LASER ULTRASONIC MONITORING OF

LASER-INDUCED THERMAL PROCESSES

by

ROSA EDITH MORALES

B.S., University of California, Davis, 2017

M.S., University of Colorado, Boulder, 2019

A thesis submitted to the

Faculty of the Graduate School of the

University of Colorado in partial fulfillment

of the requirement for the degree of

Doctor of Philosophy

Department of Mechanical Engineering

2022

Committee Members:

Todd W. Murray, Professor of Mechanical Engineering

Massimo Ruzzene, Professor of Mechanical Engineering

Rong Long, Associate Professor of Mechanical Engineering

Nick Bottenus, Assistant Professor of Mechanical Engineering

Fatemeh Pourahmadian, Assistant Professor of Civil Engineering

David M. Stobbe, Research Scientist, Lawrence Livermore National Laboratory

ABSTRACT

Morales, Rosa Edith (Ph.D., Mechanical Engineering)

Laser Ultrasonic Monitoring of Laser-Induced Thermal Processes

Thesis directed by Professor Todd W. Murray

Intra- and inter-layer integrity of components fabricated with advanced manufacturing techniques, such as laser powder bed fusion, is dependent upon rapid heating, melting, and solidification processes. There is a need for new techniques to provide *in situ* feedback of these processes. Here a laser-based ultrasonic technique to probe thermal effects induced by a high-power continuous wave laser in titanium samples is described. Numerical simulations were performed to show that, for a spatially uniform heating beam, laser-induced surface acoustic waves are strongly influenced by surface heating conditions, are dispersive in the case of rapid heating, and that an abrupt velocity reduction happens upon the onset of surface melting. Furthermore, laser-based ultrasound experimental results which monitor the transient change of surface wave travel time associated with high power laser surface heating are provided. A pulsed laser is used to generate surface acoustic waves that propagate through the laser-heated region and are detected using a photorefractive crystal-based interferometer. Qualitative agreement is observed between theory and experiment with both showing a rapid reduction in the surface wave velocity at the onset of illumination and further decrease in surface wave velocity associated with melting. It is demonstrated that changes in the surface wave velocity can be used to track local heating and detect the onset of surface melting in real time.

Additionally, we develop three-dimensional finite element acoustic models to study rapid, depth-varying laser heating. We fabricated a fast acquisition experimental setup built to probe transient depth-dependent temperature fields and melt pool depths. Agreement between theory and experiment is observed with both showing significant surface acoustic wave dispersion resulting from the rapid laser-heating. These dispersive effects are more pronounced when the heating laser power is sufficient to cause melting as the high frequency SAW components are further delayed by the presence of the melt.

The work presented here demonstrates the efficacy of using laser-based ultrasonics for *in-situ* monitoring of transient laser-induced heating and melting processes. This technique may ultimately find application in the mapping of transient laser-induced thermal fields and melt zones, providing critical information for real-time feedback and process control in advanced manufacturing systems.

DEDICATION

This dissertation is dedicated to my mother, Maria de Lourdes Morales, my father, Raul Morales, my niece, Melanie Morales, and my best friend, Yaneli Morales. To my parents, thank you for all the sacrifices you have made to ensure my siblings and I had access to a great education. To Melanie, may you always dream bigger than what the world tells you is possible. Your Tia Sisi will always be your biggest supporter. To Yaneli Morales, thank you for being my biggest cheerleader during your time on Earth. I love you forever and always.

ACKNOWLEDGEMENTS

This dissertation has been an incredible labor of love, which would not have been possible without several instrumental individuals in my life. First, I am extremely thankful for my advisor, Dr. Todd Murray, who has been an incredible teacher, mentor, and friend. I am especially thankful for all the times he inspired me, motivated me, and believed in me, even when I doubted myself. I aspire to become as dedicated a researcher as he is.

I am also grateful for all my champions, including faculty and staff, in the Mechanical Engineering department for their support throughout my PhD. I am extremely thankful for all my labmates and officemates, past and present, for enduring the long hours with me, but also for celebrating all the wins. I am especially thankful to Dr. Jordan Lum for all the kindness, unwavering support, and Costco trips he has shared with me.

I am extremely thankful for all my mentors and collaborators at Lawrence Livermore National Laboratory who helped ignite my love for research and who have supported me throughout the years to flourish as a scientist. I am especially grateful for Israel Lopez, Joe Tringe, David Stobbe, and last, but certainly not least, Beth McCormick. Beth has, and continues to be, one of my greatest cheerleaders and advocates, and I am eternally grateful for her.

Ultimately, all I have accomplished would not be possible without God and the unconditional love and support from my parents, siblings, niece, and best friends. Gracias a mis papas por los sacrificios que han echo por mi y por todo el apoyo del mundo. Los amo.

"And lastly, I want to thank me. I want to thank me for believing in me. I want to thank me for doing all this hard work. I want to thank me for having no days off. I want to thank me for never quitting... I want to thank me for just being me at all times." -Snoop Dogg

TABLE OF CONTENTS

LIST OF FIGURES

CHAPTER 1. INTRODUCTION

1.1 Advanced Manufacturing of Metals

Lasers have seen widespread use in materials processing and manufacturing applications including laser cutting, welding, ablation, drilling, surface texturing, and advanced manufacturing[1]. In these application areas, laser energy is absorbed by a material leading to local heating, melting, and vaporization, and *in-situ* control of these laser-induced processes is critical to ensure the integrity of the final product[2]. For example, in laser powder bed fusion an object is built in consecutive layers by laser melting of powder mechanically distributed over the build surface[3,4]. Intra- and inter-layer integrity is dependent upon the rapid heating, melting, and solidification processes during which defects and material discontinuities are likely to form[3-6]. If the heating laser power is too high for a given scan speed, it can lead to evaporation of the material from a molten pool, a subsequent recoil force, and collapse of the melt pool, resulting in porosity in the component. Alternatively, a low laser heating power can lead to an incomplete melting and solidification process and lack of fusion defects[7,8]. The optimal laser parameters, defined as those required to produce a part with the lowest number of processing defects, are difficult to determine *a priori* due to the complexity of the process and additional variables including powder quality and machine to machine variations in laser characteristics[9].

1.2 Nondestructive Evaluation Techniques for Advanced Manufacturing Processes

The success of laser-based manufacturing techniques, such as powder bed fusion, hinges on the ability of the operator to set and control process variables such as laser power and speed[10,11]. Nondestructive evaluation can aid in this process and provide *in situ* feedback on the build quality such that process variables can be adjusted in real time[12]. Several nondestructive evaluation

methods such as thermal imaging, optical imaging, and conventional ultrasonics have been employed to monitor laser powder bed fusion builds *in situ*[9,12]. These techniques offer remote access to the high temperature laser-material interaction site. Thermal imaging can provide information regarding the surface temperature distribution, and optical imaging can be used to ascertain surface morphology changes[9]. Conventional acoustic emission and ultrasound can potentially provide additional data regarding the build process[13]. In the case of acoustic emission, the sound generated during the laser heating process is detected using a microphone or transducer and analyzed to infer information about the process[14]. Using advanced signal processing techniques, such as machine learning, it is possible to categorize the laser-material interaction into different regimes[15].

Defect characterization in components built by advanced manufacturing techniques remains very important as complete defect mitigation has not yet been achieved[16]. X-ray computed tomography is a common nondestructive technique that has been used for defect quantification post-built as a stand-alone method[17-19] and as complimentary measurements to *in situ* process monitoring methods that detect the defects as they form[20-22].

1.3 Conventional Ultrasonic Techniques as an Evaluation Technique for Advanced Manufacturing Processes

The physical, mechanical, optical, and thermal properties of materials are functions of temperature. It follows that the velocity of ultrasonic waves is also temperature dependent with an increase in temperature generally leading to a softening of the material and lower longitudinal, shear, and surface acoustic wave velocities. Ultrasound thermography is a well-known technique used to determine the temperature of a uniformly heated sample or to map out temperature distributions below the surface[23]. Ultrasound thermography has attracted strong attention in the

medical ultrasonics community to continuously monitor and provide feedback to thermal treatment processes in biological tissue such as high intensity focused ultrasound therapy[23,24]. Some of the advantages of conventional ultrasonic techniques for process monitoring is that they are not limited to surface temperature determination, and that the transducers can be placed remote from the process zone. For additive manufacturing, they do require physical access to the build surface, but the contact location can be somewhat removed from the high temperature environment. The dependence of bulk wave propagation on temperature, mechanical properties, and phase state of the material has, for example, been used to infer the temperature in the processing zone and to predict the melt pool size based on monitoring bulk waves reflected and scattered from the melt pool[25,26].

1.4 Laser-Based Ultrasound as an Evaluation Technique for Advanced Manufacturing Processes

Laser-based ultrasonic techniques are well suited for the real-time monitoring and nondestructive evaluation of laser-induced thermal processes. The laser detection probe beam and laser source exciting the ultrasonic waves can be remote from the high temperature manufacturing process environment through using optically transparent windows or other means. Ultrasound generation by laser irradiation provides a number of advantages over conventional ultrasound in its higher spatial resolution, its narrow-band and broadband generation, its ability to provide absolute measurements, and its ability to be completely noncontact and operate on curved, rough, and hard to access surfaces[27].

Laser ultrasonic techniques have been used to evaluate advanced manufacturing builds by using surface acoustic waves and bulk waves to detect surface and near subsurface defects *ex situ*[16,28-35]. Surface acoustic waves and bulk waves have also been used to evaluate material

microstructure and grain size[36], to infer the surface temperature in laser induced thermal processes[31,37], to predict internal temperature distributions based on waves propagating over multiple paths[38], and to observe melting and solidification during crystal growth[39]. This technique has also been used for high temperature measurements of materials properties[40] and for phase transformation studies in metals[41-43].

1.5 Laser Acoustic Generation in Metals

In laser-based ultrasound, irradiation of the surface of a solid by pulsed laser light generates wave motions in the material. These acoustic signals have frequencies ranging from kHz to GHz that provide fine spatial resolutions leading to their wide use for detection of defects in metal structures[44,45]. Ultrasound can be generated in different regimes, depending on the energy density deposited by the laser pulse, which determine the dominant wave modes created. The main regimes are the thermoelastic regime and the ablative, or plasma, regime[46,47]. The ablative regime is not nondestructive as it is induced with high power densities which result in a small ablation pit a few microns deep. Here, a thin surface layer of the material melts, followed by an ablation process where particles fly off the surface and induce the forces that generate ultrasonic waves[27]. The focus of this work is the nondestructive thermoelastic regime where ultrasonic waves are generated from a pulsed laser focused onto a material causing it to heat up and expand, thus creating mechanical vibrations and transient stress fields that radiate energy as coherent elastic waves that can be sensed by a continuous beam[46]. Figure 1-1 illustrates a simplified schematic of a laser ultrasonic inspection where the generation and detection lasers are placed at a certain source to detector distance from each other.
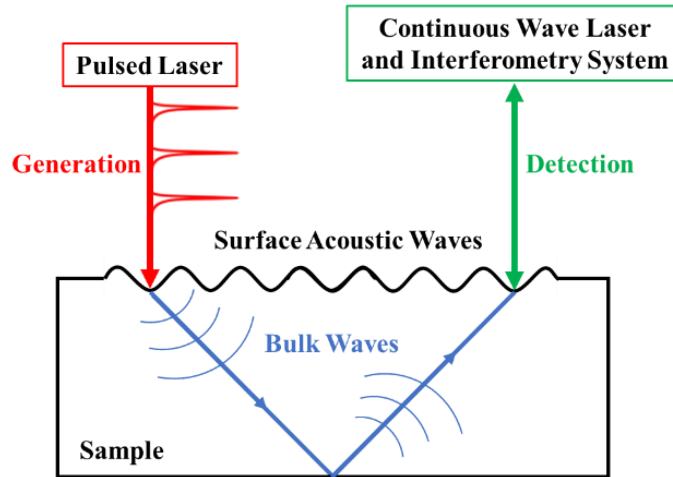
Figure 1-1. Schematic of a laser ultrasonic technique.

Depending on the application, the generation laser beam and continuous wave detection beam can be focused onto a sample in different configurations: at a distance from one another, as depicted in Figure 1-1, directly on top of each other, or directly opposite one another on different sides of a sample. In the latter two configurations, the detection is at the epicenter of the generation source and only bulk waves are detected. In this work the configuration used is the one depicted in Figure 1-1. The generation laser pulses are absorbed at the surface of an elastic sample where they cause rapid heating, thermal expansion, and elastic longitudinal, shear, and surface waves to be generated simultaneously through the thermoelastic effect, which are detected on the same side of the sample at a certain distance from the generation. Longitudinal waves propagate parallel to the direction of particle motion, while shear waves propagate perpendicular to the particle motion[46]. Longitudinal and shear waves, also known as bulk waves, travel the same path, as depicted in Figure 1-1, but they propagate at different speeds of c_L and c_T, respectively. Additionally, the free surface boundary can support surface skimming longitudinal waves which propagate along the surface between the source and detector at the longitudinal wave speed, c_L.

Most importantly, this free surface boundary also supports Rayleigh waves, also known as surface acoustic waves, which also propagate along the surface as shown in Figure 1-1.

Rayleigh waves propagate parallel to the surface at the Rayleigh wave velocity, c_R. Rayleigh waves only propagate in two dimensions across the surface thus resulting in less geometric attenuation with distance than that of bulk waves, which propagate throughout three-dimensional space. This results in Rayleigh waves having larger amplitudes when compared to longitudinal, shear, and surface-skimming waves[46]. Each of these acoustic modes have characteristic directivity patterns which can be utilized for particular applications to gain information on defects, phases, and microstructure information, for example[47,48]. The velocity, dispersion characteristics, scattering, and attenuation of ultrasonic waves can also be evaluated to determine various physical and material properties[46].

1.6 Surface Acoustic Wave Inspection

Rayleigh waves, or surface acoustic waves (SAWs), are confined to propagate in the near-surface region and as such, are very sensitive to defects and properties in this region[16,29-35]. The velocity of ultrasonic waves is highly sensitive to temperature due to an increase in temperature leading to a softening of the material and lower surface acoustic wave velocities. As such, surface acoustic waves and their times of arrival have been used to infer the surface temperature in laser-induced thermal processes[31,32,37].

Surface acoustic waves are known to be dispersive on a coating-substrate system due to the mechanical properties of the system varying with depth, unlike nondispersive SAWs that propagate in a half-space[49]. In other words, surface acoustic waves are dispersive when the mechanical properties of a material are spatially dependent over the wavelength of the surface

acoustic wave, where the wavelength $\lambda = c/f$. Here, c is the wave velocity and f is the frequency. This dispersive effect means that the phase and group velocities are not constant and are a function of frequency. Figure 1-2 depicts how the surface acoustic wave penetration is frequency dependent. In this figure, we use a laser-heated material to demonstrate dispersion effects because it is known that material properties are temperature-dependent. In this scenario, the material is heated at the surface so the resulting properties will be of a high-temperature material near the surface with the substrate converging to room temperature.
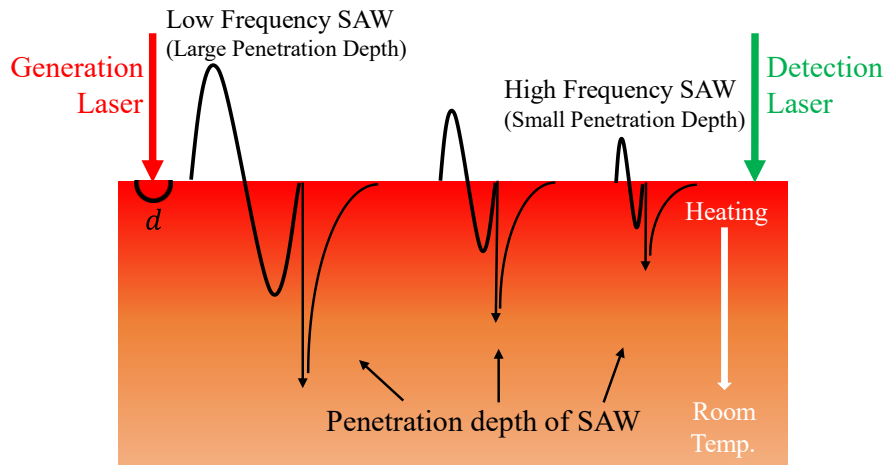
Figure 1-2. Surface acoustic waves propagating on a laser-heated material.

As seen in Figure 1-2, the low frequency SAWs have a large penetration depth further into the material, and the velocity at which these waves travel is determined by the elastic properties of the cooler substrate. On the other hand, the high frequency SAWs are confined to the near-surface region, so the SAW velocity is determined by the elastic properties of the coating, or in this case, the high-temperature area. This frequency dependence on the penetration of the SAWs makes the measurement and analysis of SAW dispersion well suited for investigating depth-dependent material properties[50-57]. To determine depth-dependent material properties with laser-based ultrasound, the theory for SAW propagation in isotropic multi-layer films on a semi-infinite

substrate needs to be well understood to be able to compare measured dispersion curves to a theoretical model[51,58]. This theory is utilized in this report to study surface acoustic wave propagation through a laser-heated region modeled as a multilayered structure.

1.7 Overview of this Thesis

In this work, we use laser-based ultrasound to monitor laser-induced heating and melting processes. In Chapter 2, we discuss a theoretical model for calculating one-dimensional temperature fields as a function of depth and time after heating begins induced by spatially uniform continuous wave laser heating. We show that slow laser heating leads to a temperature rise that is fairly uniform over the near-surface region, while rapid laser heating results in marked thermal gradients in this near-surface region. In Chapter 3, we discuss the theory behind a laser ultrasonic model that calculates elastic displacement induced by pulsed laser excitation and interferometric detection in a multi-layered plate on a semi-infinite solid In Chapter 4, we present numerical simulations from the coupled theory in Chapters 2 and 3 where we model the pulsed laser excitation and interferometric detection of the CW laser-heated surface at a given time after laser-heating is begun. We show that for a spatially uniform heating beam, laser-induced surface acoustic waves are strongly influenced by surface heating conditions, are dispersive in the case of rapid heating where the thermally-induced mechanical property change is on the same spatial scale as the wavelength of the surface acoustic waves, and we show an abrupt velocity reduction upon the onset of surface melting.

In Chapter 5, we present the experimental setup built to study surface acoustic wave propagation through laser-heated regions of Ti-6Al-4V samples. We use a pulsed laser line source to generate surface acoustic waves and a photorefractive crystal-based interferometer to monitor the transient change of surface wave travel time associated with slow, high-power laser surface

heating and melting from a Gaussian heating beam placed between the source and receiver positions. In agreement with the numerical simulations, a deviation in the response is observed when the heating laser power is sufficient to cause local surface melting. It is demonstrated that changes in the surface wave velocity can be used to track local heating and detect the onset of surface melting in real time.

In Chapter 6, we develop three-dimensional finite element acoustic models with which to study rapid, depth-varying laser heating. We also present a fast acquisition experimental setup built to probe transient depth-dependent temperature fields and at sufficiently high powers, melt pool depths. We use a pulsed laser line source to generate high frequency surface acoustic waves and a Michelson interferometer to monitor the surface wave dispersion associated with rapid, depth-varying laser heating and melting from a Gaussian heating beam placed between the source and receiver positions. Agreement between theory and experiment is observed with both showing significant surface acoustic wave dispersion resulting from the rapid laser-heating since the induced thermal gradients cause the higher frequency components of the SAW that probe the near-surface temperatures to be delayed with respect to the lower frequencies that penetrate further into the cooler bulk of the material. These dispersive effects are more pronounced when the heating laser power is sufficient to cause local melting as the high frequency SAW components are further delayed by the presence of the melt. It is demonstrated that surface wave dispersion can be used to track transient depth-varying heating and melting. In Chapter 7, we conclude by summarizing our findings thus far and discuss ideas for future studies that can further supplement this research.

REFERENCES

1. Von Allmen, M. & Blatter, A. *Laser-beam interactions with materials: physical principles and applications*. (Springer, 1995).

2. Ready, J. F. *Effects of high-power laser radiation*. (Academic Press, 1971).

3. Ye, J. *et al.* Energy Coupling Mechanisms and Scaling Behavior Associated with Laser Powder Bed Fusion Additive Manufacturing. *Adv. Eng. Mater.* **21**, 1900185 (2019).

4. Khairallah, S. A. *et al.* Controlling interdependent meso-nanosecond dynamics and defect generation in metal 3D printing. *Science* **368**, 660–665 (2020).

5. Mercelis, P. & Kruth, J. Residual stresses in selective laser sintering and selective laser melting. *Rapid Prototyping Journal* **12**, 254–265 (2006).

6. Thijs, L., Verhaeghe, F., Craeghs, T., Humbeeck, J. V. & Kruth, J.-P. A study of the microstructural evolution during selective laser melting of Ti–6Al–4V. *Acta Materialia* **58**, 3303–3312 (2010).

7. Matthews, M. J. *et al.* Denudation of metal powder layers in laser powder bed fusion processes. *Acta Materialia* **114**, 33–42 (2016).

8. Khairallah, S. A., Anderson, A. T., Rubenchik, A. & King, W. E. Laser powder-bed fusion additive manufacturing: Physics of complex melt flow and formation mechanisms of pores, spatter, and denudation zones. *Acta Materialia* **108**, 36–45 (2016).

9. Grasso, M. & Colosimo, B. M. Process defects and *in situ* monitoring methods in metal powder bed fusion: a review. *Meas. Sci. Technol.* **28**, 044005 (2017).

10. Kiss, A. M. *et al.* Laser-Induced Keyhole Defect Dynamics during Metal Additive Manufacturing. *Adv. Eng. Mater.* **21**, 1900455 (2019).

11. King, W. E. *et al.* Laser powder bed fusion additive manufacturing of metals; physics, computational, and materials challenges. *Applied Physics Reviews* **2**, 041304 (2015).

12. Everton, S. K., Hirsch, M., Stravroulakis, P., Leach, R. K. & Clare, A. T. Review of in-situ process monitoring and in-situ metrology for metal additive manufacturing. *Materials & Design* **95**, 431–445 (2016).

13. Rieder, H., Dillhöfer, A., Spies, M., Bamberg, J. & Hess, T. Ultrasonic online monitoring of additive manufacturing processes based on selective laser melting. in 184–191 (2015).

14. Kouprianoff, D., Yadroitsava, I., du Plessis, A., Luwes, N. & Yadroitsev, I. Monitoring of Laser Powder Bed Fusion by Acoustic Emission: Investigation of Single Tracks and Layers. *Front. Mech. Eng.* **7**, 678076 (2021).

15. Shevchik, S. A., Masinelli, G., Kenel, C., Leinenbach, C. & Wasmer, K. Deep Learning for *In Situ* and Real-Time Quality Monitoring in Additive Manufacturing Using Acoustic Emission. *IEEE Trans. Ind. Inf.* **15**, 5194–5203 (2019).

16. Harke, K. J., Calta, N., Tringe, J. & Stobbe, D. Laser-based ultrasound interrogation of surface and sub-surface features in advanced manufacturing materials. *Sci Rep* **12**, 3309 (2022).

17. du Plessis, A. & le Roux, S. G. Standardized X-ray tomography testing of additively manufactured parts: A round robin test. *Additive Manufacturing* **24**, 125–136 (2018).

18. Wildenschild, D. & Sheppard, A. P. X-ray imaging and analysis techniques for quantifying pore-scale structure and processes in subsurface porous medium systems. *Advances in Water Resources* **51**, 217–246 (2013).

19. Obbard, R. W. *et al*. Micro computed tomography for in situ analysis of subsurface structure. in *2021 IEEE Aerospace Conference (50100)* 1–10 (IEEE, 2021). doi:10.1109/AERO50100.2021.9438421.

20. Snow, Z., Diehl, B., Reutzel, E. W. & Nassar, A. Toward in-situ flaw detection in laser powder bed fusion additive manufacturing through layerwise imagery and machine learning. *Journal of Manufacturing Systems* **59**, 12–26 (2021).

21. Forien, J.-B. et al. Detecting keyhole pore defects and monitoring process signatures during laser powder bed fusion: A correlation between in situ pyrometry and ex situ X-ray radiography. *Additive Manufacturing* **35**, 101336 (2020).

22. Mitchell, J. A., Ivanoff, T. A., Dagel, D., Madison, J. D. & Jared, B. Linking pyrometry to porosity in additively manufactured metals. *Additive Manufacturing* **31**, 100946 (2020).

23. Dalong Liu & Ebbini, E. S. Real-Time 2-D Temperature Imaging Using Ultrasound. *IEEE Trans. Biomed. Eng.* **57**, 12–16 (2010).

24. Lai, P. *et al.* Real-Time Monitoring of High-Intensity Focused Ultrasound Lesion Formation Using Acousto-Optic Sensing. *Ultrasound in Medicine & Biology* **37**, 239–252 (2011).

25. Gillespie, J. *et al. In situ* characterization of laser-generated melt pools using synchronized ultrasound and high-speed X-ray imaging. *The Journal of the Acoustical Society of America* **150**, 2409–2420 (2021).

26. Yang, T. *et al.* In-situ monitoring and ex-situ elasticity mapping of laser induced metal melting pool using ultrasound: Numerical and experimental approaches. *Journal of Manufacturing Processes* **71**, 178–186 (2021).

27. Achenbach, J. D. The Thermoelasticity of Laser-Based Ultrasonics. *Journal of Thermal Stresses* **28**, 713–727 (2005).

28. Davis, G. *et al.* Laser ultrasonic inspection of additive manufactured components. *Int J Adv Manuf Technol* **102**, 2571–2579 (2019).

29. Dai, T. *et al*. Laser ultrasonic testing for near-surface defects inspection of 316L stainless steel fabricated by laser powder bed fusion. *China Foundry* **18**, 360–368 (2021).

30. Everton, S., Dickens, P., Tuck, C. & Dutton, B. Using Laser Ultrasound to Detect Subsurface Defects in Metal Laser Powder Bed Fusion Components. *JOM* **70**, 378–383 (2018).

31. Manzo, A. J. & Helvajian, H. Utility of optical heterodyne displacement sensing and laser ultrasonics as in situ process control diagnostic for additive manufacturing. *Opt. Eng.* **57**, 1 (2018).

32. Manzo, A. J. & Helvajian, H. Pulsed laser ultrasonic excitation and heterodyne detection for *in situ* process control in laser 3D manufacturing. *Journal of Laser Applications* **29**, 012012 (2017).

33. Jian, X., Dixon, S., Guo, N. & Edwards, R. Rayleigh wave interaction with surface-breaking cracks. *Journal of Applied Physics* **101**, 064906 (2007).

34. Klein, M. & Sears, J. Laser ultrasonic inspection of laser cladded 316LSS and TI-6-4. in *International Congress on Applications of Lasers & Electro-Optics* 1006 (Laser Institute of America, 2004).

35. Steg, R. G. & Klemens, P. G. Scattering of Rayleigh Waves by Surface Irregularities. *Phys. Rev. Lett.* **24**, 381–383 (1970).

36. Smith, R. J. *et al.* Spatially resolved acoustic spectroscopy for selective laser melting. *Journal of Materials Processing Technology* **236**, 93–102 (2016).

37. Yamada, H., Kosugi, A. & Ihara, I. Noncontact Monitoring of Surface Temperature Distribution by Laser Ultrasound Scanning. *Jpn. J. Appl. Phys.* **50**, 07HC06 (2011).

38. Shi, Y.-A. *et al.* A Method for Reconstructing Internal Temperature Distribution in Solid Structure. *J Nondestruct Eval* **39**, 48 (2020).

39. Queheillalt, D. T. & Wadley, H. N. G. Laser ultrasonic sensing of the melting and solidification of cadmium telluride. *Journal of Crystal Growth* **225**, 34–44 (2001).

40. Kil-Mo Koo, Dong-Gyu Jeong, Jong-Ho Choi, & Duck-Young Ko. A new measurement system of very high temperature in atomic pile using ultrasonic delay time. in *Proceedings of IEEE Region 10 International Conference on Electrical and Electronic Technology. TENCON 2001 (Cat. No.01CH37239)* vol. 2 860–863 (IEEE, 2001).

41. Hinterlechner, I. *et al.* In-situ monitoring of phase transformation in Ti-6Al-6V-2Sn using laser ultrasonics. *Nondestructive Testing and Evaluation* **33**, 130–138 (2018).

42. Kruger, S. E. & Damm, E. B. Monitoring austenite decomposition by ultrasonic velocity. *Materials Science and Engineering: A* **425**, 238–243 (2006).

43. Shinbine, A., Garcin, T. & Sinclair, C. In-situ laser ultrasonic measurement of the hcp to bcc transformation in commercially pure titanium. *Materials Characterization* **117**, 57–64 (2016).

44. Tanaka, T. & Izawa, Y. Nondestructive Detection of Small Internal Defects in Carbon Steel by Laser Ultrasonics. *Jpn. J. Appl. Phys.* **40**, 1477–1481 (2001).

45. Moreau, A. et al. On-line measurement of texture, thickness and plastic strain ratio using laser-ultrasound resonance spectroscopy. *Ultrasonics* **40**, 1047–1056 (2002).

46. Scruby, C. B. & Drain, L. E. *Laser Ultrasonics: Techniques and Applications*. (Routledge, 2019). doi:10.1201/9780203749098.

47. Davies, S. J., Edwards, C., Taylor, G. S. & Palmer, S. B. Laser-generated ultrasound: its properties, mechanisms and multifarious applications. *J. Phys. D: Appl. Phys*. **26**, 329–348 (1993).

48. M. C. Brennan, *Investigation of Laser Ultrasonic Evaluation for Use as an In Situ Process Monitoring Tool for Laser-Based Directed Energy Deposition*. The Pennsylvania State University (2018)

49. Murray, T. W., Krishnaswamy, S. & Achenbach, J. D. Laser generation of ultrasound in films and coatings. *Appl. Phys. Lett.* **74**, 3561–3563 (1999).

50. T. L. Steen, *Inspection of functionally graded coating materials using frequency domain photoacoustic microscopy*. Boston University (2008).

51. Guo, Z., Achenbach, J. D., Madan, A., Martin, K. & Graham, M. E. Integration of modeling and acoustic microscopy measurements for thin films. *The Journal of the Acoustical Society of America* **107**, 2462–2471 (2000).

52. Murray, T. W., Balogun, O., Steen, T. L., Basu, S. N. & Sarin, V. K. Inspection of compositionally graded mullite coatings using laser based ultrasonics. *International Journal of Refractory Metals and Hard Materials* **23**, 322–329 (2005).

53. Bucaro, J. A. & Flax, L. Application of acoustic surface waves to the study of surface properties of ion-exchanged glass. *Journal of Applied Physics* **45**, 765–774 (1974).

54. Szabo, T. L. Obtaining subsurface profiles from surface−acoustic−wave velocity dispersion. *Journal of Applied Physics* **46**, 1448–1454 (1975).

55. Glorieux, C. et al. Surface acoustic wave depth profiling of elastically inhomogeneous materials. *Journal of Applied Physics* **88**, 4394 (2000).

56. Zhang, F., Krishnaswamy, S., Fei, D., Rebinsky, D. A. & Feng, B. Ultrasonic characterization of mechanical properties of Cr- and W-doped diamond-like carbon hard coatings. *Thin Solid Films* **503**, 250–258 (2006).

57. Goossens, J. et al. Surface acoustic wave depth profiling of a functionally graded material. *Journal of Applied Physics* **102**, 053508 (2007).

58. Cheng, J., Wu, L. & Zhang, S. Thermoelastic response of pulsed photothermal deformation of thin plates. *Journal of Applied Physics* **76**, 716–722 (1994).

CHAPTER 2. LASER-INDUCED HEATING THEORETICAL MODEL

In this chapter, we discuss a theoretical model for calculating one-dimensional temperature fields induced by spatially uniform continuous wave laser heating. The work presented in Chapter 2, Chapter 3, Chapter 4, and Chapter 5 was condensed into a journal article titled "Real-time laser ultrasonic monitoring of laser-induced thermal processes" and was published in *Scientific Reports*[1].

2.1 Finite Difference Laser Heating Model

In this work, we calculate the elastic displacement response generated by a nanosecond pulsed laser incident upon a surface that is being heated by a spatially uniform continuous wave (CW) laser with a step-function time dependence. First, the one-dimensional temperature field produced by a CW laser is calculated using the implicit finite difference method presented by Singh and Narayan[2]. Finite difference techniques involve splitting time and space into finite temporal and spatial steps and approximating the differential equation with a difference equation at each of these points[3,4]. The difference equations are derived from a Taylor series expansion of the derivatives about spatial and temporal points of observation. Truncation error in finite difference techniques is inherent and is due to the use of difference equations to replace the differential equations[5]. Here, an implicit technique is used which consists of a system of i equations being solved simultaneously at every time step, where i refers to the number of space steps. Unlike explicit techniques, where a single unknown is solved at every time step, implicit techniques do not suffer from stability criterion limitations, allowing more freedom when choosing space and time steps. The finite difference method utilized in this work was presented by Richtmyer[4] and used for laser heating problems by Singh and Narayan[2]. It is a higher order implicit method with a small truncation error of $O(\Delta t)^2 + O(\Delta x)^4$ which is not restricted by any stability criterion, thus

14

leading to rapid convergence to the exact solution. This implicit finite difference method was used by Murray[5,6] to model laser generation of acoustic waves in the ablative regime. They solve the one-dimensional laser vaporization problem to calculate pressure exerted on the surface during Q-switched laser heating.

Unlike in the work referenced here where pulsed laser irradiation is considered[2,5,6], we adapt our methods for irradiation from a continuous wave laser source with a step-function time dependence. The model is used to determine the temperature as a function of time (t) at each depth (d) below the surface, and it tracks the melt front position. Temperature-dependent thermal properties and density of the irradiated material are utilized in this formulation. Finite difference equations are set up for accurate determination of the temperature gradients at the liquid-solid interface, which controls the resulting melt depth. The thermal profiles and melt front positions are tracked explicitly in this finite difference routine with increasing laser irradiation time, or time of heating. The solution approach closely follows that of Singh and Narayan[2] and is summarized in this section.

The one-dimensional temperature $T(z,t)$ in a material during laser irradiation is controlled by the heat flow equation given by

$$\rho_i(T)C_{p_i}(T)\frac{\partial T_i(z,t)}{\partial t} = \frac{\partial}{\partial z}\left(K_i(T)\frac{\partial T_i(z,t)}{\partial z}\right) + I_0(1-R)\exp(-\alpha z) \quad [1]$$

where z refers to direction perpendicular to the plane of the sample and t is time. The subscript i is set to $i=1,2$ in reference to the solid or liquid phase, respectively. The terms $\rho(T)$, $C_p(T)$, and $K(T)$ refer to the temperature-dependent density, thermal heat capacity per unit mass, and thermal conductivity, respectively. R and α are the reflectivity and absorption coefficients of the material corresponding to the laser wavelength. The temperature-dependence of these variables is neglected

in our work. I_0 is the laser intensity of the CW laser source heating the surface. In the formulation of this problem, radial heat flow from the illuminated region is neglected, and it is assumed that there are no thermal losses in the front and back surfaces.

The boundary condition at the solid-liquid interface assumes the liquid and solid temperatures present at the interface are equal: $T_1 = T_2 = T(z)$, where this interface temperature $T(z)$ is equal to the melting point, T_m, during melting. The position of the solid-liquid interface is determined by the heat balance at the interface, and is expressed as

$$-K_1 \frac{\partial T_1}{\partial z}\bigg|_{z=S} + K_2 \frac{\partial T_2}{\partial z}\bigg|_{z=S} = L \frac{dS}{dt} \qquad [2]$$

where S refers to the interface position and L is the latent heat per unit volume of the material. To solve the heat flow equation with the boundary conditions listed above, the finite difference scheme is needed. To do so, the heat flow equation and melt front position are made non-dimensional by introducing the following quantities

$$\bar{z} = \frac{z}{l}, \qquad \bar{S} = \frac{S}{l}, \qquad \theta = \frac{T - T_m}{T_m}, \qquad \bar{t} = \frac{T_m K_s t}{L l^2} \quad [3]$$

where K_s and l are constants set to equal the thermal conductivity of the material at room temperature and the desired spatial step size of the model in cm, respectively. These constants are substituted into Equation 1 to obtain the non-dimensional form of the heat flow equation expressed as

$$\frac{\partial \theta}{\partial \bar{t}} = \sigma(T) \left(\frac{\partial^2 \theta}{\partial \bar{z}^2} + \frac{1}{K(T)} \frac{\partial K(T)}{\partial \bar{z}} \frac{\partial \theta}{\partial \bar{z}} \right) + \frac{I_0 (1 - R) \exp(-\alpha z) L l^2}{T_m^2 K_s C_v(T)} \quad [4]$$

where $C_v(T)$ is the volume heat capacity given by $C_v(T) = \rho C_p(T)$, and $\sigma(T)$ is the effective thermal diffusivity of the material given by $\sigma(T) = K(T)L/(K_S C_v(T)T_m)$. The solid-liquid interface boundary condition can also be expressed in its non-dimensional form as

$$\frac{\partial \bar{S}}{\partial t} = \frac{K_1 \partial \theta_2}{K_S \partial \bar{z}}\bigg|_{\bar{z}=\bar{S}} - \frac{K_2 \partial \theta_1}{K_S \partial \bar{z}}\bigg|_{\bar{z}=\bar{S}} \qquad [5]$$

To solve the differential equation with this implicit finite difference formulation, the time and space area are divided into small steps Δt and Δz as follows:

$$\bar{t} = n\Delta t \qquad n = 0,1,2,3, \dots, M$$
$$\bar{z} = i\Delta z \qquad i = 0,1,2,3, \dots, N \qquad [6]$$

where M and N are the total number of steps in time and space, respectively. The position of the melt front interface is followed explicitly and is given by

$$\bar{S} = q\Delta z + \varepsilon \Delta z \qquad -0.5 < \varepsilon < 0.5 \qquad [7]$$

where q is a whole number representing a grid point and ε is the fractional distance of the solid-liquid interface from the grid point q. The finite difference expressions that follow and the derivation of this particular technique are outlined in detail in the literature[2,4].

With this model, we calculate the temperature at any point in the plate, within the 1-D approximation, and track the position of the melt front. In this study, we use the Titanium alloy Ti-6Al-4V for all our theoretical and experimental work. Temperature-dependent thermal properties and density for both the solid and liquid Ti-6Al-4V phases[7-10] are included in the finite difference program. These properties and others needed for the model are summarized in Table I.

Table I. Thermal and optical properties of Ti-6Al-4V used in the laser heating model.

Absorption depth, α	100 nm
Reflectivity at λ=1064 nm, R	0.6154
Melting temperature, T_m	1943 K
Vaporization temperature, T_v	3560 K
Density, ρ	4.42 g/cm^3
Atomic weight	47.897 g/mol
Latent heat of melting, L	390 kJ/mol
Latent heat of vaporization, L_v	421 kJ/mol
Thermal conductivity at room temperature, K_S	7 W/m K
Thermal conductivity $(T<T_m)$, K_1	$-0.797 + 18.2$E-3$T - 20$E-6T^2 W/m K
Thermal conductivity $(T>T_m)$, K_2	34.6 W/m K
Heat capacity $(T<T_m)$, C_{p_1}	$0.4115 + 2$E-4$T + 5$E-10T^2 J/g K
Heat capacity $(T>T_m)$, C_{p_2}	0.83 J/g K

2.2 Test of the Model

The analytical solution for one-dimensional heating induced by a Gaussian beam absorbed at the surface of a semi-infinite solid[11] is used to verify the finite difference routine

$$T(z,t) = \frac{2F_0}{K}\sqrt{\kappa t}\ \text{ierfc}\left(\frac{z}{2\sqrt{\kappa t}}\right) \qquad [8]$$

where F_0 is the constant power density, K is thermal conductivity, κ is thermal diffusivity, z is depth, and t is time. This equation calculates the temperature rise from room temperature, T, as a function of depth and time with constant room temperature values. As such, the finite difference routine was executed without temperature-dependent properties to verify that the room temperature calculations matched the analytical solution. The following constant room temperature values for Ti-6Al-4V were used in the finite difference routine and in the analytical solution above to calculate surface temperature (at $z = 0$): $K = 7$ W/mK, $\kappa = K/(\rho\ c_p)$ where $\rho = 4.42$ g/cm^3 and $c_p = 0.565$ J/gK. Absorption depth and reflectivity values listed in Table I were

used and an incident laser power density of $F_0 = 2$ kW/cm^2 was chosen. The resulting analytical

solution from Equation 8 and the finite difference solution are plotted in Figure 2-1. The finite

difference solution converges to the exact solution indicating that the algorithm works.
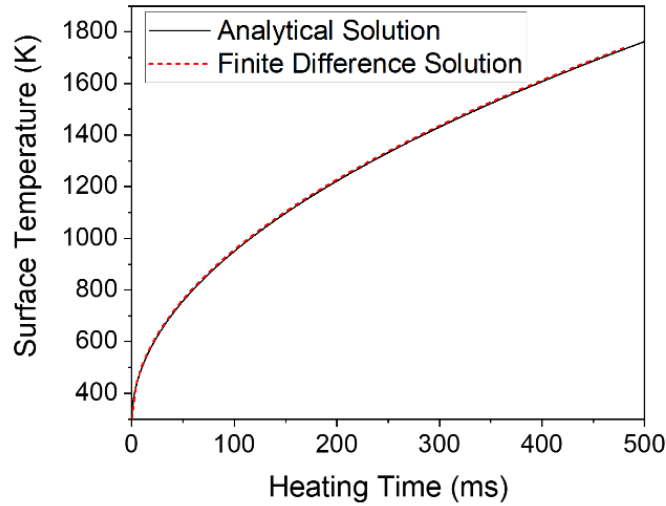
Figure 2-1. Comparison between analytical and finite difference solution of surface temperature
for laser heating at a constant heating power density of 2 kW/cm^2 in Ti-6Al-4V.

After verifying the convergence of the finite difference solution, temperature-dependent

properties were again implemented, and heating studies were conducted at a low laser power

density of 6 kW/cm^2 and a much higher power density of 250 kW/cm^2.

2.3 Slow Heating Study

We first study a slow heating case in which we use a constant heating laser power density

of 6 kW/cm^2 to heat a 3.6 mm thick model for 550 ms. The non-dimensional step sizes used in

these calculations are $\Delta t = 0.075$ and $\Delta z = 0.075$, with $n = 878,000$ and $i = 16,000$ total steps in

time and space, respectively, and a length constant $l = $ 8e-4 cm resulting in the 550 ms and the 3.6

mm thickness. Figure 2-2(a) shows the surface temperature (at $d = 0$) as a function of time where

the heating laser is turned on at $t = 0$ and a heating laser power of 6 kW/cm^2. The surface temperature rises until it reaches the melting temperature of 1943 K at a time of about 465 ms, where it briefly remains until the net heat absorbed exceeds the latent heat of phase change[2,12]. The melt front then begins to propagate into the material and, as shown on the right axis of Figure 2-2(a), proceeds rapidly to a depth of over 35 μm. Figure 2-2(b) shows the full extent of the calculated thermal data, with the color bar indicating the temperature rise at each depth and heating time.
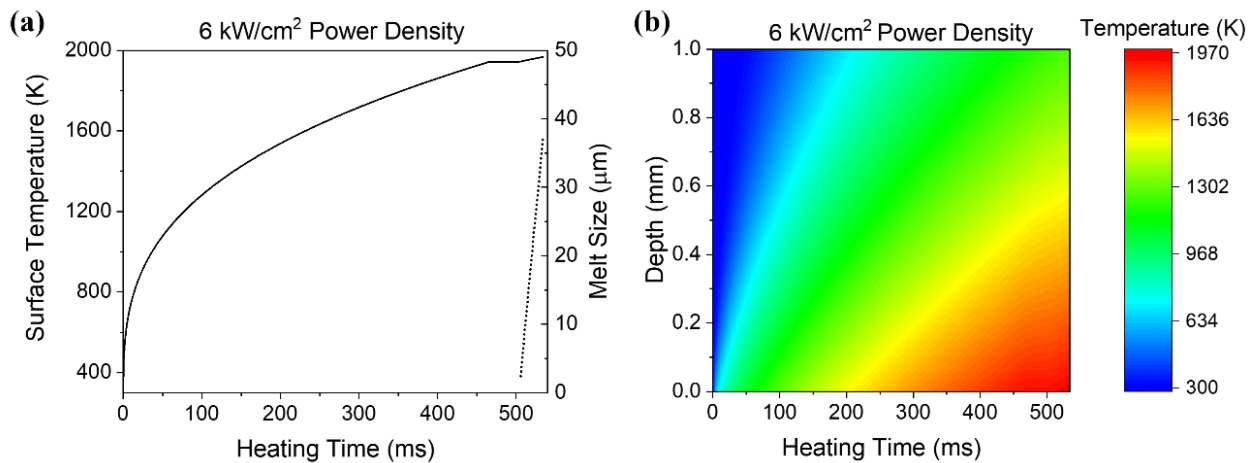
Figure 2-2. *(a)* Surface temperature (solid line) and melt size (dotted line) as a function of heating time for a 6 kW/cm^2 laser power density incident on Ti-6Al-4V. *(b)* Calculated temperature field as a function of heating time and depth for the 6 kW/cm^2 power density.

Surface acoustic waves are confined to propagate in the near surface region with a penetration depth on the order of the wavelength. For example, for a frequency of 30 MHz, surface waves in Ti-6Al-4V will be sensitive to mechanical property changes that occur over a depth of approximately 100 μm. In Figure 2-2(b), the temperature rise is somewhat uniform over the near surface region, and thus it is expected that the mechanical property changes will also be relatively constant over the penetration depth, resulting in a surface acoustic wave delay that is frequency independent.

2.4 Rapid Heating Study

Next, we use a much higher power of 250 kW/cm^2 to heat a 240 µm thick model for only 500 µs. The non-dimensional step sizes used in these calculations are $\Delta t = 0.075$ and $\Delta z = 0.075$ with $n = 80,000$ and $i = 4,000$ total steps in time and space, respectively, and a length constant $l = 8e\text{-}5$ cm. Here, we need a smaller length constant to have enough time and space steps to allow the solution to converge. Figure 2-3(a) shows the surface temperature for the 250 kW/cm^2 power density. Here, surface melting occurs at about 300 µs and there are marked thermal gradients in the near surface region within the 500 µs time window as shown in Figure 2-3(b). These thermal gradients can cause dispersion of surface waves since the higher frequency waves, with a shorter wavelength, will be more influenced by the near surface region while lower frequency waves will penetrate further into the cooler substrate. This one-dimensional thermal model allows for the calculation of temperature as a function of depth and melt front position at any time after the heating laser is turned on, and it is used to determine the elastic displacement response generated by a pulsed laser source incident upon a laser-heated surface.
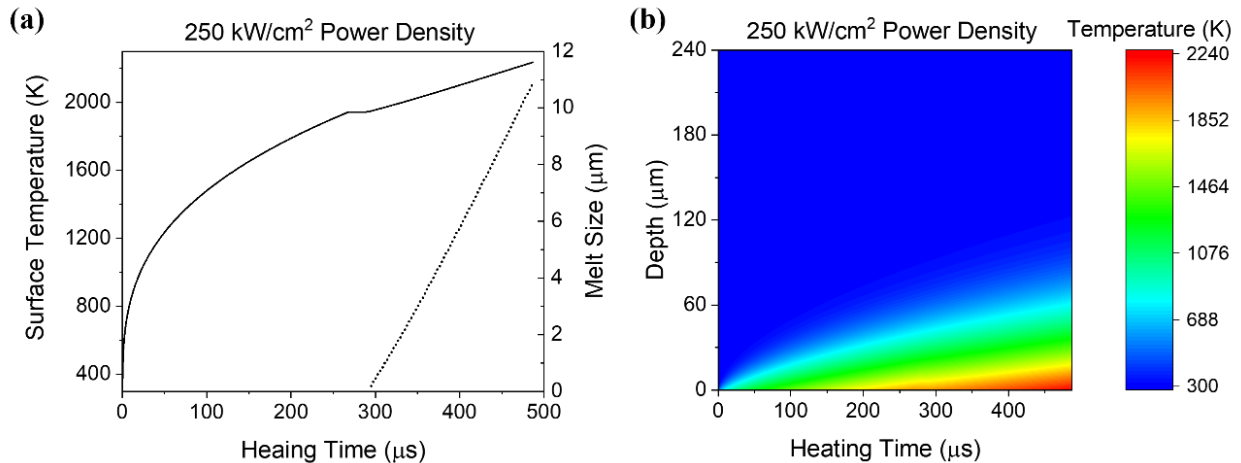
Figure 2-3. (a) Surface temperature (solid line) and melt size (dotted line) as a function of heating time for a 250 kW/cm^2 laser power density incident on Ti-6Al-4V. *(b)* Calculated temperature field as a function of heating time and depth for the 250 kW/cm^2 power density.

REFERENCES

1. Morales, R. E., Harke, K. J., Tringe, J. W., Stobbe, D. M. & Murray, T. W. Real-time laser ultrasonic monitoring of laser-induced thermal processes. *Sci Rep* **12**, 9865 (2022).

2. Singh, R. K. & Narayan, J. A novel method for simulating laser-solid interactions in semiconductors and layered structures. *Materials Science and Engineering: B* **3**, 217–230 (1989).

3. Ozisik, M. N., *Finite Difference Methods in Heat Transfer* (CRC Press, 1994).

4. Richtmyer, R. D., *Difference Methods for Initial Value Problems* (Interscience, New York, 1957).

5. Murray, T.W., *Laser interaction with materials: Optimizing the laser source for the generation of acoustic waves in laser ultrasonic applications*. Johns Hopkins University (1998).

6. Murray, T. W. & Wagner, J. W. Laser generation of acoustic waves in the ablative regime. *Journal of Applied Physics* **85**, 2031–2040 (1999).

7. Welsch, G., Boyer, R. & Collings, E. W. *Materials properties handbook: titanium alloys*. (ASM International, 1994).

8. Smithells, C. J., Gale, W. F. & Totemeier, T. C. *Smithells metals reference book*. (Elsevier Butterworth-Heinemann, 2004).

9. Mills, K. C. *Recommended values of thermophysical properties for selected commercial alloys*. (Woodhead, 2002).

10. Casas, J., Kéita, N. M. & Steinemann, S. G. Sound Velocity in Liquid Titanium, Vanadium and Chromium. *Physics and Chemistry of Liquids* **14**, 155–158 (1984).

11. Ready, J. F. *Effects of high-power laser radiation*. (Academic Press, 1971).

12. Wood, R. F. & Giles, G. E. Macroscopic theory of pulsed-laser annealing. I. Thermal transport and melting. *Phys. Rev. B* **23**, 2923–2942 (1981).

CHAPTER 3. LASER ULTRASONICS THEORETICAL MODEL

3.1 Formulating the Problem

Acoustic signals generated by a laser source in a layered system must be well understood to use laser ultrasonics for the study of surface acoustic wave interaction with a laser-heated region. There is a significant amount of work in the theoretical formulation for laser ultrasonic wave generation in a semi-infinite half-space[1-3], in a homogeneous, isotropic plate[4-6], and in isotropic single or multi-layer films on a semi-infinite substrate[7,4]. The theoretical approach presented by Cheng *et al.*[4] is employed in this work to model the pulsed laser excitation and interferometric detection of the CW laser-heated surface that results from the one-dimensional thermal model described in Chapter 2.

The material near the surface is discretized into a temperature-dependent multi-layered plate consisting of *n* homogeneous, isotropic, and linearly elastic layers of equal thickness on top of a homogeneous, isotropic, and linearly elastic half-space. The excitation laser source is represented as an equivalent elastic boundary source consisting of distributed normal and shear loading on the plate surface[4,5,9], and the transfer matrix technique[10] is used to enforce the continuity of stress and displacement across all homogeneous and isotropic layer boundaries. The problem is solved in cylindrical coordinates using the integral transform technique where a Hankel transform of the elastic wave equation is taken with respect to the radial coordinate (*r*) and a Laplace transform is taken with respect to time. The normal surface displacement as a function of time at a given *r* is found through numerical inversion of the Hankel-Laplace transforms. The formulation of this problem as presented in detail by Cheng *et al.*[4] and is summarized below.

3.2 Governing Equations of Elasticity

We begin with the governing equation for the axially symmetric elastic wave problem in a linearly elastic, isotropic, homogeneous material which can be written as

$$(\lambda + \mu)\nabla\nabla \cdot u + \mu\nabla^2 u = \rho\frac{\partial^2 u}{\partial t^2} \qquad [1]$$

where u is displacement, ρ is density, and λ and μ are Lamé parameters. For a cylindrical system, the Helmholtz decomposition used to represent the displacement component normal to the surface can be written as

$$u_z = \frac{\partial\phi}{\partial r} - \frac{\partial\psi}{\partial z} \qquad [2]$$

where ϕ is the scalar potential and ψ is the vector potential (θ component only). The governing elastic wave equation, also known as Navier's governing equation, Equation 1 can be written in terms of this Helmholtz decomposition.

$$\nabla\left[(\lambda + 2\mu)\nabla^2\phi - \rho\frac{\partial^2\phi}{\partial t^2}\right] + \nabla \times \left[\mu\nabla^2\psi - \rho\frac{\partial^2\psi}{\partial t^2}\right] = 0 \qquad [3]$$

This governing equation can then be decomposed into the following set of equations

$$(\lambda + 2\mu)\nabla^2\phi - \rho\ddot{\phi} = 0 \qquad [4]$$

$$\mu\nabla^2\psi - \rho\ddot{\psi} = 0 \qquad [5]$$

which can be simplified in terms of longitudinal and shear wave speeds, c_L and c_T, respectively.

$$\nabla^2\phi - \frac{1}{c_L^2}\ddot{\phi} = 0 \qquad [6]$$

$$\nabla^2\psi - \frac{1}{c_T^2}\ddot{\psi} = 0 \qquad [7]$$

where $c_L = \sqrt{(\lambda + 2\mu)/\rho}$ and $c_T = \sqrt{\mu/\rho}$. Given the assumed axisymmetric beam profile of the laser source, this problem is best solved in a cylindrical coordinate system, so Equations 6-7 are re-written as

$$\frac{\partial^2 \phi}{\partial r^2} + \frac{1}{r}\frac{\partial \phi}{\partial r} + \frac{\partial^2 \phi}{\partial z^2} = \frac{1}{c_L^2}\frac{\partial^2 \phi}{\partial t^2} \tag{8}$$

$$\frac{\partial^2 \psi}{\partial r^2} + \frac{1}{r}\frac{\partial \psi}{\partial r} + \frac{\partial^2 \psi}{\partial z^2} - \frac{\psi}{r^2} = \frac{1}{c_T^2}\frac{\partial^2 \psi}{\partial t^2} \tag{9}$$

3.3 Solution of the Elastic Problem

The corresponding displacements and stresses in the cylindrical coordinate system can be expressed as

$$u_z = \frac{\partial \phi}{\partial r} - \frac{\partial \psi}{\partial z} \tag{10}$$

$$w = \frac{\partial \phi}{\partial z} + \frac{1}{r}\frac{\partial(r\psi)}{\partial r} \tag{11}$$

$$\tau_{zr} = \mu\left(\frac{\partial u}{\partial z} + \frac{\partial w}{\partial z}\right) \tag{12}$$

$$\tau_z = (\lambda + 2\mu)\frac{\partial w}{\partial z} + \frac{\lambda}{r}\frac{\partial(ru)}{\partial r} \tag{13}$$

Hankel and one-sided Laplace transforms are then applied to Equations 8 and 9 to yield

$$\overline{\frac{\partial^2 \phi}{\partial z^2}}^{H_0} - \alpha^2 \bar{\phi}^{H_0} = 0 \tag{14}$$

$$\overline{\frac{\partial^2 \psi}{\partial z^2}}^{H_1} - \beta^2 \bar{\psi}^{H_1} = 0 \tag{15}$$

where the bar represents the Laplace transform, and H_0 and H_1 are the Hankel transforms of order zero and unity, respectively. Here, $\alpha^2 = \xi^2 + p^2/c_L^2$ and $\beta^2 = \xi^2 + p^2/c_T^2$ where ξ and p

represent the spatial frequency and the time frequency, respectively. For a layer, the solutions of $\bar{\phi}^{H_0}$ and $\bar{\psi}^{H_1}$ are

$$\bar{\phi}^{H_0} = A(\xi,p)e^{-\alpha z} + B(\xi,p)e^{\alpha z} \qquad [16]$$

$$\bar{\psi}^{H_1} = C(\xi,p)e^{-\beta z} + D(\xi,p)e^{\beta z} \qquad [17]$$

where constants A, B, C, and D are functions of ξ and p. These Laplace and Hankel transforms can then be applied to the displacements and stresses in Equations 10-13.

3.4 Elastic Boundary Conditions

The initial conditions for a plate at rest prior to time $t=0$ are as follows

$$\phi(r,z,0) = \frac{\partial \phi}{\partial t}(r,z,0) = \psi(r,z,0) = \frac{\partial \psi}{\partial t}(r,z,0) \equiv 0 \qquad [18]$$

The boundary conditions at the top and bottom surface of each plate ($z = z \pm h/2$) can be written in the Laplace and Hankel domain as the following

$$\bar{\tau}_{zr}^{H_1}(z = z_1 - h_1/2) = \bar{g}^{H_1}(\xi,p) \qquad [19]$$

$$\bar{\tau}_z^{H_0}(z = z_1 - h_1/2) = \bar{f}^{H_0}(\xi,p) \qquad [20]$$

$$\bar{\tau}_{zr}^{H_1}(z = z_n + h_n/2) = 0 \qquad [21]$$

$$\bar{\tau}_z^{H_0}(z = z_n + h_n/2) = 0 \qquad [22]$$

These boundary conditions set stresses and displacements on the bottom of layer n equal to the stresses and displacements on the top of layer $n+1$. On the top surface of the layered system, equivalent elastic boundary sources $\bar{g}^{H_1}(\xi,p)$ and $\bar{f}^{H_0}(\xi,p)$ are used to represent acoustic wave generation by an incident laser pulse and are given by

$$\bar{g}^{H_1}(\xi, p) = -2\frac{\xi}{p}C_0 Q_0 Q(\xi)Q(p) \qquad [23]$$

$$\bar{f}^{H_0}(\xi, p) = -\frac{\beta^2 + \xi^2}{p\chi}C_0 Q_0 Q(\xi)Q(p) \qquad [24]$$

where $\chi = \alpha^2 + p/\kappa$, κ is the thermal diffusion coefficient, C_0 is a constant related to the thermal and elastic properties of the top layer, and $Q_0 Q(\xi)Q(p)$ is the Hankel and Laplace transform of the laser source function $Q(r,t)$ given as

$$Q(r,t) = Q_0 \left[\frac{2}{R^2}\exp\left(-\frac{2r^2}{R^2}\right)\right]\left[\frac{8t^3}{\tau^4}\exp\left(-\frac{2t^2}{\tau^2}\right)\right] \qquad [25]$$

where R is the beam radius of the Gaussian excitation pulse, τ is the laser pulse rise time, and Q_0 is the amplitude of the heating produced by the photothermal effect[4,5,7]. This source allows the thermoelastic problem of transient acoustic wave generation by a laser source to be simplified to a purely elastic problem. The spatial and temporal distributions of the incident laser pulse are both assumed to be Gaussian. This laser source representation assumes that the heating is localized to the surface layer and that the point of observation is outside of the volume defined by significant thermal diffusion, which holds if the thermal diffusion length $\sqrt{4\kappa\tau}$ is sufficiently smaller than the top layer thickness and the source to receiver distance, respectively. Another assumption is that the optical energy is converted to heat close to the irradiated boundary, which holds if the top layer material is a strong absorber at the generation laser wavelength[4].

3.5 Transfer Matrix Technique

With the Laplace and Hankel transforms applied to the displacements and stresses in Equations 10-13, the transfer matrix method[10] is used to relate the stresses and displacements at the top surface of each layer to those at the bottom surface to obtain a layer transfer matrix M_j for each layer. Continuity conditions at all layer interfaces are then used from layer 1 to n to derive a

total transfer matrix T which transfers the displacements and stresses from one side of the layered system to the other side. This total transfer matrix is the product of all transfer matrices across each of the layers.

$$T = \prod_{i=1}^{n} M_i \qquad [26]$$

Since our model consists of layered system on a half space, a transfer matrix M_{n+1} is also obtained for the semi-infinite substrate following a similar procedure as that described above, but in a simpler manner due to the upgoing bulk wave modes vanishing in a half space. The total transfer matrix of the system T^* is thus the product of the total transfer matrix of the layers T and the transfer matrix M_{n+1} for the half space.

3.6 Transient Response

The boundary conditions at the top and bottom surfaces (Equations 19-22) are used with the total transfer matrix to yield the displacement as a function of the spatial and time frequencies, ξ and p, respectively, at the top surface of the layered system in the Hankel and Laplace domains. The transient response of the layered system under laser source illumination can now be obtained by numerically solving the inverse Laplace and Hankel transforms as

$$u(r,t) = \frac{1}{2\pi i} \int_0^\infty \left(\int_{a-i\infty}^{a+i\infty} \bar{u}^{H_1}(\xi,p) e^{pt} dp \right) J_1(r\xi) \xi d\xi \qquad [27]$$

$$w(r,t) = \frac{1}{2\pi i} \int_0^\infty \left(\int_{a-i\infty}^{a+i\infty} \bar{w}^{H_0}(\xi,p) e^{pt} dp \right) J_0(r\xi) \xi d\xi \qquad [28]$$

where a is a real arbitrary constant. Numerical techniques are necessary for these calculations as it is very difficult to solve these inverse transforms analytically for a multi-layered system. The numerical technique employed here is described in detail by Cheng *et al.*[4]

3.7 Surface Acoustic Waves in a Molten Liquid-Solid Layered System

At sufficiently high heating powers, melting will occur and as such, it is important to study acoustic waves in a liquid-solid layered system, such as the one depicted in Figure 3-1. Scholte surface waves and leaky Rayleigh waves arise between an ideal fluid half-space and an isotropic solid medium half-space. Rayleigh surface waves change to leaky Rayleigh waves because the longitudinal waves are radiated into the fluid layer[11]. However, if the longitudinal wave speed of the liquid is greater than the shear wave speed of the solid, as is common in most metals, these leaky Rayleigh waves do not exist for an infinite liquid layer. The Scholte waves appear at small wavelengths and they propagate with a phase velocity lower than that of the liquid layer[12]. In general, the velocity of waves propagating on a liquid-covered half space transition from the Rayleigh wave velocity at zero thickness to the Scholte wave velocity when the thickness of the liquid is large with respect to the wavelength[12,13].

Figure 3-1. Schematic of the model used to study guided wave propagation at the interface between a liquid layer of finite thickness h and a solid.

The Scholte wave speed c_S is determined by solving the characteristic equation shown below in Equation 29, where c_{Li} is the longitudinal wave speed in the ith medium ($i = 1$ for the solid layer, $i = 2$ for the fluid layer), c_{Ti} is the shear wave speed, and ρ_i is the density[13]. The resulting Scholte wave speed for a liquid-solid layer of Titanium alloy Ti-6Al-4V, with properties[14-17] listed in Table II, is $c_S = 2469$ m/s.

29

$$4\xi_{L1}\xi_{T1} - (1 + \xi_{T1}^2)^2 = m(1 - \xi_{T1}^2)^2 \frac{\xi_{L1}}{\xi_{L2}}$$

$$\xi_{Li} = \sqrt{1 - \frac{c_S^2}{c_{Li}^2}} \quad \text{for } i = 1,2$$

$$\xi_{T1} = \sqrt{1 - \frac{c_S^2}{c_{T1}^2}}$$

[29]

$$m = \frac{\rho_2}{\rho_1}$$

Table II. Material properties of solid and liquid Ti-6Al-4V.

Solid		
	Longitudinal Velocity, c_{l1}	6130 m/s
	Shear Velocity, c_{t1}	3182 m/s
	Density, ρ_1	4420 kg/m^3
Liquid	Longitudinal Velocity, c_{l2}	4407 m/s
	Density, ρ_2	3920 kg/m^3

For a finite liquid layer of thickness h, we can calculate an analytical dispersion curve to track the wave velocity c as a function of the product of frequency and thickness with the following equation

$$4\sqrt{1 - \zeta_1^2} - \frac{(2 - \zeta_1^2)^2}{\sqrt{1 - \zeta_2^2}} = \frac{\rho_2}{\rho_1} \frac{\zeta_1^4}{\sqrt{1 - \zeta^2}} \tanh\left[lh\sqrt{1 - \zeta^2}\right] \quad \text{for } \zeta < 1$$

$$\zeta_1 = \frac{c_{l2}}{c_{t1}}\zeta, \quad \zeta_2 = \frac{c_{l2}}{c_{l1}}\zeta$$

[30]

$$c = \zeta c_{l2}$$

Here, $lh = 2\pi h/\lambda$ where h is the fluid layer thickness and λ is the wavelength. Equation 30 is solved as a function of frequency f by using the relation $(c/c_{l2})lh = fh/c_{l2}$ as explained by Biot[12]. The solution to this characteristic equation for the analytical dispersion curve of a Ti-6Al-4V

liquid-solid layer with material properties listed in Table II is plotted in Figure 3-2. For this liquid-solid layered model with a finite thickness liquid, the velocity starts at the Rayleigh wave speed of Titanium at room temperature, $c_R = 2958$ m/s, for low frequencies and very thin liquid layers of thicknesses close to zero ($h \approx 0$). The velocity decreases to the Scholte wave speed of $c_S = 2469$ m/s for increasing thickness of the liquid layer h and higher frequencies.
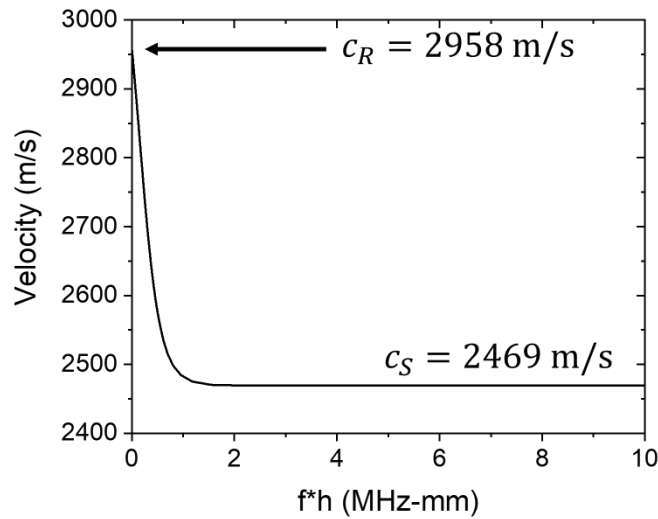
Figure 3-2. Analytical dispersion curve calculated for a Ti-6Al-4V liquid layer on top of a Ti-6Al-4V solid at room temperature.

The same formulation as described in Sections 1-6 of this chapter is followed to numerically study guided wave propagation along the interface between a liquid-solid layered system. In this model, we only use a single layer with liquid metal properties on top of semi-infinite substrate with room temperature properties, as depicted in Figure 3-1. We calculate acoustic responses of the displacement normal to the surface as a function of time at many source-to-detector distances to have a 2-D data set of displacement as a function of time and space. We then use the 2-D FFT technique[18] to calculate dispersion curves for this liquid-solid layered system. The 2-D acoustic data set is Fourier transformed into temporal frequency f and spatial frequency

k, which is also known as the wavenumber and is defined below in Equation 31. The peaks of this *f-k* 2-D FFT correspond to the modes of the system. The dominant mode is the surface acoustic wave mode in this case. Finally, using the temporal and spatial frequencies *f* and *k* corresponding to the peaks, or the SAW mode, we can calculate the dispersion curve with Equation 32 to show the phase velocity dependence on frequency.

$$k = \frac{2\pi}{x} \qquad\qquad [31]$$

$$c = \frac{2\pi f}{k} \qquad\qquad [32]$$

Figure 3-3 shows the resulting dispersion curves calculated for a 50 μm liquid layer of pure Titanium using the analytical characteristic equation, Equation 30, and the 2-D model described above. Note that pure Titanium and not Ti-6Al-4V were used here. The difference between the two materials are the densities with solid density $\rho_1 = 4508$ kg/m^3 and liquid density $\rho_2 = 4208$ kg/m^3 for pure Titanium. For these material properties, the resulting Scholte wave speed is $c_S = 2447$ m/s. As shown in Figure 3-3, the velocity of the surface acoustic waves in the 2-D model starts at the Titanium room temperature Rayleigh wave speed, 2958 m/s, for low frequencies and converges to the Scholte wave speed at higher frequencies. The model results agree with the analytical solution except for numerical noise that is present in the simulation results at lower frequencies.

The dispersion resulting from this liquid-solid layer interactions will be characteristic of the liquid layer thickness. Temperature fields induced by laser-heating is neglected in this discussion but will also influence the dispersion characteristics of the surface acoustic wave. In the next chapter, we dive into studying the effects of temperature and surface melting on surface acoustic wave propagation.
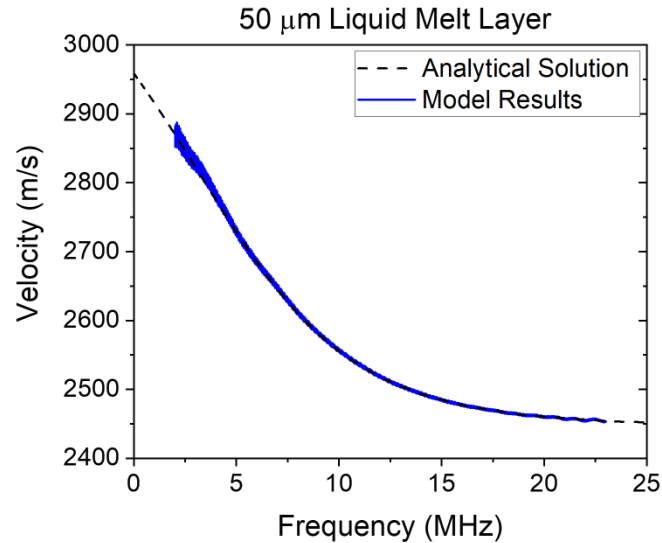
Figure 3-3. Dispersion curves calculated for a liquid Titanium layer of 50 μm thickness on top of a semi-infinite Titanium substrate at room temperature using the characteristic equation (dashed curve) and with the 2-D model (solid blue curve).

REFERENCES

1. Rose, J. L. *Ultrasonic waves in solid media*. (Cambridge University Press, 1999).

2. McDonald, F. A. On the precursor in laser-generated ultrasound waveforms in metals. *Appl. Phys. Lett.* **56**, 230–232 (1990).

3. Sanderson, T., Ume, C. & Jarzynski, J. Laser generated ultrasound: a thermoelastic analysis of the source. *Ultrasonics* **35**, 115–124 (1997).

4. Spicer, J. B., McKie, A. D. W. & Wagner, J. W. Quantitative theory for laser ultrasonic waves in a thin plate. *Appl. Phys. Lett.* **57**, 1882–1884 (1990).

5. Spicer, J. B. *Laser Ultrasonics in Finite Structures: Comprehensive Modeling with Supporting Experiment*. Johns Hopkins University (1991).

6. Cheng, J., Wu, L. & Zhang, S. Thermoelastic response of pulsed photothermal deformation of thin plates. *Journal of Applied Physics* **76**, 716–722 (1994).

7. Murray, T. W., Krishnaswamy, S. & Achenbach, J. D. Laser generation of ultrasound in films and coatings. *Appl. Phys. Lett.* **74**, 3561–3563 (1999).

8. Cheng, A., Murray, T. W. & Achenbach, J. D. Simulation of laser-generated ultrasonic waves in layered plates. *The Journal of the Acoustical Society of America* **110**, 848–855 (2001).

9. Rose, L. R. F. Point-source representation for laser-generated ultrasound. *The Journal of the Acoustical Society of America* **75**, 723–732 (1984).

10. Thomson, W. T. Transmission of Elastic Waves through a Stratified Solid Medium. *Journal of Applied Physics* **21**, 89–93 (1950).

11. Bertoni, H. L. & Tamir, T. Unified theory of Rayleigh-angle phenomena for acoustic beams at liquid-solid interfaces. *Appl. Phys.* **2**, 157–172 (1973).

12. Biot, M. A. The interaction of Rayleigh and Stoneley waves in the ocean bottom*. *Bulletin of the Seismological Society of America* **42**, 81–93 (1952).

13. Meegan, G. D., Hamilton, M. F., Il'inskii, Yu. A. & Zabolotskaya, E. A. Nonlinear Stoneley and Scholte waves. *The Journal of the Acoustical Society of America* **106**, 1712–1723 (1999).

14. Welsch, G., Boyer, R. Collings, E.W. *Materials properties handbook: titanium alloys*. (ASM International, 1994).

15. Smithells, C. J., Gale, W. F. & Totemeier, T. C. *Smithells metals reference book*. (Elsevier Butterworth-Heinemann, 2004).

16. Mills, K. C. *Recommended values of thermophysical properties for selected commercial alloys*. (Woodhead, 2002).

17. Casas, J., Kéita, N. M. & Steinemann, S. G. Sound Velocity in Liquid Titanium, Vanadium and Chromium. *Physics and Chemistry of Liquids* **14**, 155–158 (1984).

18. Alleyne, D. & Cawley, P. A two-dimensional Fourier transform method for the measurement of propagating multimode signals. *The Journal of the Acoustical Society of America* **89**, 1159–1168 (1991).

CHAPTER 4. THEORETICAL MODEL TO STUDY SURFACE ACOUSTIC WAVE INTERACTION WITH LASER-HEATED REGIONS

4.1 Temperature Dependence of Mechanical Properties

The thermal and elastic properties of materials are dependent on temperature, with an increase in temperature generally resulting in a decrease in both material density and stiffness. We first consider a uniformly heated sample of a titanium alloy (Ti-6Al-4V) that is assumed to be homogeneous and isotropic. The temperature-dependent density ρ, elastic modulus E, and Poisson's ratio σ are obtained from the software *JMatPro*[1] for temperatures below melting and are used to calculate longitudinal, c_L, and shear, c_T, wave speeds as a function of temperature. The software *JMatPro* quantitatively calculates thermophysical properties and behavior of alloys utilizing thermodynamic modeling augmented with theoretical material models and property databases[1]. From *JMatPro*, we export data sets of the desired properties as a function of temperature. Figure 4-1 shows the temperature-dependent properties we use for Ti-6Al-4V.
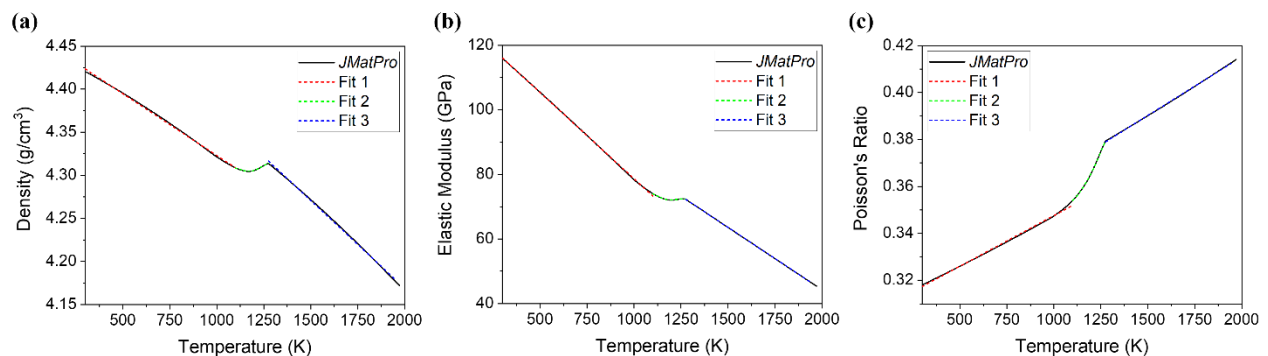
Figure 4-1. Temperature-dependent properties of **(a)** density ρ, **(b)** elastic modulus E, and **(c)** Poisson's ratio σ exported from *JMatPro* and the curve fits for temperatures ranges: 300-1100 K plotted in red, 1100-1275K plotted in green, and 1275-1943 K plotted in blue.

Overall, density and elastic modulus decrease with increasing temperature while Poisson's ratio increases. This is all due to decreasing bond strength on the microscopic level which leads to

material softening. As shown in these plots, there is a region between 1100 and 1275 K where the properties behave differently. These temperatures correspond to Ti-6Al-4V undergoing an hcp (α) – bcc (β) phase transformation as is typical for group-IV metals and their alloys[2]. We curve fit the data from *JMatPro* to get functional forms of these temperature-dependent properties for calculating resulting wave speeds as a function of temperature. The curve fitting is performed for three separate temperature ranges to account for the phases present in the material: 300-1100 K for the α phase, 1100-1275 K for the α – β transition region, and 1275-1943 K for the β phase. The resulting functional form of the temperature dependent properties is the following, in units of kg/m^3 and Pa for density and elastic modulus, respectively, and unitless Poisson's ratio.

$\rho(T)$

$$= \begin{cases} 4466.5 - 0.14346T, & 300 < T \leq 1100 \\ -1.062\text{E}5 + 377.1T - 0.4814T^2 + 2.724\text{E-}4T^3 - 5.767\text{E-}8T^4, & 1100 < T \leq 1275 \\ 4576.8 - 0.20406T, & 1275 < T < 1943 \end{cases} \quad [1]$$

$E(T)$

$$= \begin{cases} 1.3211\text{E}11 - 5.3476\text{E}7T, & 300 < T \leq 1100 \\ -2.861\text{E}13 + 9.81\text{E}10T - 1.255\text{E}8T^2 + 7.12\text{E}4T^3 - 15.116T^4, & 1100 < T \leq 1275 \\ 1.2157\text{E}11 - 3.8674\text{E}7T, & 1275 < T < 1943 \end{cases} \quad [2]$$

$$\sigma(T) = \begin{cases} 0.30444 + 4.3136\text{E-}5T, & 300 < T \leq 1100 \\ 0.71057 + 7.3107\text{E-}4T + 3.6983\text{E-}7T^2, & 1100 < T \leq 1275 \\ 0.31529 - 4.9955\text{E-}5T, & 1275 < T < 1943 \end{cases} \quad [3]$$

These temperature-dependent properties are then used to determine longitdinal, c_L, and shear, c_T, wave speeds as a function of temperature with Equations 4 and 5.

$$c_L(T) = \sqrt{E(T)\big(1 - \sigma(T)\big)/\big(\rho(T)\big(1 - 2\sigma(T)\big)\big(1 + \sigma(T)\big)\big)} \quad [4]$$

$$c_T(T) = \sqrt{G(T)/\rho(T)} \quad [5]$$

where $G(T) = E(T)/\big(2(1 + \sigma(T))\big)$. These values are, in turn, used to calculate Rayleigh velocity, which is the speed at which surface acoustic waves travel, using the characteristic equation[3], Equation 6.

$$\left(\frac{c_R(T)}{c_T(T)}\right)^6 - 8\left(\frac{c_R(T)}{c_T(T)}\right)^4 + 8\left(\frac{c_R(T)}{c_T(T)}\right)^2\left(3 - 2\left(\frac{c_T(T)}{c_L(T)}\right)^2\right) + 16\left(\left(\frac{c_T(T)}{c_L(T)}\right)^2 - 1\right) = 0 \quad [6]$$

The result is shown in Figure 4-2 where the Rayleigh wave velocity is seen to decrease from 3000 m/s at room temperature (293 K) to 1880 m/s at the melting temperature of 1943 K. The decrease is relatively monotonic outside of small region between 1100 and 1275 K, the temperature range at which Ti-6Al-4V undergoes an $\alpha - \beta$ phase transformation. In the case of uniform heating, the thermal field and elastic properties are not depth-dependent, and the Rayleigh waves propagate without dispersion.
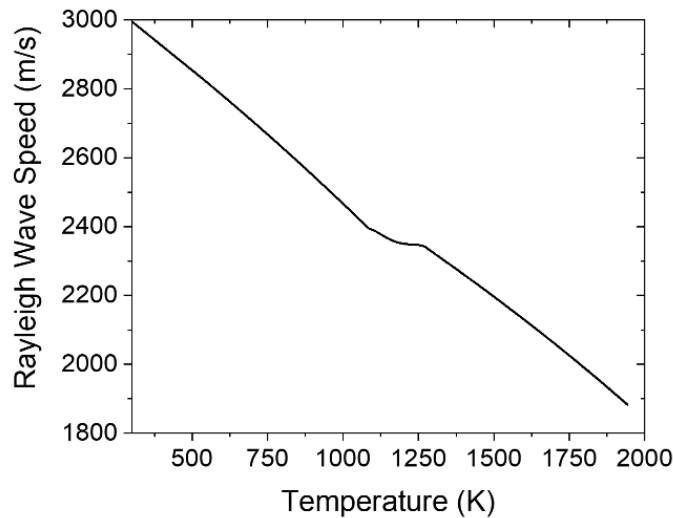
Figure 4-2. Rayleigh wave velocity, c_R, of Ti-6Al-4V as a function of temperature ranging from room temperature to the melting temperature of 1943 K.

Rayleigh wave propagation becomes more complex in the case of transient heating, such as that produced by a high power laser source, as the thermal field and temperature-dependent

elastic properties are functions of both time and space. Furthermore, the thermal properties are also temperature-dependent and, at sufficiently high heating powers, the material will undergo a phase transformation resulting in surface melt.

4.2 Coupling of Thermal Model and Acoustic Wave Generation

The final solution for the elastic displacement response generated by a nanosecond pulsed laser source incident upon a surface that is being heated by a spatially uniform continuous wave (CW) laser with a step-function time dependence requires a coupling of the thermal model described in Chapter 2 with the elastic wave solutions presented in Chapter 3. The coupled problem is solved using the numerical routine written in C++ included in Appendix I. We begin by calculating the one-dimensional temperature field produced by a CW laser using the implicit finite difference method which allows for the calculation of the temperature as a function of depth and melt front position at any time after the heating laser is turned on. Next, we model the pulsed laser excitation and interferometric detection of the CW laser-heated surface at a given time. The material near the surface is discretized into 400 layers, with a layer thickness of 0.6 μm, the elastic properties of each layer are calculated from the mean temperature of the layer, and the elastic wave propagation problem is then reduced to an analogous problem of wave propagation in a homogeneous, isotropic layered media. This model is thus an extension of the work done to study laser generation of ultrasound in plates on a semi-infinite substrate[4,5] and is combined with the implicit finite difference thermal model[6]. Following these numerical methods, we built a 2D model that calculates the time domain displacement of a layered system consisting of temperature-dependent mechanical properties on top of a semi-infinite substrate, as shown in Figure 4-3, where each layer consists of temperature-dependent density, ρ, longitudinal speed, c_L, and shear speed, c_T.
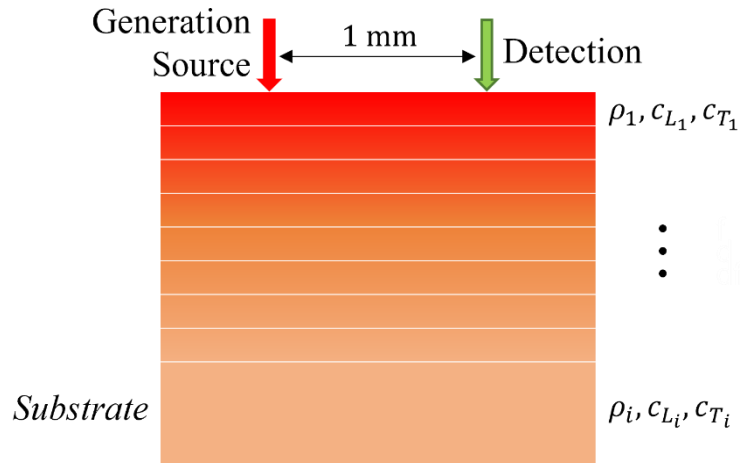
Figure 4-3. Schematic of the thermo-acoustic layered model with temperature-dependent properties.

We first calculate the depth-dependent temperature distributions resulting from a continuous laser source at a certain power density incident on the sample. Next, we calculate temperature-dependent mechanical properties resulting from these temperature distributions, we apply the properties to their corresponding depth to create the layered model, and we use the acoustic model to generate acoustic signals with a point source 1 mm away from the detection point on the surface. We first step through the chosen heating time in discrete steps and solve the one-dimensional laser heating problem as we step through space to get the depth-dependent temperature distribution resulting from a CW laser source at a certain power density incident on the sample at that time step n. This process is then repeated for the next heating time step $n + 1$. A schematic of this process is shown in Figure 4-4.
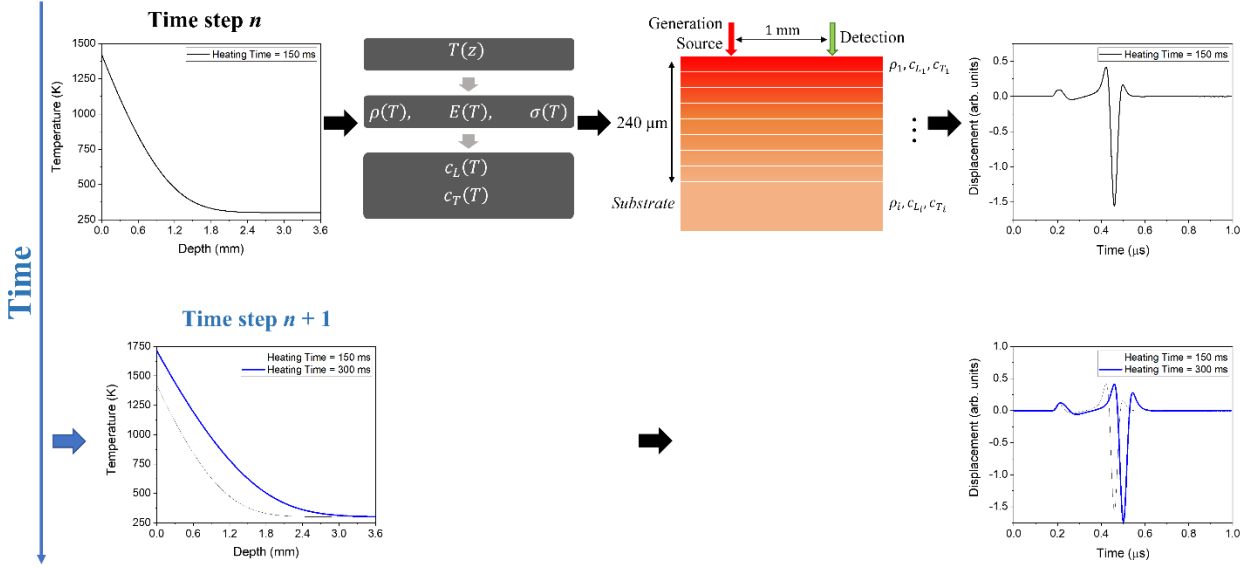
Figure 4-4. Schematic of model implementation. We step through time, and at each time point *n*, we calculate temperature-dependent properties and create a layered acoustic model for which we calculate ultrasonic responses.

When surface melting occurs, the thickness of the surface layer is set as the thickness of the melt pool and the density[7] (3920 kg/m^3)and longitudinal wave velocity[8] (4407 m/s) of liquid Ti-6Al-4V are used. A shear wave velocity of nearly zero is used in the model because shear waves are known not to propagate in liquids. The acoustic calculations in the algorithm cannot be performed if the shear speed is exactly zero, so we choose a small acoustic speed of 44 m/s. These liquid properties are listed in Table III. The remainder of the geometry below the melt is again discretized into 0.6 μm thick temperature-dependent layers. The excitation laser spot size was set to 100 μm full width at half maximum (FWHM) with a detection location at $r = 1.0$ mm.

Table III. Properties of liquid Ti-6Al-4V used in the model.

Density, ρ	3.920 g/cm^3
Longitudinal velocity, c_L	4.407 mm/μs
Shear velocity, c_T	0.044 mm/μs

4.3 Surface Acoustic Wave Interaction with Slow Laser-Heating

Surface acoustic waves are confined to propagate in the near surface region with a penetration depth on the order of the wavelength. For a frequency of 30 MHz, for example, surface waves in Ti-6Al-4V will be sensitive to mechanical property changes that occur over a depth of approximately 100 μm. The temperature field calculated in Section 2.3 for a heating laser power of 6 kW/cm^2 will be referred to here and is included again in Figure 4-5(a) and (b). In Figure 4-5(b), the temperature rise is somewhat uniform over the near surface region, and thus we expect that the mechanical property changes will also be relatively constant over the penetration depth, resulting in a surface acoustic wave delay that is frequency independent.

The normal surface displacement as a function of time is given in Figure 4-5(c) for the 6 kW/cm^2 heating power. The top curve gives the room temperature response in the absence of CW surface heating. A small amplitude wave arrival corresponding to the surface skimming longitudinal wave is seen at 0.16 μs followed by the larger surface acoustic wave (SAW) amplitude arrival at about 0.30 μs. The other curves show the displacement response at various times after the CW heating laser is turned on. For the signals between $t = 0$ and $t = 450$ ms, the shape of the surface acoustic wave remains relatively uniform, but the arrival is delayed as heating proceeds. During the last three time steps of $t = 508.5$, 517.0, and 525.6 ms, melting has occurred with melt depths of 6.0, 16.8 and 27.0 μm, respectively. More prominent dispersion is seen when the surface waves traverse the molten layer; the higher frequency, short wavelength, components are delayed due to the strong interaction with the melt layer. Note that in this case, the longitudinal wave velocity in the molten liquid is higher than the shear wave velocity in the substrate so the surface waves are not leaky[8]. In general, the velocity of waves propagating on a liquid-covered half space transition from the Rayleigh wave velocity at zero thickness to the Scholte wave velocity when

the thickness of the liquid is large with respect to the wavelength[9,10], as was described in Section 2.5.
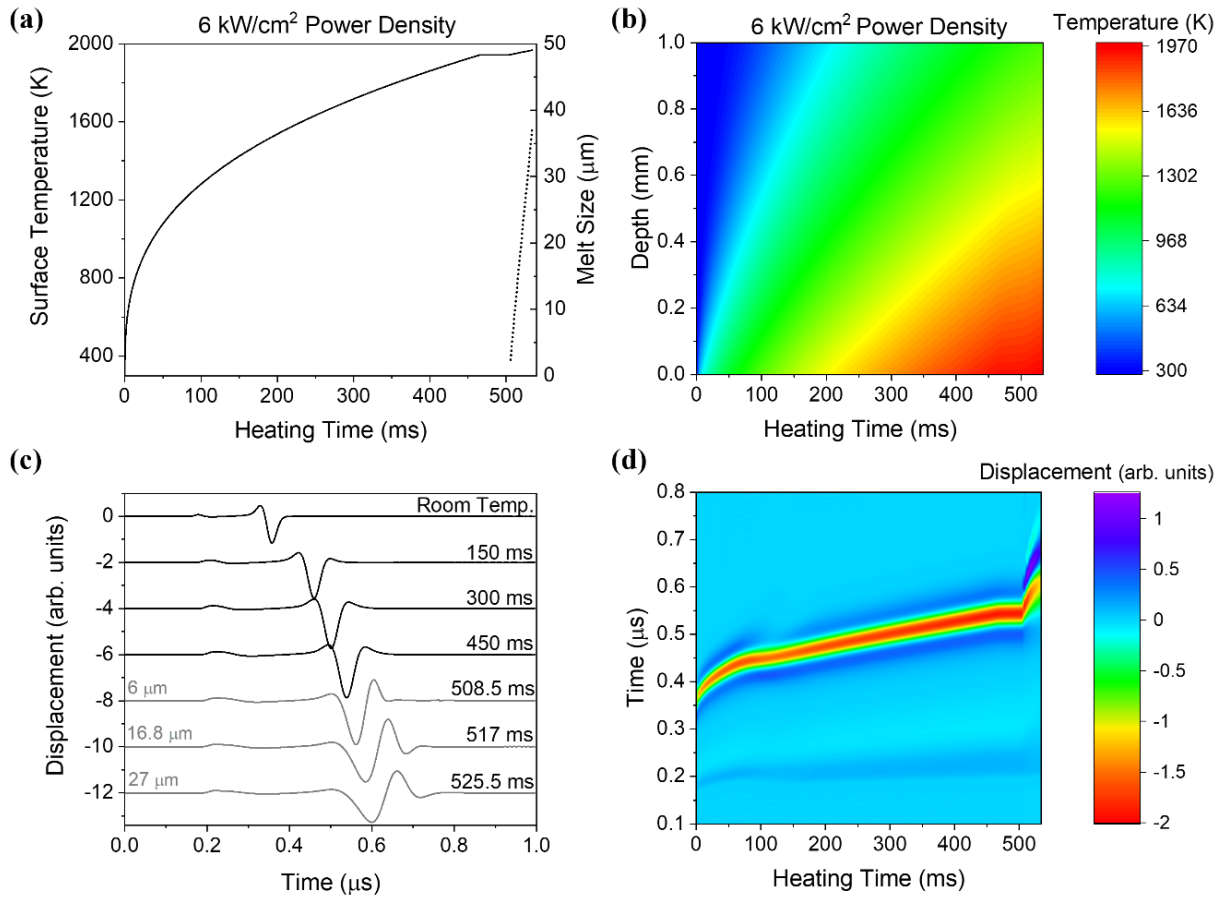
Figure 4-5. *(**a**)* Surface temperature (left axis) and melt size (right axis) as a function of heating time for a constant 6 kW/cm^2 power density incident on Ti-6Al-4V. *(**b**)* Calculated temperature field as a function of heating time and depth. *(**c**)* Calculated laser ultrasonic signals with a source to detector distance of 1.0 mm at room temperature and heating times of 150.0, 300.0, 450.0, 508.5, 517.0, and 525.5 ms. *(**d**)* Temporal evolution of the displacement field for the 6 kW/cm^2 power density.

Figure 4-5(d) shows the evolution of the displacement field calculated throughout the heating time. Here, the abscissa gives the time after the heating laser is turned on while the ordinate gives the time after the excitation laser pulse. The color bar represents the normal displacement of the surface. In this image, the SAW arrival has the largest negative amplitude and is shown in red. The initial pronounced change in the SAW arrival time is associated with the rapid rise in the near

42

surface temperature as seen in Figure 4-5(a) and (b). The SAW arrival time is then relatively constant between 75 and 100 ms during which the α – β phase transformation in the Ti-6Al-4V occurs. After this transition region, the arrival of the SAW continues to be delayed with heating time in a monotonic fashion until approximately 508 ms where a sharp break in the curve associated with surface melting is observed. The SAW signal sensitivity to the presence of melt makes it an attractive option for sensing melt depth.

4.4 Surface Acoustic Wave Interaction with Rapid Laser-Heating

The surface temperature for a significantly higher heating power of 250 kW/cm^2, which was discussed in Section 2.4, is shown here again in Figure 4-6(a). The thermal gradients observed in Figure 4-6(b) can cause dispersion of surface waves since the high frequency waves, with a shorter wavelength, will be more influenced by the near surface region while lower frequency waves will penetrate further into the cooler substrate. Figure 4-6(c) shows the normal displacement of the surface for this higher heating power density of 250 kW/cm^2. The excitation source characteristics are the same as those given above. In this case, the heating takes place much more rapidly and surface melting starts at about 305 μs. Such rapid heating leads to strong near-surface thermal gradients (shown in Figure 4-6(a) and (b)) which, in turn, lead to sharp changes in the mechanical properties within the wavelength range of the broadband surface acoustic wave. At heating times between $t = 0$ and $t = 300$ μs, a significant amount of surface acoustic wave dispersion is evident, with the higher frequency components that probe the near-surface temperature delayed with respect to the lower frequencies that penetrate further into the cooler bulk of the material.
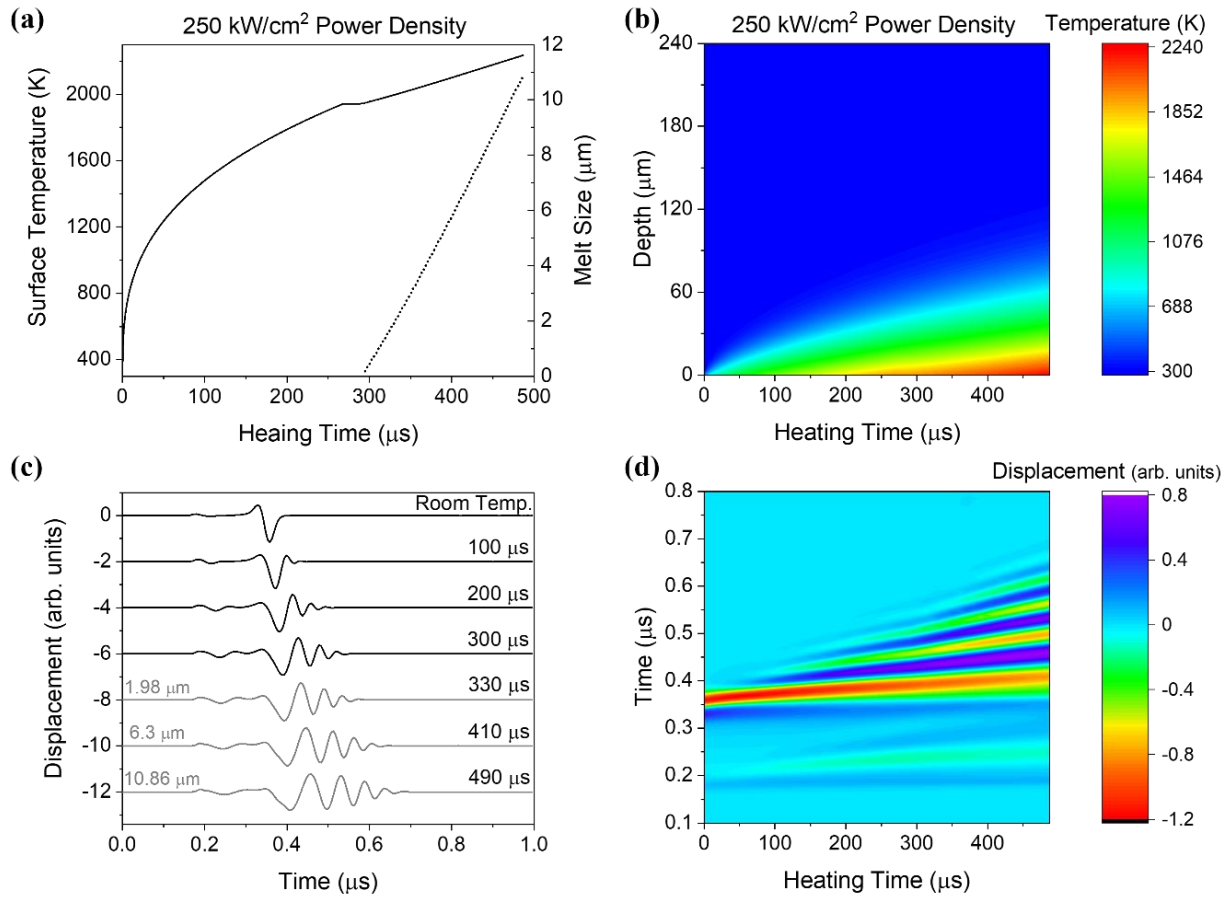
Figure 4-6. *(a)* Surface temperature (left axis) and melt size (right axis) as a function of heating time for a constant 250 kW/cm^2 power density incident on Ti-6Al-4V. *(b)* Calculated temperature field as a function of heating time and depth for this rapid heating case. *(c)* Calculated laser ultrasonic signals at room temperature and heating times of 100, 200, 300, 330, 410, and 490 μs. *(d)* Temporal evolution of the displacement field for the 250 kW/cm^2 power density.

This dispersive effect is further amplified at later times ($t > 300$ μs) where the higher frequency SAW components are also delayed by the presence of surface melt. Figure 4-6(d) shows the temporal evolution of the displacement field with surface heating. While the dispersion is certainly more pronounced than in the slow heating case of Figure 4-5(d), the onset of surface melting is not as evident. Note that the dispersion of the SAWs in a multilayer system can be used to back out the depth-dependent mechanical properties using a model-based inversion approach[12].

44

For the heating case, depth-dependent mechanical properties could ultimately be related to the subsurface temperature profile.

REFERENCES

1. Saunders, N., Guo, U. K. Z., Li, X., Miodownik, A. P. & Schillé, J.-Ph. Using JMatPro to model materials properties and behavior. *JOM* **55**, 60–65 (2003).

2. Ogi, H. *et al.* Titanium's high-temperature elastic constants through the hcp–bcc phase transformation. *Acta Materialia* **52**, 2075–2080 (2004).

3. Rose, J. L. *Ultrasonic waves in solid media*. (Cambridge University Press, 1999).

4. Cheng, A., Murray, T. W. & Achenbach, J. D. Simulation of laser-generated ultrasonic waves in layered plates. *The Journal of the Acoustical Society of America* **110**, 848–855 (2001).

5. Murray, T. W., Krishnaswamy, S. & Achenbach, J. D. Laser generation of ultrasound in films and coatings. *Appl. Phys. Lett.* **74**, 3561–3563 (1999).

6. Singh, R. K. & Narayan, J. A novel method for simulating laser-solid interactions in semiconductors and layered structures. *Materials Science and Engineering: B* **3**, 217–230 (1989).

7. Mills, K. C. *Recommended values of thermophysical properties for selected commercial alloys*. (Woodhead, 2002).

8. Casas, J., Kéita, N. M. & Steinemann, S. G. Sound Velocity in Liquid Titanium, Vanadium and Chromium. *Physics and Chemistry of Liquids* **14**, 155–158 (1984).

9. Bertoni, H. L. & Tamir, T. Unified theory of Rayleigh-angle phenomena for acoustic beams at liquid-solid interfaces. *Appl. Phys.* **2**, 157–172 (1973).

10. Biot, M. A. The interaction of Rayleigh and Stoneley waves in the ocean bottom*. *Bulletin of the Seismological Society of America* **42**, 81–93 (1952).

11. Meegan, G. D., Hamilton, M. F., Il'inskii, Yu. A. & Zabolotskaya, E. A. Nonlinear Stoneley and Scholte waves. *The Journal of the Acoustical Society of America* **106**, 1712–1723 (1999).

12. Murray, T. W., Balogun, O., Steen, T. L., Basu, S. N. & Sarin, V. K. Inspection of compositionally graded mullite coatings using laser based ultrasonics. *International Journal of Refractory Metals and Hard Materials* **23**, 322–329 (2005).

CHAPTER 5. REAL-TIME INSPECTION OF LASER HEATING AND MELTING

5.1 High Sensitivity Laser Ultrasonic Experimental Setup

A laser ultrasonic system was designed to study surface acoustic wave propagation through a laser-heated region of Ti-6Al-4V samples. A schematic of this experimental setup is shown in Figure 5-1. A pulsed Nd:YAG laser operating at the fundamental frequency ($\lambda = 1064$ nm) and a repetition rate of 15 Hz is used to generate broadband surface acoustic waves. The generation laser is collimated and focused to a line on the sample surface using a cylindrical lens. A line source produces a negative-going monopolar Rayleigh wave displacement instead of the bipolar displacement that results from a circular source[1]. We focus the generation laser beam into a line, rather than a circular spot, to improve the signal-to-noise ratio in our experiments since more energy can be injected into the sample while keeping the energy density low enough to avoid ablation. Furthermore, the generated surface acoustic waves have plane wavefronts parallel to the line source, which is advantageous for surface flaw inspection[2,3]. At the sample surface, the line source was approximately 15 mm in length and had a Gaussian FWHM of 60 μm. The laser energy at the sample was 1.6 mJ, sufficiently low that generation remained in the thermoelastic regime.

The displacement normal to the surface associated with the laser-generated acoustic wave was detected using a photorefractive crystal (PRC) based interferometer using a Bismuth Silicon Oxide (BSO) PRC[4-6]. The detection laser was a 300 mW frequency doubled Nd:YAG laser operating at 532 nm. The surface displacements are detected with a photodetector, sent to a digital oscilloscope with a 200 MHz bandwidth limit, and subsequently transferred to a computer and filtered using a 40 MHz second order low pass Butterworth filter. The distance between the SAW excitation line and detection point was set to 4.0 mm.
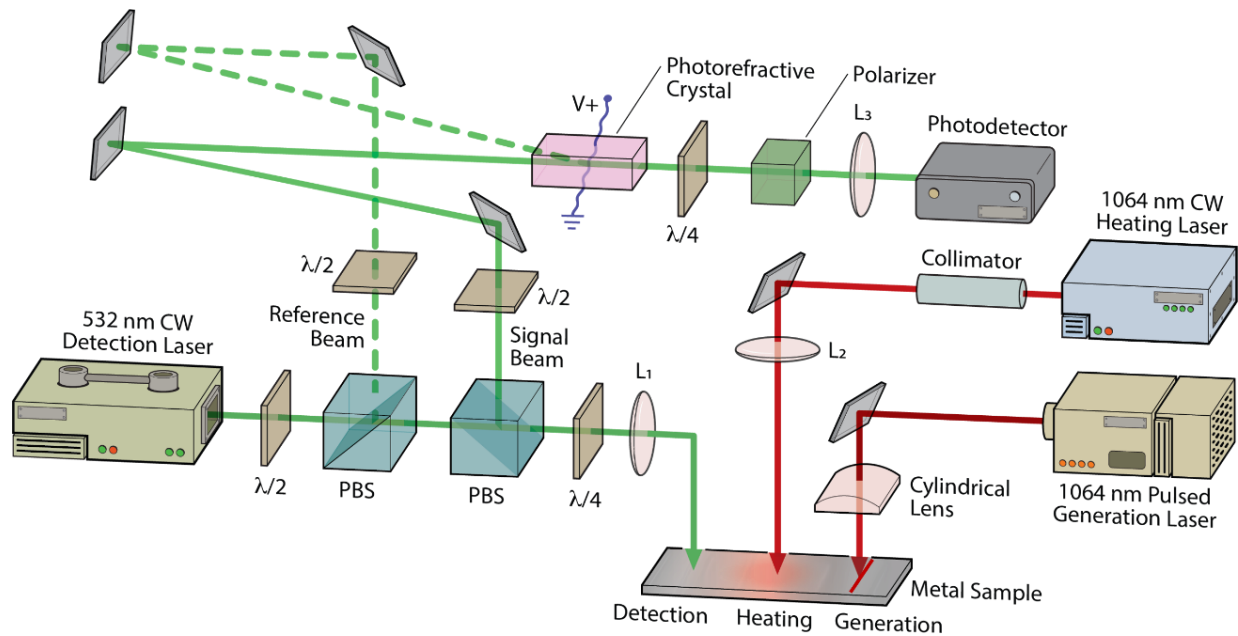
Figure 5-1. Schematic of the experimental setup depicting the three laser beams on the sample surface. The following abbreviations are used: PBS – polarizing beam splitter, λ/2 – half-wave plate, λ/4 – quarter-wave plate, L1, L2, L3 – focusing lenses.

5.2 Optical Detection of Ultrasound

Optical interferometry is a highly sensitive technique to measure ultrasonic displacement[46]. There are several types of interferometers used for the detection of ultrasonic movement of surfaces. In a Michelson interferometer, light is reflected from a mirror-like surface and interferes with a reference beam to measure optical phase and instantaneous surface displacement[46]. The interference is set at quadrature, meaning the reference and signal beams are out of phase with each other, to obtain optimal sensitivity. However, when a sample has a rough surface, the light reflected has a speckle pattern, and the light scattered from different paths of the surface is not phase related and does not constructively interfere[46].

Photorefractive crystal (PRC) based interferometry is well suited for detection on optically rough surfaces and has been widely used in the optical detection of ultrasound[4-6]. The PRC has an

47

index of refraction that varies according to the spatial distribution of light incident upon it, and it exhibits both photoconductive and electro-optic behavior[8-10]. This technique actively adapts the reference wavefront to match the speckled signal wavefront for optimal interference. The PRC-based interferometer begins with the detection laser output directed to a beamsplitter where it is divided into reference and signal beams. The reference beam is sent directly to the PRC, while the signal beam is focused onto the polished specimen surface, and, upon reflection, is sent to the PRC where it interferes with the reference beam at a 5-degree angle and creates a sinusoidal index grating inside the crystal. A portion of the reference beam diffracts from the grating in the two-wave mixing process and interferes with the signal beam at the photodetector. In addition, we apply an AC electric field across the PRC to enhance the two-wave mixing gain. Polarization optics after the PRC were used to ensure that the diffracted reference beam and transmitted signal beam were in quadrature, optimizing the detection sensitivity.

5.3 Experimental Procedure

A fiber-coupled 60 W continuous wave Nd:YAG laser operating at a wavelength of 1064 nm was used to heat the sample surface. The laser output was collimated and sent through a spherical lens to the surface. The Gaussian spot size at the surface was 644 μm and the heating laser was positioned directly in between the SAW excitation laser line and the detection point using translation stages. The samples were polished Ti-6Al-4V disks with a diameter of 25 mm and a height of 13 mm. A LabVIEW code was used to control the heating laser power and to acquire laser ultrasonic signals during the heating process at a data acquisition rate of 15 Hz (corresponding to the excitation laser repetition rate). At a given heating laser power, data acquisition commenced at a heating time t_h = -3 s, and single shot laser ultrasonic signals were acquired continuously throughout the experiment. At t_h = 0 s the heating laser was switched on

and the sample was illuminated with a constant power for 10 s, after which the heating laser was turned off. To monitor sample cooling, data acquisition continued for 5 s after the heating laser was turned off. The sample was then allowed to cool to room temperature and translated to a new position. A schematic of this experimental procedure is displayed in Figure 5-2. The experimental procedure was repeated a total of 10 times at each heating power and the laser ultrasonic signals collected at each time, with respect to heating laser turn on at $t_h = 0$, were averaged to improve the signal-to-noise ratio. After each experiment, the sample surface was inspected using an optical microscope for signs of surface melting and discoloration.
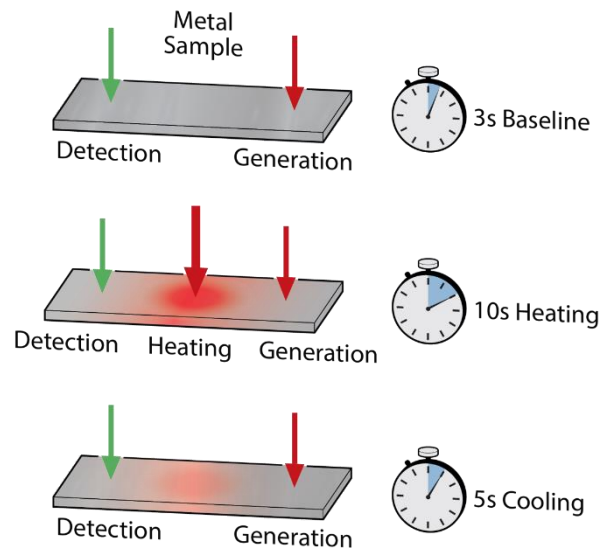
Figure 5-2. Schematic of the experimental procedure followed to monitor real-time transient heating and melting.

5.4 Real-Time Inspection of Transient Heating and Melting

The first experiment was conducted at a CW laser heating power of 30 W. Figure 5-3(a) shows the ultrasonic signals detected at several heating times, with the prominent feature (negative dip) corresponding to the arrival of the surface acoustic wave. The top waveform shows the response in the absence of surface heating ($t_h < 0$) and the negative peak in the surface wave arrival

is seen at about 1.33 μs. The next four curves show the displacement responses at various times after the heating laser is turned on, and the last two curves show the response at 1 and 3 s after the heating laser is turned off. The shape of the surface acoustic wave remains relatively constant, but the arrival is delayed as heating proceeds. This lack of dispersion is expected as the heating times are long and the thermal field is thus relatively constant throughout the surface wave penetration depth. Figure 5-3(b) shows similar results for a CW laser heating power of 46 W. The basic features of the waveforms at 30 W and 46 W are similar but the delay in the SAW is more pronounced with the larger heating power due to the increase in temperature in the laser-heated region.

Figure 5-3(c) and (d) show the evolution of the displacement field throughout these experiments for CW laser heating powers of 30 W and 46 W, respectively. The abscissa gives the experiment time, where $t_h = 0$ represents the time at which the heating laser is turned on and the heating laser is turned off at $t_h = 10$ s, while the ordinate gives the time after the excitation laser pulse. The color bar represents the out of plane displacement of the surface. In these images, the SAW arrival has the negative-most amplitude shown in red. In both images, the surface wave arrival shows a marked delay associated with the onset of surface heating. This is followed by a more gradual change between $t_h = 2$ s and $t_h = 10$ s as heat diffuses through the sample and the sample temperature begins to approach the steady state. Finally, a rapid decrease in the arrival time is observed when the heating laser is turned off. Interestingly, the 46 W heating power not only causes more of a surface wave delay but the shape of the arrival over heating time is quite different than the 30 W heating laser case, and there is not a simple linear scaling between them. Furthermore, optical microscopy revealed no visible markings left on the surface from the 30 W

heating power experiments, while there were clear discolorations and surface texture changes, indicative of surface melting, resulting from the 46 W heating power experiments.
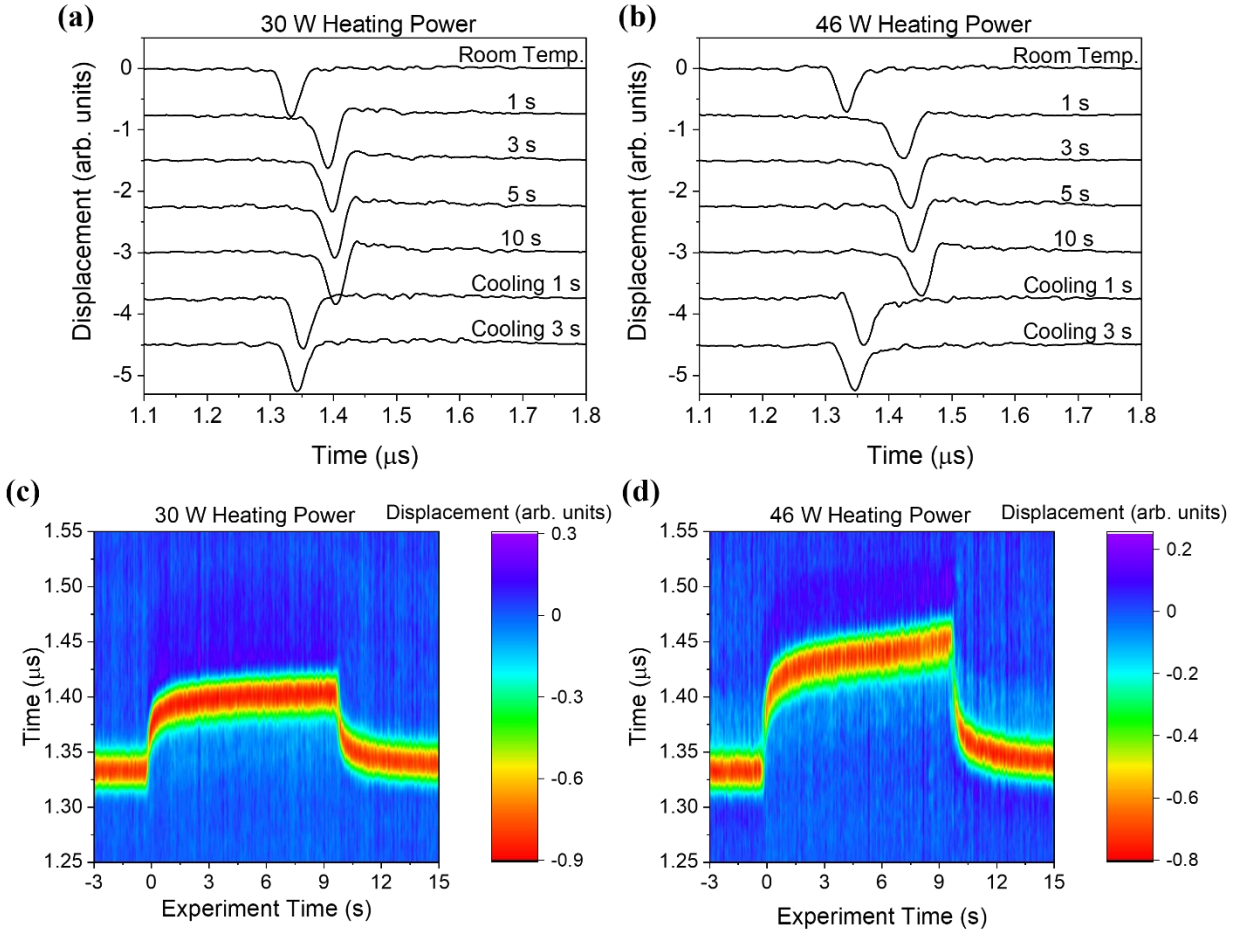
Figure 5-3. Laser ultrasonic signals in Ti-6Al-4V samples with a source to detector distance of 4.0 mm at room temperature, heating times of 1, 3, 5, and 10 s, and cooling times of 1 and 3 s for CW laser heating powers of *(a)* 30 W and *(b)* 46 W. Temporal evolution of the displacement fields, where experiment time and time of 0 s indicates the time at which the heating laser is turned on, for CW laser heating powers of *(c)* 30 W and *(d)* 46 W.

The frequency content of the surface acoustic waves generated in these experiments extends to 32 MHz. At this frequency and with the slow heating time of 10 s, the SAW is minimally dispersive with the increasing temperatures as seen in Figure 5-3, while the delay of the SAW is sensitive to the heating power or surface state. The arrival time of the negative peak of the surface

wave was determined as a function of heating time for different laser powers. The surface wave delay was then determined by subtracting the room temperature arrival time. Figure 5-4(a) shows the real-time transient surface wave delays for heating powers of 30, 34, and 40 W. Note that at these lower heating powers, all the curves show a similar shape. If these curves are divided by the heating laser power to determine the normalized surface wave delay (in units of ns/W), all the curves collapse to a single curve as shown in Figure 5-4(b). This indicates that in this regime, the surface wave delay is a simple linear function of the heating power. Optical microscopy confirmed that there were no visible changes to the surface subsequent to heating in this power range.

At higher heating powers the response is quite different, however: experiments performed at 46, 48, and 56 W resulted in visible markings and surface texture changes. The delay curves for these heating powers are plotted in Figure 5-4(c) together with the results from the 30 W experiment during which no surface changes were observed. The SAW delay is significantly more pronounced and the normalized surface wave delay plots in Figure 5-4(d) show a distinct change in shape. While all the curves follow the 30 W heating curve for early heating times, deviations begin at later times, with the deviations occurring earlier for higher power. It is hypothesized that the nonlinearity in the curve is associated with phase change and the presence of surface melt.
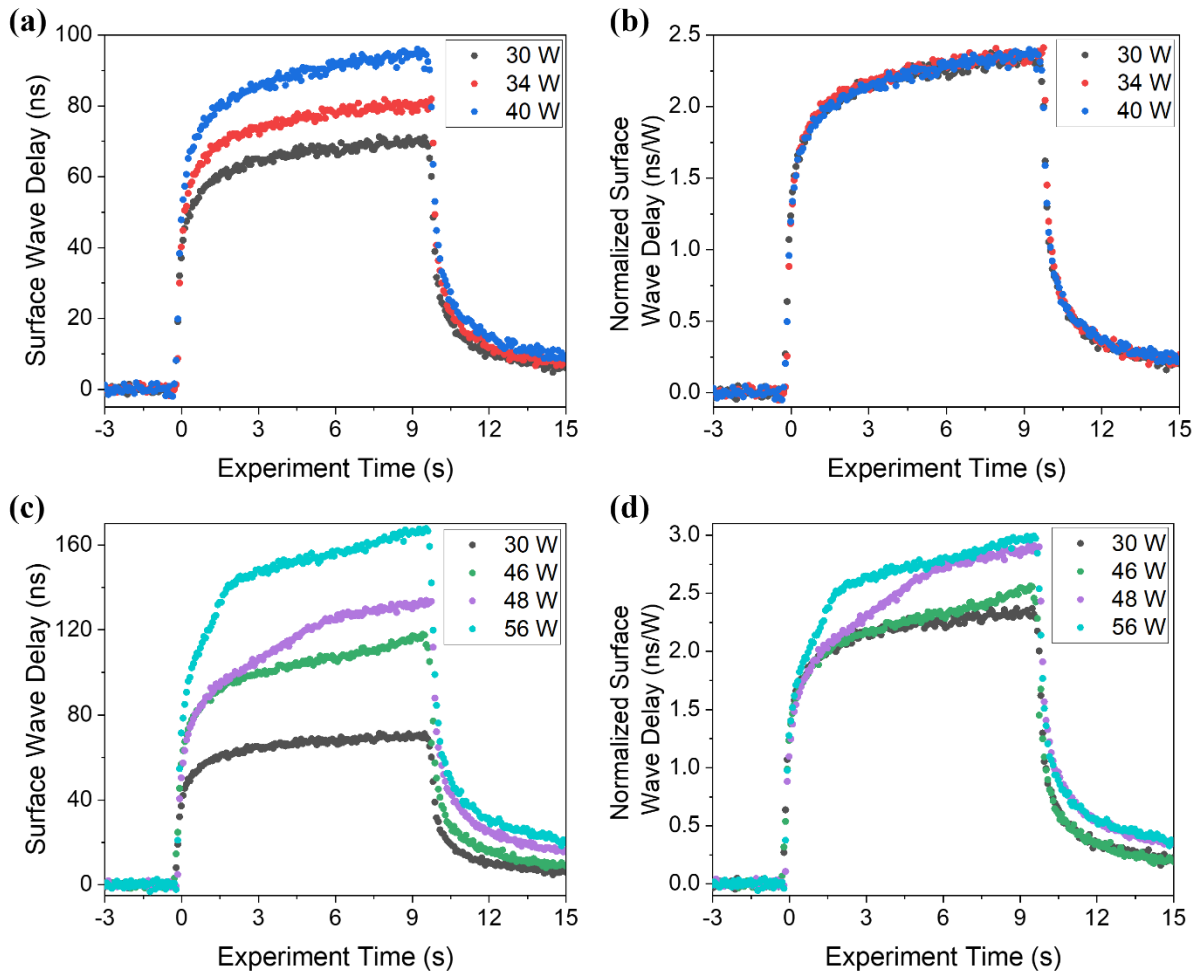
Figure 5-4. Single shot experimental data of the delay from room temperature of the SAW as a function of experiment time where experiment time of 0 s indicates the start of heating. ***(a)*** Heating laser powers of 30, 34, and 40 W and ***(b)*** these SAW time of arrival curves normalized by their respective heating powers. ***(c)*** Heating laser powers of 30, 46, 48, and 56 W and ***(d)*** these curves normalized by their respective heating powers.

5.5 Incremental Heating Experiments

Incremental heating experiments were performed in which the laser power was fixed at 48 W but the illumination time was varied between 0.5 s and 10.0 s in 0.5 s intervals. The sample surface was optically observed after each interval, and the sample was translated between measurements such that a new region was illuminated. Figure 5-5(a) shows a subset of the surface wave delay data, again demonstrating that surface waves can be very effective for the

characterization of the transient thermal field. Figure 5-5(b) shows a zoom-in of the first 5.0 s of normalized surface wave delay for heating laser powers of 30 W and 48 W. The curves are nearly identical up until about 2.0 s of illumination, after which the 48 W curve shows a significantly higher delay. Optical micrographs of the surface are shown in Figure 5-5(c). There is no detectable surface discoloration before 2.0 s of heating. However, there is a clear indication of a melt region starting at 2.0 s and this region continues to grow at longer heating times.

Note that in the modeling results presented in Chapter 4, a one-dimensional illumination model was used to elucidate the effects of surface heating and melting on surface wave propagation. Thus a quantitative comparison with experimental results, in which the waves propagate through a region heated with a Gaussian laser source, is not possible. Nevertheless, there is qualitative agreement between the two with a rapid delay in the surface wave velocity at the onset of illumination and further decrease in surface wave velocity associated with melting. The surface acoustic wave delay curves, such as those shown in Figure 5-4 and Figure 5-5, may prove useful in monitoring laser-induced thermal processes, particularly in more complex cases involving phase transformation. Changes in these curves indicate variations in the heating laser parameters or laser-material interaction. These experimental results are limited to relatively slow heating, where the temperature is uniform over the surface wave penetration depth. A higher repetition rate pulsed laser can be used to probe more rapid thermal processes and potentially obtain quantitative information about the heated zone, including temperature distribution and melt pool depth. It is also important to point out that laser additive manufacturing techniques are conducted in a layer-wise manner, and track formation and overlap add complexity to the heating and melting processes.

(a) 48 W Heating Power

(b)

(c) 2.0 s 2.5 s 3.0 s 3.5 s 4.0 s
4.5 s 5.0 s 5.5 s 6.0 s 6.5 s
500 μm
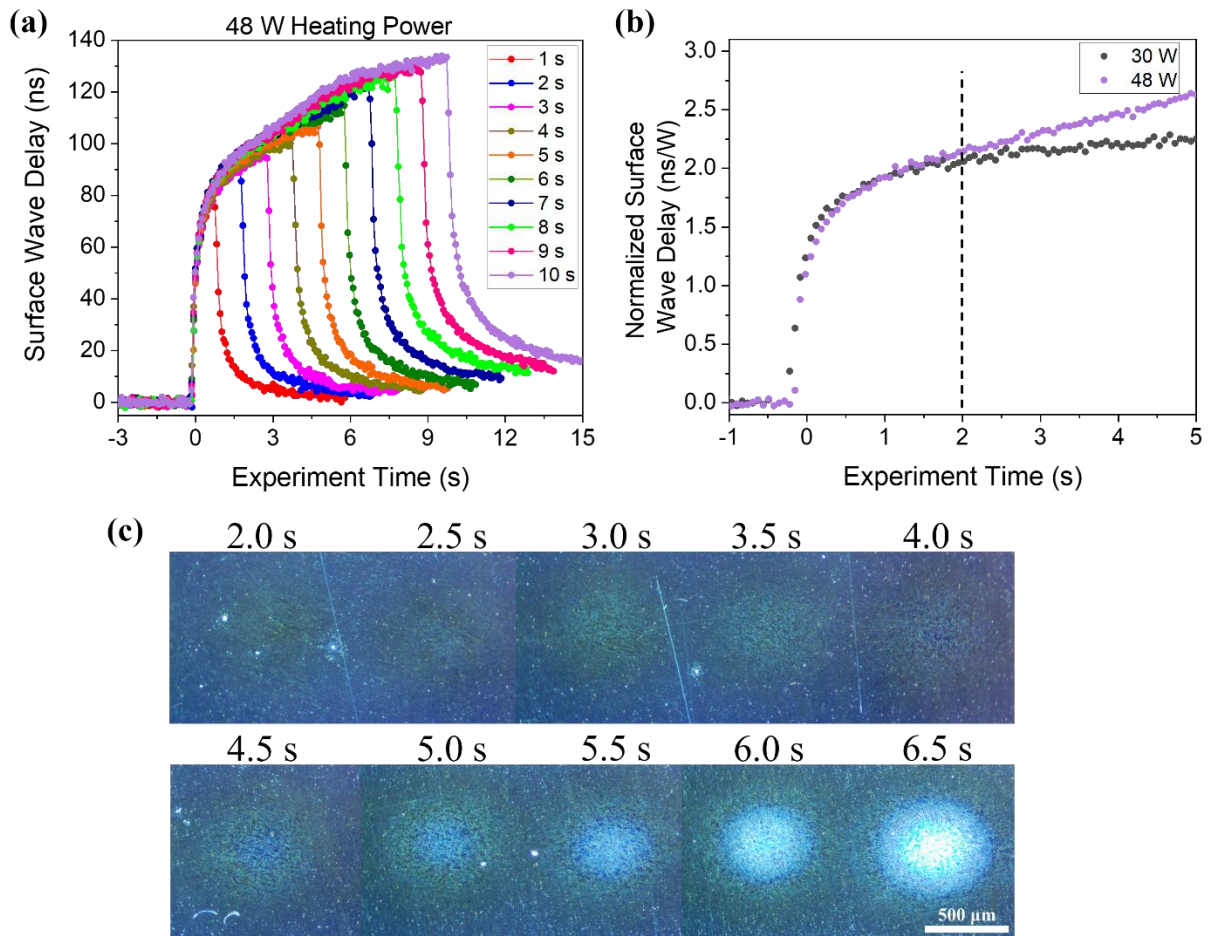
Figure 5-5. (a) Subset of surface wave delay data from the incremental heating experiment at a fixed laser power of 48 W. *(b)* Zoom-in of the normalized surface wave delay for heating laser powers of 30 W and 48 W. *(c)* Optical micrographs of the sample surface after the indicated times of heating.

REFERENCES

1. Doyle, P. A. & Scala, C. M. Near-field ultrasonic Rayleigh waves from a laser line source. *Ultrasonics* **34**, 1–8 (1996).

2. Arias, I. & Achenbach, J. D. Thermoelastic generation of ultrasound by line-focused laser irradiation. *International Journal of Solids and Structures* **40**, 6917–6935 (2003).

3. Achenbach, J. D. The Thermoelasticity of Laser-Based Ultrasonics. *Journal of Thermal Stresses* **28**, 713–727 (2005).

4. Ing, R. K. & Monchalin, J. -P. Broadband optical detection of ultrasound by two-wave mixing in a photorefractive crystal. *Appl. Phys. Lett.* **59**, 3233–3235 (1991).

5. Blouin, A. & Monchalin, J. Detection of ultrasonic motion of a scattering surface by two-wave mixing in a photorefractive GaAs crystal. *Appl. Phys. Lett.* **65**, 932–934 (1994).

6. Delaye, P. *et al.* Detection of ultrasonic motion of a scattering surface by photorefractive InP:Fe under an applied dc field. *J. Opt. Soc. Am. B* **14**, 1723 (1997).

7. Scruby, C. B. & Drain, L. E. *Laser Ultrasonics: Techniques and Applications*. (Routledge, 2019). doi:10.1201/9780203749098.

8. Saleh, B. E. A. & Teich, M. C. *Fundamentals of photonics*. (Wiley, 2019).

9. Solymar, L., Webb, D. J. & Grunnet-Jepsen, A. *The physics and applications of photorefractive materials*. (Clarendon Press ; Oxford University Press, 1996).

10. Gunter, P. & Huignard, J. P. *Photorefractive Materials and Their Applications I*. vol. 61 (Springer Berlin Heidelberg, 1988).

CHAPTER 6. PROBING TRANSIENT DEPTH-DEPENDENT TEMPERATURE FIELDS AND MELTS

In this chapter we develop three-dimensional finite element acoustic models to study rapid, depth-varying laser heating. We also present a fast acquisition experimental setup built to probe transient depth-dependent temperature fields and at sufficiently high powers, melt pool depths. The work in this chapter is currently in preparation to be submitted for publication in *Applied Physics Letters.*

6.1 3-D Time Domain Finite Element Simulations

We developed a 3-D model for time domain finite element analysis (FEA) simulations to study surface acoustic wave interaction with rapid, depth-varying temperature fields. We begin by analytically calculating the 3D thermal field produced from a Gaussian beam absorbed at the surface of a semi-infinite solid with the following equation[1].

$$T_{Gauss}(r, z, t) = \frac{F_0 d^2}{K} \sqrt{\frac{\kappa}{\pi}} \int_0^t \frac{p(t - t')}{\sqrt{t'}\,(4\kappa t' + d^2)} \exp\left[-\frac{z^2}{4\kappa t'} - \frac{r^2}{4\kappa t' + d^2} \right] dt' \quad [1]$$

We calculate the temperature rise from room temperature, T, as a function of depth z, radius r, and time t. F_0 is the maximum power density, d is the heating laser 1/e beam radius, κ is the thermal diffusivity, and K is the thermal conductivity. The power density F_0 is a function of beam radius and is calculated with $F_0 = P_0 A / \pi d^2$ where P_0 is the heating laser maximum power and A is the material absorption coefficient at 1064 nm, which is the wavelength of the heating laser we use in our experiments. The values used for these calculations are listed below.

Table IV. Thermal and optical properties of Ti-6Al-4V used in 3-D FEA modeling.

Absorption at λ=1064 nm, A	0.3850
Melting temperature, T_m	1943 K
Density, ρ	4.42 g/cm^3
Thermal conductivity at room temperature, K	7 W/m K
Thermal Diffusivity, κ	2.803E-6 m^2/s

The laser pulse shape is defined as *p(t)* in Equation 1. In this chapter we are interested in capturing rapid laser heating and melting, and as such, we chose a laser pulse in the shape of a sigmoid function to increase the amount of time during which the heating begins. The sigmoid function used is the inverse of a Gaussian function and defined below

$$p(t) = \frac{P_0}{2}\left(1 + \text{erf}\left(\frac{1.8(t - t_0)}{\tau}\right)\right) \qquad [2]$$

where P_0 is the maximum power, t_0 is the time at the center of the pulse, and τ is the rise time of the pulse shape from 10% to 90% of P_0. We choose a 500 ms pulse shape with $t_0 = 250$ ms, a maximum power $P_0 = 5$ W, and a rise time $\tau = 225$ ms, as displayed in Figure 6-1(a). This pulse shape is included in the 3-D temperature calculations, Equation 1, with $t = 500$ ms and a Gaussian beam radius of $d = 185$ µm for a 0.5 mm^3 cubic area. Figure 6-1(b) shows the 3D temperature field calculated with these parameters.
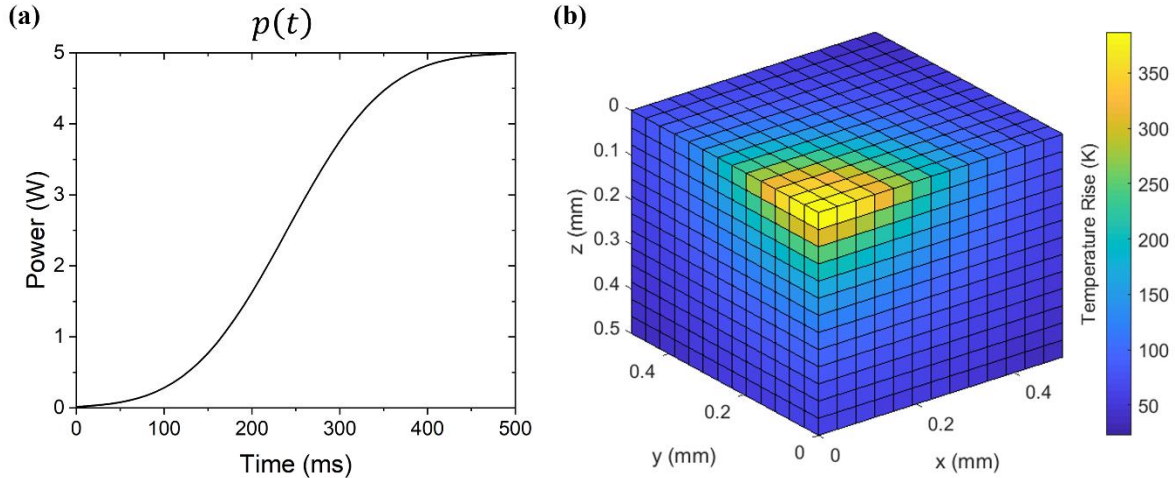
Figure 6-1. *(a)* Heating laser pulse shape as a function of time, *p(t)*, for a 500 ms pulse and a maximum power of 5 W. *(b)* Calculated 3-D temperature field resulting from this laser pulse and a 185 μm Gaussian beam radius in a 0.5 mm^3 cubic area of Ti-6Al-4V.

Next, we import the calculated 3-D temperature field into *Onscale* (previously known as *PZFlex*), a time domain finite element software, where we calculate the temperature-dependent mechanical properties of density $\rho(T)$, elastic modulus $E(T)$, and Poisson's ratio $\sigma(T)$ and the resulting bulk wave speeds of the longitudinal, $c_L(T)$, and shear, $c_T(T)$, waves as was done previously in Chapter 4. The temperature-dependent bulk wave velocities and densities are then assigned to their corresponding spatial position in the center of the 3-D model. As shown in Figure 6-1(b), the temperature field we calculate is a quarter of the full field, so we mirror the temperature-dependent geometry across *x*. The rest of the geometry is given room temperature Ti-6Al-4V properties. We employ a symmetry boundary condition across *y* in the FEA model to save computation power. Figure 6-2(a) shows the geometry of the FEA model including this symmetry boundary condition. Appendix II includes the *Onscale* code used to run this model.

In these 3-D simulations, we use an excitation line source as is used in experimentation. The excitation laser spot size was set to 15 μm full width at half maximum (FWHM) with a 1.5 ns

thermoelastic temporal pulse. The detection location is set to 600 μm away from the excitation line

source. The box size in the simulations is set to 1 μm and our full geometry is discretized into 1000

X 850 X 1000 elements in *x*, *y* and *z*, respectively. This box size is chosen so that the generation

laser spot size (15 μm) is defined by at least 15 nodes.

(a)   **(b)**
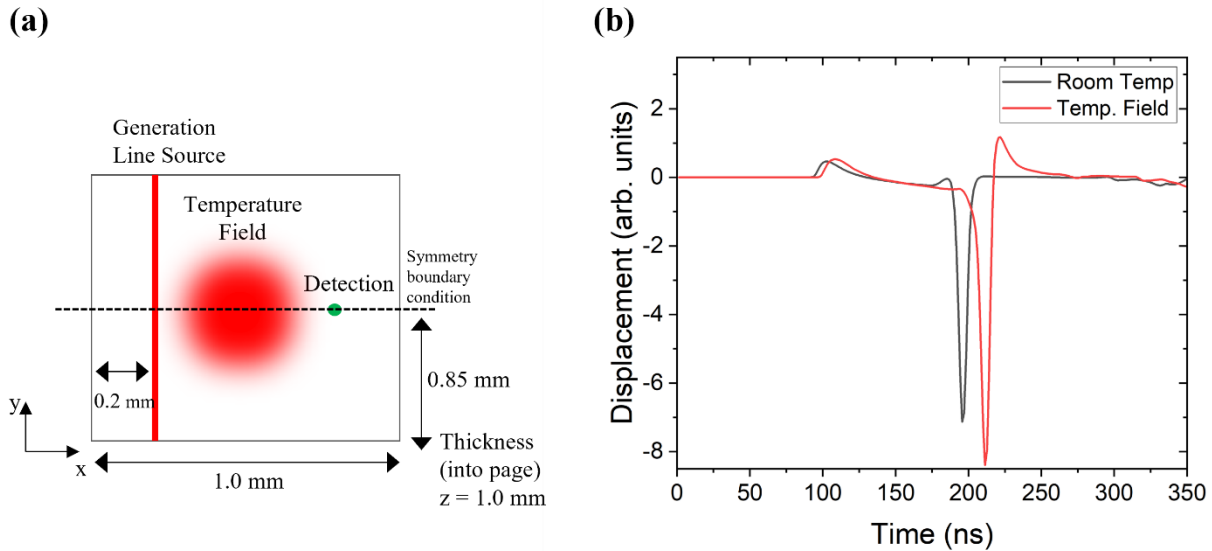
Figure 6-2. (a) Geometry of the 3-D FEA model used to simulate SAW propagation through a laser-heated region. *(b)* Simulation results of displacement normal to the surface as function of time with a source to detector distance of 600 μm at room temperature and for the laser-heated region from the 3-D thermal field.

The normal surface displacement as a function of time is given in Figure 6-2(b) for the 3-

D model at room temperature, or in the absence of heating, and for the laser-heated model with

the thermal field calculated above from a *t* = 500 ms heating pulse with a max power of 5 W. In

the response for the model at room temperature, a small amplitude wave arrival corresponding to

the surface skimming longitudinal wave is seen at about 100 ns followed by the larger SAW

amplitude arrival at about 195 ns. In the laser-heated model response, both the surface skimming

longitudinal wave and the surface acoustic wave are delayed. Significant SAW dispersion is

evident in this response as the higher frequency, short wavelength, components that probe the near-

surface temperatures are delayed with respect to the lower frequencies that penetrate further into the cooler bulk of the material.

Instead of detecting in-line with the laser-heated zone, as in Figure 6-2(a), we can detect at multiple locations spanning this entire region, see Figure 6-3(a), to create displacement fields. These displacement fields show the SAW delay and dispersion resulting from the laser-heated region and can provide additional information on the spatial extent of the heated and melted regions when used with melting simulations.
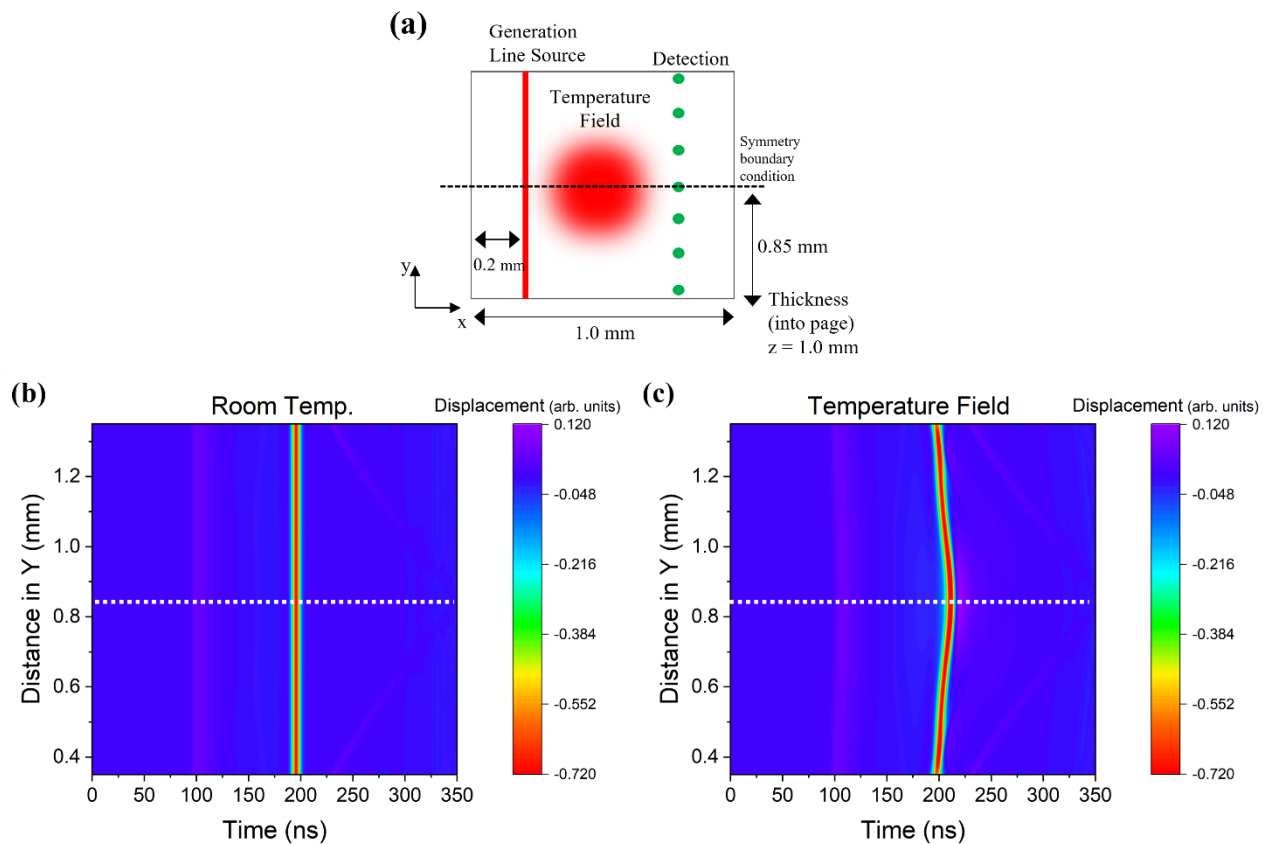
Figure 6-3. (a) Schematic showing detection at multiple locations across the laser-heated zone. Displacement fields at a source to detector distance of 600 μm in *(b)* the absence of thermal effects and *(c)* from a laser-heated area. The temperature field is centered at y = 0.85 mm and is represented by the dashed line.

6.2 Fast Acquisition Laser Ultrasonic Experimental Setup

A new laser ultrasonic system was developed to study surface acoustic wave propagation through a rapid, transient laser-heated region of Ti-6Al-4V. A schematic of this configuration is shown in Figure 6-4. A short pulse microchip laser operating at 532 nm and a repetition rate of 1 kHz is used to generate the broadband surface acoustic waves. It is important to note that our previous experimental setup used a 15 Hz repetition rate laser, so we are now working with an acquisitions system that is about 67 times faster. The laser pulse is sent through a variable attenuator and reflected from a gimbal mirror to finely control its position. We focus the generation laser through a cylindrical lens and a long working distance 5X microscope objective to form a line source with a Gaussian FWHM of 15 μm.
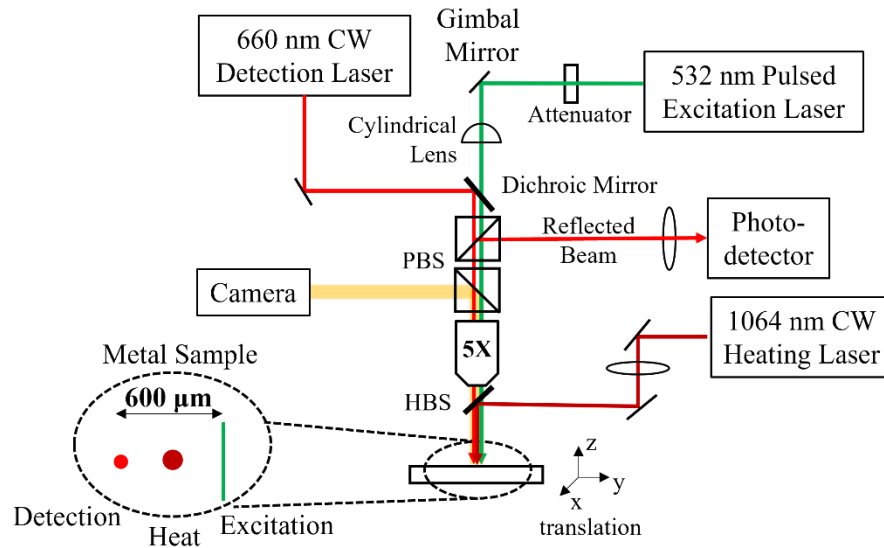
Figure 6-4. Schematic of the experimental setup depicting the three laser beams on the sample surface. The following abbreviations are used: PBS – polarizing beam splitter, HBS – harmonic beam splitter.

The detection laser is a continuous wave detection laser operating at 660 nm. The detection beam is sent through the same 5X microscope objective as the generation laser. The displacement

normal to the surface is detected using a Michelson interferometer. The same IPG Photonics fiber-coupled 60 W continuous wave Nd:YAG laser operating at 1064 nm as in our previous experimental setup is used to heat the samples in this setup. The Gaussian 1/e spot size at the surface was 185 μm and was positioned directly in between the excitation laser line and the detection point using translation stages. We use the IPG Photonics Pulse Shaper Software to set the heating pulse to the 500 ms pulse shape $p(t)$ defined by Equation 2 and the same parameters as those plotted in Figure 6-1(a), but with varying max powers P_0. We include a glass slide in the heating laser beam path to direct some light onto a power meter with which we measure the max power reached for every experiment. This experimental setup includes a charge coupled device (CCD) camera that allows us to observe the sample surfaces immediately after heating. We heat polished Ti-6Al-4V disks of a 25 mm diameter and a height of 13mm.

Figure 6-5 shows an ultrasonic signal recorded on Ti-6Al-4V at room temperature with a source to detector distance of 600 μm. This signal was averaged 10,000 times and is not post-processed. In this figure we also plot a simulation result at the same source to detector distance, and we normalize both responses with respect to the peak amplitude of the SAW. The small amplitude wave arrival at about 100 ns corresponds to the surface skimming longitudinal wave while the larger SAW amplitude arrival occurs at 195 ns. As is shown, our simulation results agree well with what we achieve experimentally besides the scattering seen in the experimental results as Ti-6Al-4V is known to be a highly scattering material.
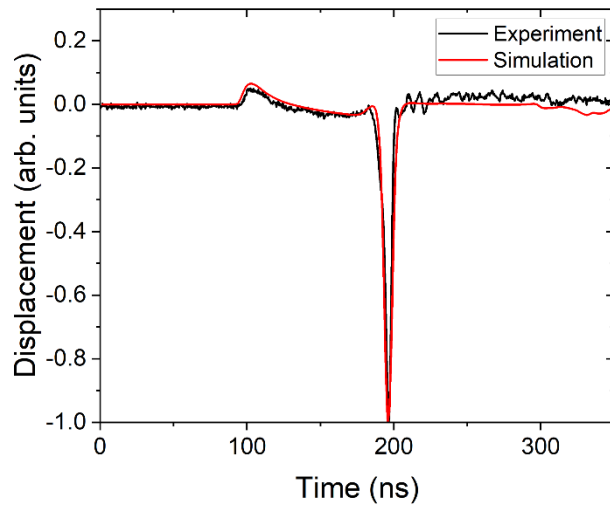
Figure 6-5. Comparison of experimental and simulation results on room temperature Ti-6Al-4V at a source to detector distance of 600 μm.

6.3 Probing Transient Depth-Varying Temperature Fields and Melts

The first set of experiments were conducted in a similar manner as before where single shot laser ultrasonic signals were acquired continuously during the laser-heating processes at a data acquisition rate of 1 kHz. At a given laser power, data acquisition began at experiment time *t* = 0 with the sample at room temperature, the 500 ms heating laser pulse (shown in Figure 6-1(a)) is then turned on at experiment time of *t* = 300 ms, and data acquisition continues until experiment time of *t* = 1250 ms to monitor the sample cooling. Single experiments (without averaging) are presented here. All the data was post-processed with a 100 MHz second order lowpass filter.

Figure 6-6(a) shows the real-time transient surface wave delays for heating power of 13, 18, 23, and 26 W which are determined by subtracting the room temperature arrival times from the arrival of the negative peak of the SAW. The 13 and 18 W heating powers did not result in melting as was inspected by the CCD camera. Figure 6-6(b) shows how both of these normalized delayed curves (delay divided by heating laser power) fall directly on top of each other indicating

that there were no phase changes, and the surface wave delay is linearly related to the heating power. At the higher heating powers of 23 and 26 W, the shape of the delay curves changes and visible surface texture changes were observed with the CCD camera. These normalized curves shown in Figure 6-6(c) and (d) show the distinct change in shape happening at an experiment time of $t = 700$ ms for the 23 W experiment and earlier at $t = 665$ ms for the higher 26 W heating power. These delay curves show the same features as seen in our slow heating experiments – the SAW is increasingly delayed with increasing heating power, or temperatures, and the delay becomes nonlinear when melting is achieved. It is important to note that these heating curves show a heating pulse closer to 400 ms, approximately between $t = 400$ ms and $t = 800$ ms, instead of the 500 ms pulse shown in Figure 6-1(a). This is because the heating laser we use does not begin to emit until about 0.5 W, which corresponds to approximately 100 ms on the $p(t)$ curve.
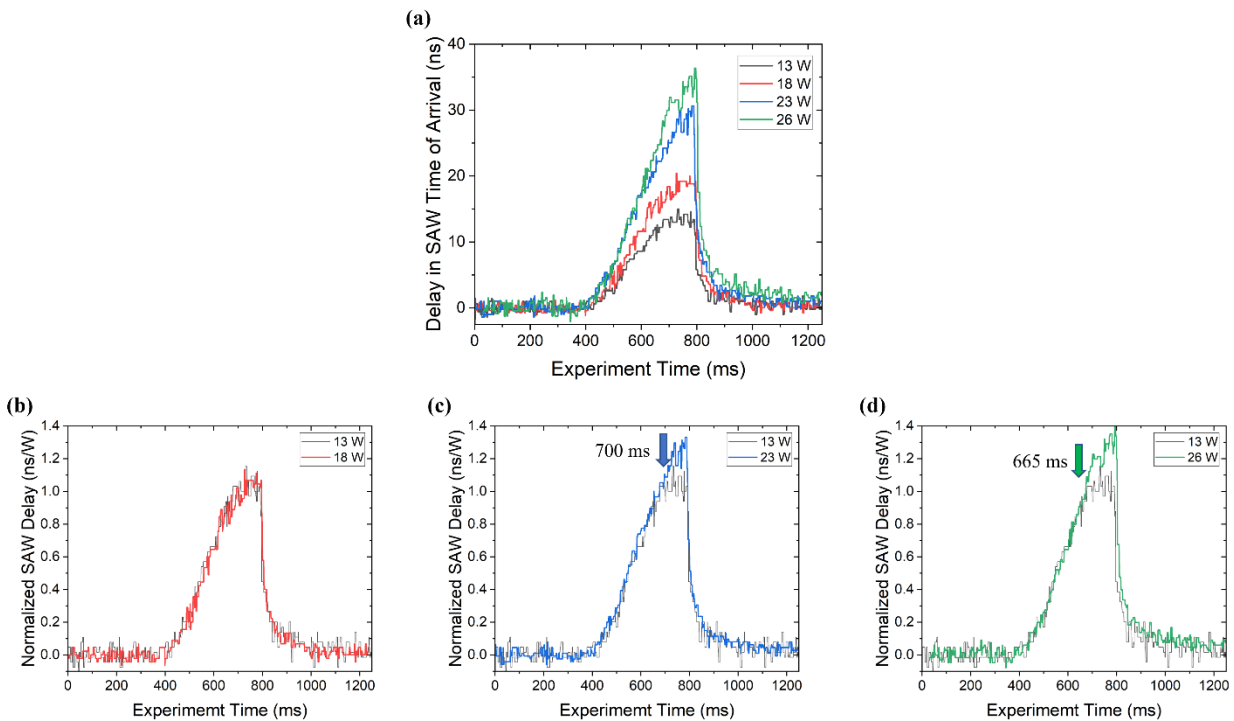
Figure 6-6. *(a)* Real-time transient surface wave delays for heating laser powers of 13, 18, 23 and 26W. Normalized surface wave delays, in units of ns/W, for heating powers of *(b)* 13 and 18 W, *(c)* 13 and 23 W, and *(d)* 13 and 26 W.

65

What becomes more interesting about these rapid heating experiments, however, is that the temperature fields induced here are depth-varying, unlike in the slow heating case where the temperatures were relatively uniform in the near-surface region. As such, it is expected that these thermal gradients will result in the surface acoustic waves to become dispersive as the higher frequency components that probe the near-surface temperatures will become delayed with respect to the lower frequencies that penetrate further into the cooler bulk of the material. This dispersion results in a SAW shape change as seen in our simulation results in Figure 6-2 and 6-3. Our one-dimensional illumination model results presented in Chapter 4 demonstrate that the SAW is expected to become even further dispersive by the presence of melt during these rapid heating cases.

Figure 6-7(a) and (b) show displacement fields for the 13 W and 26 W experiments. As seen in the 26 W field, it is evident that the SAW changes in shape during the laser illumination times roughly between $t = 400$-800 ms. It is less evident how dispersive the purely heating case of 13 W is from the displacement fields. However, the surface acoustic waves in Figure 6-7(c) and (d) show the change in shape of the SAW more clearly. Recall that this data is not averaged and each of these results is from a single experiment. As such, we choose to show an average of 25 single shots for the ultrasonic signals. The first response (plotted in black) is averaged between $t = 100$ and 125 ms, and shows the response in the absence of heating, the next response (plotted in red) is averaged between $t = 555$ and 580 ms, which is about 155 ms after heating began, and the last response (plotted in blue) is averaged between $t = 755$ and 780 ms, which is at the peak of the heating time and a few ms before the heating laser is powered off. In these ultrasonic signals, the prominent feature with the negative-most amplitude corresponds to the surface acoustic wave arrival. These figures show how the surface acoustic wave is not only delayed by the heating, but

it also changes in shape with this effect being more drastic for the 26 W case in which melting resulted. The dispersion in both of these cases would become much more evident with averaging experiments conducted at the same heating power. As such, in the next set of experiments performed we used averaging.
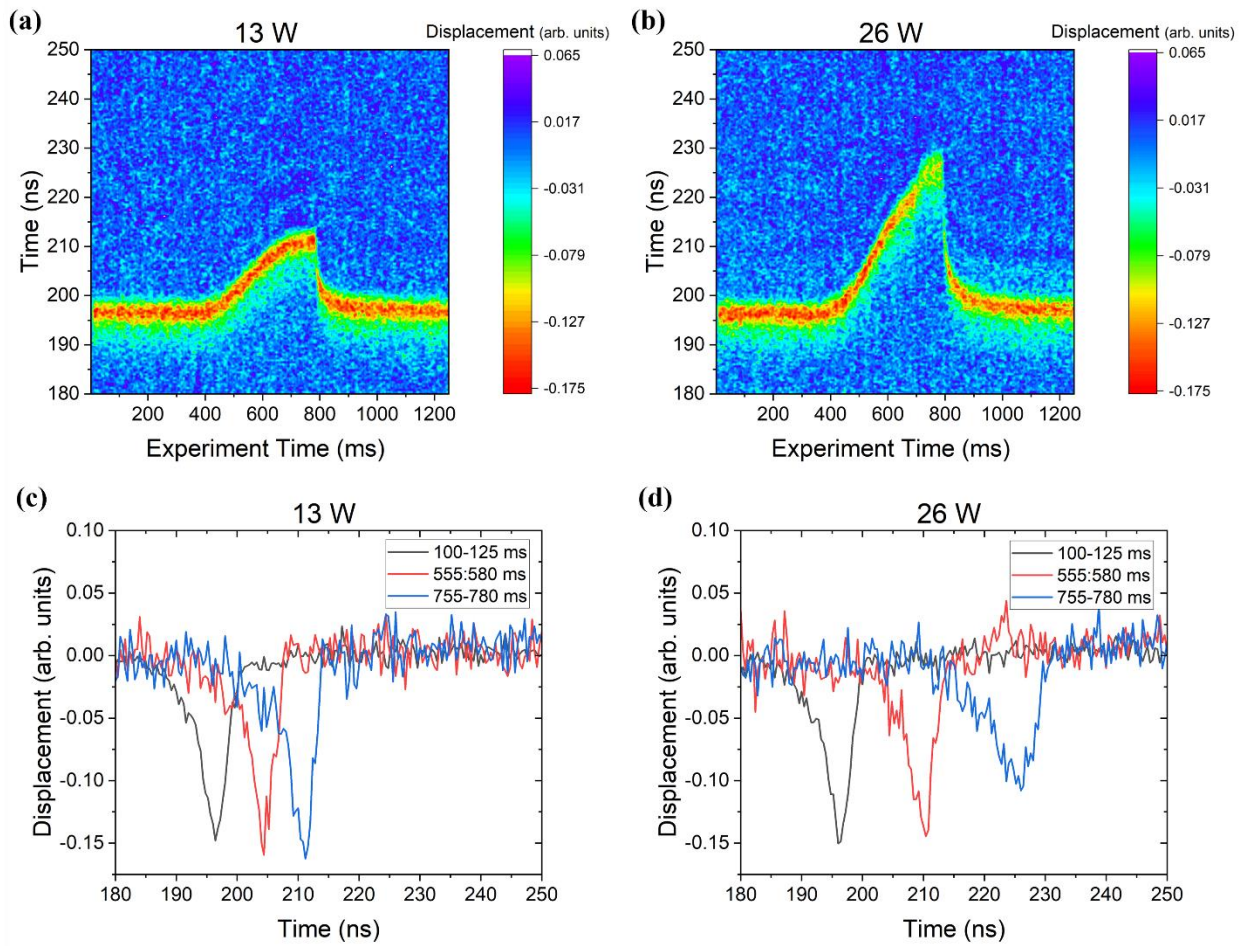
Figure 6-7. Temporal evolution of the displacement fields for laser heating power of *(a)* 13 W and *(b)* 26 W. Laser ultrasonic signals averaged between experiment times of 100-125 ms (black curve), 555-580 ms (red curve), and 755-780 ms (blue curve) for heating laser power of *(c)* 13 W and *(d)* 26 W.

6.4 Probing Transient Temperature Fields

In the next set of experiments, we scanned the heating laser across the static generation line and detection point which remained 600 μm apart. At each heating laser location, we took 50 experiments, with cooling time allowed between each experiment, before translating to the next position in order to be able to average the data and get higher signal to noise ratio than that achieved in Figure 6-7 from a single experiment. A schematic of this scanning experimental procedure is shown in Figure 6-8(a). In the first scanning experiment, we scanned the heating laser 0.8 mm in 0.05 mm increments at a heating laser power of 10 W with 45 s of cooling time between each experiment. The detection and excitation line were located in-line with the heating laser positioned at 0.4 mm. The CCD camera showed no visible markings or signs of melt resulted. Figure 6-8(b) shows the averaged delay curves at all 16 heating laser positions. A better way to visualize these delay curves, however, is seen in Figure 6-8(c) where we plot all the delay curves together. The abscissa gives the experiment time while the ordinate gives the heating laser position. The color bar represents the surface wave delay in ns. Here, we see the surface wave is delayed the most when directly in line with the heating laser at a position of 0.4 mm, and the delays are symmetric around this point.
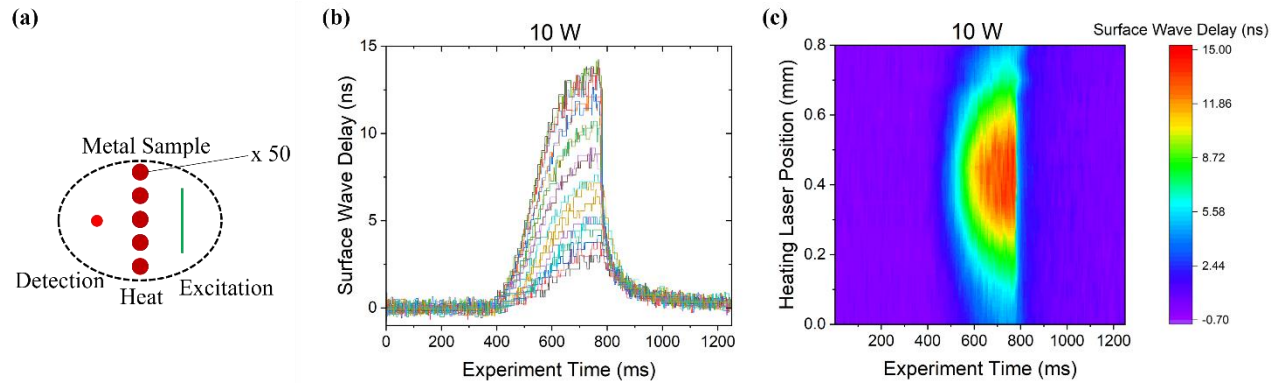
Figure 6-8. (a) Schematic of heating laser scanning experiments performed. ***(b)*** 16 averaged delay curves from all heating laser positions of the experiment performed at a heating laser power of 10 W. ***(c)*** Surface wave delays as a function of experiment time and heating laser position for heating laser power of 10 W.

Dispersive effects are characteristic of these transient depth-dependent laser-induced temperature fields, and as such, we look beyond the surface wave delays. Figure 6-9(a) and (b) shows displacement fields from this 10 W scanning experiments. The abscissa gives the time after the excitation pulse while the ordinate gives the heating laser position. The color bar represents the out of plane displacement of the surface. In these images, the SAW is represented by the negative-most amplitude shown in red. Figure 6-9(a) corresponds to an experiment time of $t = 200$ ms, which is before the heating starts, while Figure 6-9(b) corresponds to an experiment time of $t = 750$ ms, which is near the end of the heating pulse and about 50 ms before the heating is turned off. These displacements fields show the delay of the surface acoustic wave with respect to the constant arrivals at room temperature (Figure 6-9(a)). The surface wave delay is maximum when the heating laser position is in-line with the excitation laser line and the detection laser point, 0.4 mm in Figure 6-9(b). Also, the displacement field at $t = 750$ ms shows the SAW becoming dispersive near the in-line positions as seen by the SAW shape change.

69
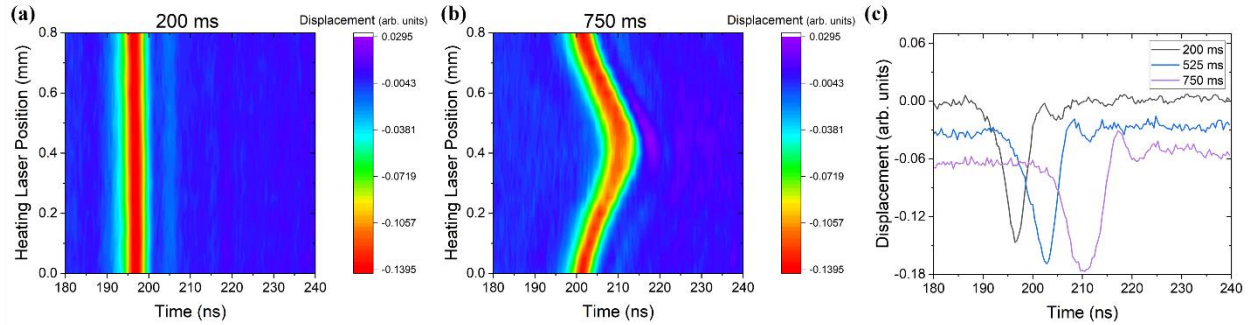
Figure 6-9. Displacement fields at a source to detector distance of 600 μm *(a)* in the absence of thermal effects and *(b)* from a laser-heated area at an experiment time of 750 ms from a heating laser power of 10 W. *(c)* Laser ultrasonic signals at experiment times of 200, 525, and 750 ms for a heating laser power of 10 W positioned at 0.4 mm.

In Figure 6-9(c) we show ultrasonic signals for the heating laser position in-line with the excitation and detection (at a 0.4 mm position), since this is where the ultrasonic signals are most sensitive to the heating, at different experiment times of t = 200, 525, and 750 ms. The first waveform shows the response in the absence of heating and the next two curves show the displacements responses after the heating laser is turned on. A significant degree of dispersion is seen for experiment times of t = 525 and 750 ms, with the higher frequency components becoming delayed by the high near-surface temperatures. The ultrasonic signals shown in Figure 6-9 are each averaged 50 times resulting in a much higher signal to noise ratio that the signals shown in Figure 6-7 which were from a single experiment. Thus, it is easier to observe dispersion in these averaged signals.

6.5 Inferring Temperature Rise from Simulations

In Section 2 above we perform 3-D finite element simulations for a laser-heated model using a 3-D temperature field we calculate from the same 500 ms heating pulse *p(t)* and Gaussian beam diameter of *d* = 185 μm as is used in experiments. A zoom-in of the simulation results of Figure 6-3 are included below in Figure 6-10 (a) and (b). We zoom-in to match the 180 to 240 ns

time used in our experimental results and the 0.8 mm distance through which we translated the heating laser in our scanning experiment. Note that in the simulation, the detection point is scanned while the excitation line and temperature field are kept static. The heating experiment results presented earlier are again included below in Figure 6-10 (c) and (d) to ease the discussion in comparing the theory to experiments.
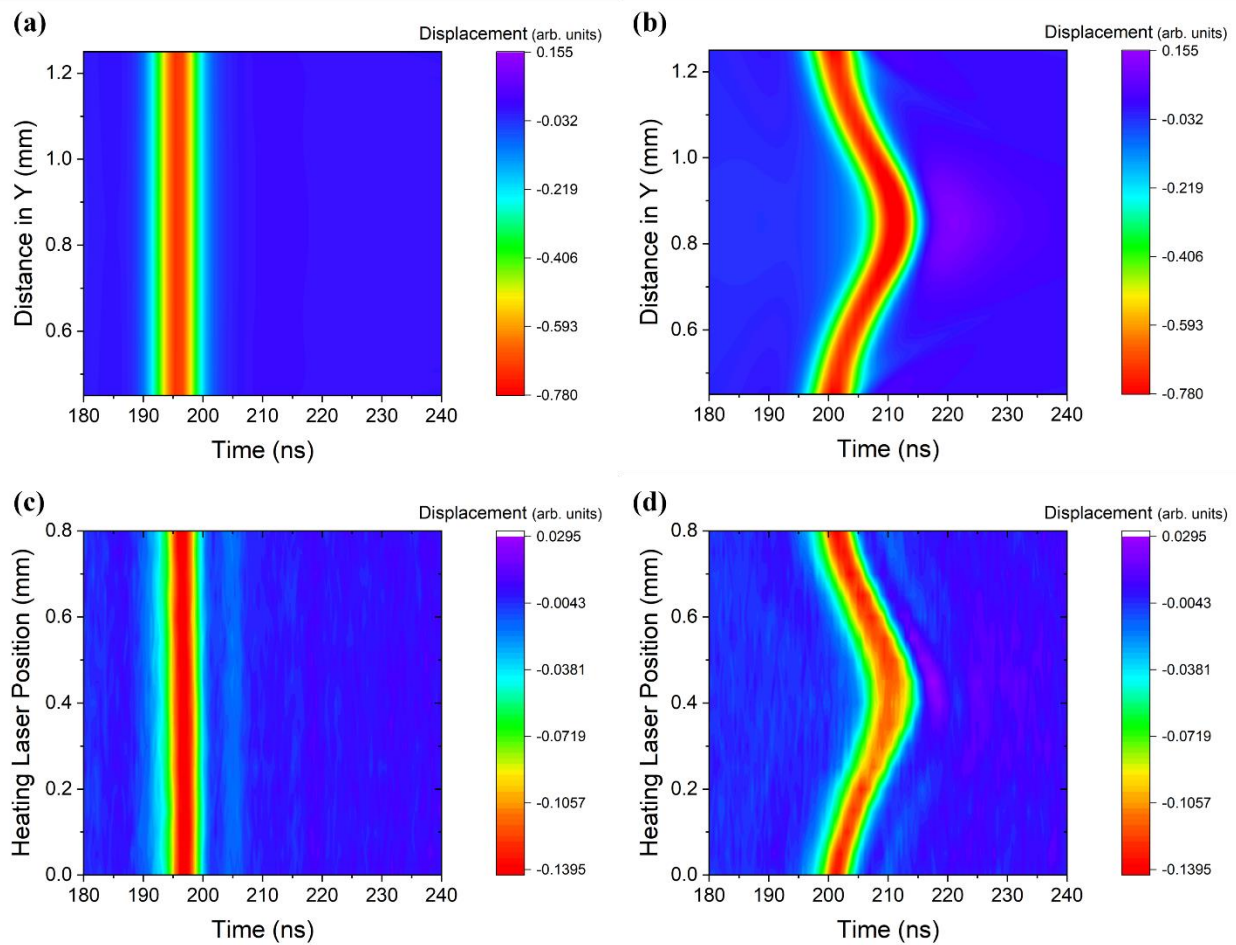
Figure 6-10. Simulated displacement fields at a source to detector distance of 600 μm resulting from the 3-D finite element model ***(a)*** in the absence of heating and ***(b)*** with the calculated temperature field for a 5 W laser power. Experimental results from the scanning experiment ***(c)*** in the absence of heating and ***(d)*** from the 10 W heating laser power.

Figure 6-10 shows good agreement between our simulation and experimental results. The resulting delay in both Figure 6-10(b) and (c) is of about 20 ns. We see dispersive effects, or change

in shape of the SAW, represented by the purple hue near the in-line positions, which is at 0.85 mm

in simulation and 0.4 mm in experiments, with these effects gradually decreasing from the in-line

position. Also, the shape in which the SAW is delayed with respect to the in-line position matches

between simulation and experiment results. Figure 6-11 shows individual waveform responses at

room temperature and from traversing the temperature field both from simulation and experiments

at their corresponding in-line positions. Here, too, we see very good agreement between our

simulation and experiment results. Thus, based on the maximum temperature of 387 K that results

in our simulations, we can infer that experimentally, a maximum temperature of about 387 K is

reached.
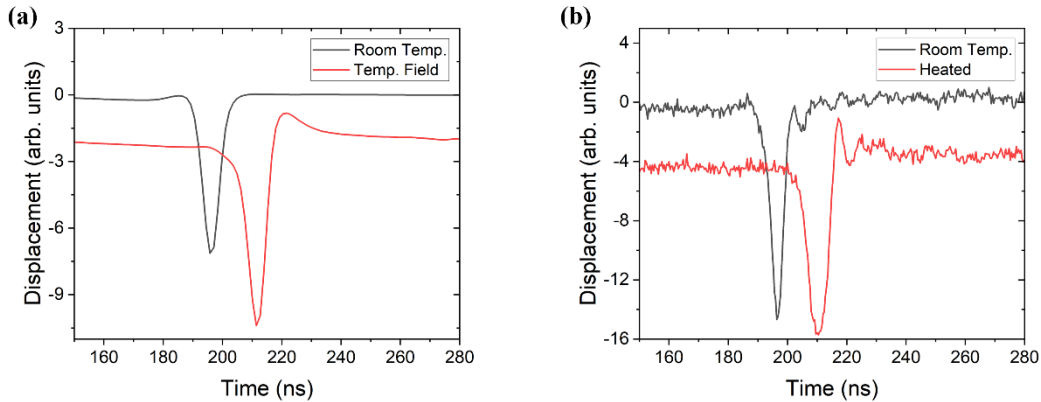
Figure 6-11. Laser ultrasonic signals at a source to detector distance of 600 μm resulting from **(a)** the 3-D finite element model in the absence of heating and with the calculated temperature field for a 5 W laser power and from **(b)** experimental results from the scanning experiment in the absence of heating and from the 10 W heating laser power.

A max power of 5 W was used in the calculated temperature field used in the simulations,

while a power if 10 W was measured in experiments. It would be more accurate to perform 3-D

thermal modeling, as was done with our 1-D thermal models, instead of using the analytical

formula listed in Equation 1 which does not consider temperature-dependent properties for

example. By adding 3-D thermal modeling to these simulations, we will achieve a very accurate

representation of what we see physically. These 3-D simulations can better inform future experimental measurements and the analysis of experimental data ultimately allowing us to solve the inverse problem to determine depth-dependent temperature profiles.

6.6 Probing Transient Melt Pools

In a second scanning experiment, a higher heating laser power of 13 W was used, and we scanned the heating laser 0.75 mm in 0.025 mm increments with only 30 s of cooling time between each experiment. The detection and excitation line were in-line with the heating laser at 0.375 mm. In this experiment, a clear melt line resulted on the sample and is shown in Figure 6-12(a). This image was taken with a digital microscope. Here we can see the laser line source to the right of the melt line, and the red dot is added to give a visual as to where the detection laser was approximately placed.

Figure 6-12(b) shows the surface delay as a function of experiment time and heating laser position for the 13 W experiment. When compared to the heating experiment (Figure 6-8(c)), the 13 W scanning experiment resulted in higher surface wave delays at earlier experiment times and starting at further locations from the in-line position as well. This indicates that the 13W experiment induces temperature fields with a greater spatial extent than the 10 W experiment. Figure 6-12(c) and (d) shows the displacement fields at $t = 200$ ms, which is before the heating starts, and at $t = 750$ ms, which is near the end of the heating. These displacements fields show the delay of the surface acoustic wave with respect to the constant arrivals at room temperature resulting from the melting experiment with the delay being maximum when the heating laser position is in-line with the excitation laser line and the detection laser point at 0.375 mm. When compared to the results from the heating experiment (Figure 6-9), we see that the delay and SAW shape change is more pronounced in the melting experiments. These dispersive effects are more

73

pronounced here due to the higher frequency SAW components becoming further delayed by the presence of the melted region.
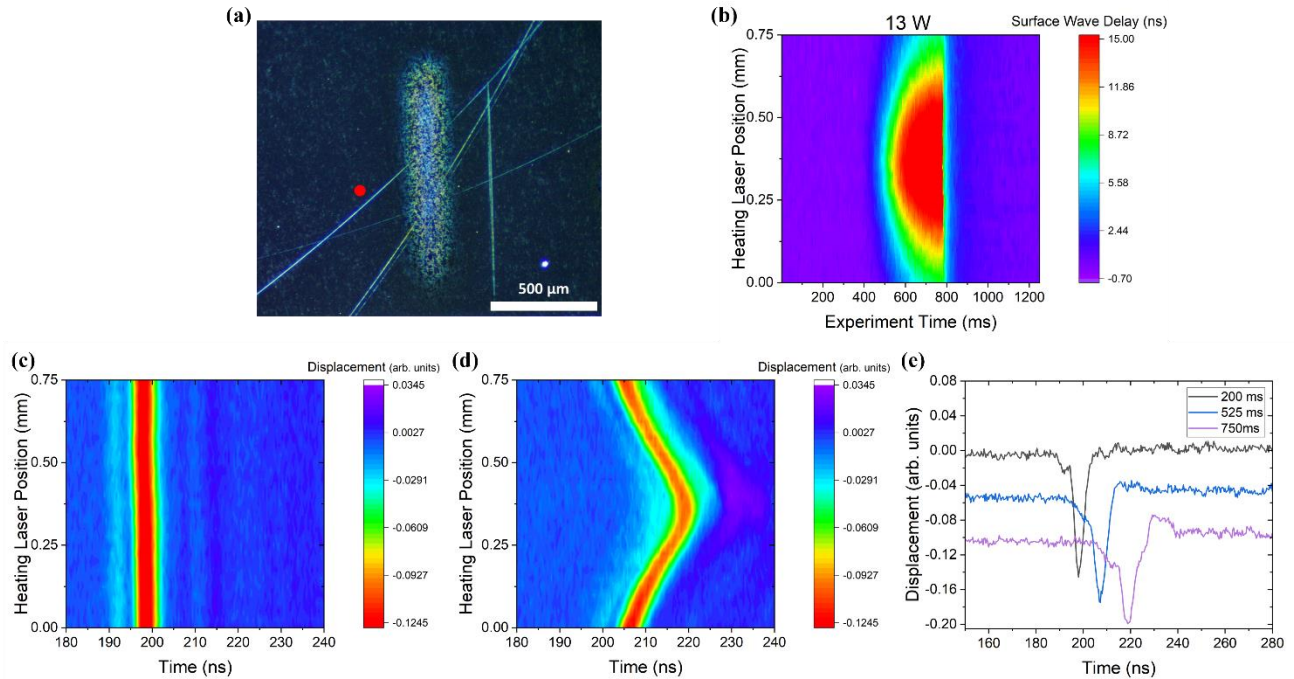
Figure 6-12. *(a)* Resulting melt line from scanning experiment performed at a heating laser power of 13 W. *(b)* Surface wave delays as a function of experiment time and heating laser position for heating laser power of 13 W. *(c)* Displacement fields at a source to detector distance of 600 μm in the absence of thermal effects and *(d)* from a laser-heated area at an experiment time of 750 ms from a heating laser power of 13 W. *(e)* Laser ultrasonic signals at experiment times of 200, 525, and 750 ms for a heating laser power of 13 W positioned at 0.375 mm.

Quantifying these dispersion effects and SAW shape changes can be potentially used to approximate melt pool depths. For this to happen, however, we first need to develop 3-D laser-melting models which can be used to inform future experimental measurements and the analysis of experimental data to determine melt pool extents and depths.

REFERENCES

1. Ready, J. F. *Effects of high-power laser radiation*. (Academic Press, 1971).

CHAPTER 7. CONCLUDING REMARKS

7.1 Conclusion

Laser-based ultrasonics is a non-contact technique used to monitor transient laser-induced heating and melting processes, which have become increasingly important to characterize with the recent push in developing laser-based advanced manufacturing techniques for their advantages over conventional manufacturing methods in their ability to manufacture complex, geometries, internal features, and light weight components. In these advanced manufacturing techniques, laser energy is absorbed by a material leading to local heating, melting, and vaporization. For example, in laser powder bed fusion an object is built in consecutive layers by laser melting of powder mechanically distributed over the build surface. Intra- and inter-layer integrity is dependent upon the rapid heating, melting, and solidification processes during which defects and material discontinuities are likely to form. The optimal laser parameters required to produce a part with the lowest number of processing defects are difficult to determine *a priori* due to the complexity of these manufacturing processes, so having *in-situ* control of the laser-induced processes is critical to ensure the integrity of the final product. All the work presented here was conducted on Titanium allow Ti-6Al-4V as it is commonly used in advanced manufacturing techniques due to its exceptional performance in high-value applications such as aerospace, military, and high precision technologies.

In Chapter 2, we present numerical simulations of one-dimensional thermal fields induced by a spatially-uniform continuous wave (CW) laser. This model allows for temperature calculations as a function of depth and melt front position at any time after heating begins. We show that slow laser heating leads to a temperature rise that is fairly uniform over the near-surface region, while rapid laser heating results in marked thermal gradients in this near-surface region.

In Chapter 3, we discuss the theory behind a laser ultrasonic model that calculates elastic displacement induced by a pulsed laser excitation and interferometric detection in a multi-layered plate on a semi-infinite solid. In this approach, the excitation laser source is represented as an equivalent elastic boundary source, and the transfer matrix technique is used to enforce the continuity of stress and displacement across all homogeneous and isotropic layer boundaries. The problem is solved in cylindrical coordinated using the integral transform technique where a Hankel transform of the elastic wave equation is taken with respect to the radial coordinate and a Laplace transform is taken with respect to time. The normal displacement as a function of time at a given radial distance is found through numerical inversion of the Hankel-Laplace transforms.

In Chapter 4, we present numerical simulations from the coupled theory in Chapters 2 and 3 where we model the pulsed laser excitation and interferometric detection of the CW laser-heated surface at a given time after laser-heating is begun. The one-dimensional temperature fields produced by the CW laser in Chapter 2 are discretized into 400 layers, the temperature-dependent elastic properties of each layer are calculated, and the elastic wave problem is then reduced to an analogous problem of wave propagation in a homogeneous, isotropic layered media. We show that for a spatially uniform heating beam, laser-induced surface acoustic waves are strongly influenced by surface heating conditions, are dispersive in the case of rapid heating where the thermally-induced mechanical property change is on the same spatial scale as the wavelength of the surface acoustic waves, and we show an abrupt velocity reduction upon the onset of surface melting.

In Chapter 5, we present the experimental setup built to study surface acoustic wave propagation through a laser-heated region of Ti-6Al-4V samples. We use a pulsed laser line source to generate surface acoustic waves and a photorefractive crystal-based interferometer to monitor the transient change of surface wave travel time associated with slow, high-power laser surface

heating and melting from a Gaussian heating beam placed between the source and receiver positions. Qualitative agreement between theory and experiment is observed with both showing a rapid reduction in the surface wave velocity at the onset of illumination and further decrease in surface wave velocity associated with melting. It is demonstrated that changes in the surface wave velocity can be used to track local heating and detect the onset of surface melting in real time.

In Chapter 6, we develop three-dimensional finite element acoustic models with which to study rapid, depth-dependent laser heating. We approximate a 3-D temperature field with the analytical solution for a Gaussian beam absorbed at the surface of a semi-infinite solid. We use a sigmoid function to represent the heating laser pulse and calculate 3-D thermal fields which we then import into the finite element software *Onscale*. We calculate the temperature-dependent elastic properties of each x, y, and z position for which the thermal field was calculated, and we calculate the elastic displacement normal to the surface as function of time at a given distance from the thermoelastic excitation line source. We also present a fast acquisition experimental setup built to probe transient depth-dependent temperature fields and at sufficiently high powers, melt pool depths. We use a pulsed laser line source to generate high frequency surface acoustic waves and a Michelson interferometer to monitor the surface wave dispersion associated with rapid, depth-dependent laser heating and melting from a Gaussian heating beam placed between the source and receiver positions. Experimental results show the real-time reduction in the surface wave velocity at the onset of illumination and further decrease in surface wave velocity associated with melting, as was observed in the slow-heating case. Agreement between theory and experiment is observed with both showing significant surface acoustic wave dispersion resulting from the rapid laser-heating since the induced thermal gradients cause the higher frequency components of the SAW that probe the near-surface temperatures to be delayed with respect to the lower frequencies that

77

penetrate further into the cooler bulk of the material. These dispersive effects are more pronounced at higher laser-heating powers which result in melt as the high frequency SAW components are further delayed by the presence of the melt. It is demonstrated that surface wave dispersion can be used to track transient depth-varying heating and melt.

The work presented here demonstrates the efficacy of using laser-based ultrasonics for *in-situ* monitoring of transient laser-induced heating and melting processes. This technique may ultimately find application in the mapping of transient laser-induced thermal fields and melt zones, providing critical information for real-time feedback and process control in advanced manufacturing systems including those relying on laser powder bed fusion. It is important to point out that laser additive manufacturing techniques are conducted in a layer-wise manner, and track formation and overlap add complexity to the heating and melting processes.

7.2 Suggestions for Future Work

Qualitative agreement between theory and experiments achieved in this work allows for very well-informed experimental measurements and aids the analysis of experimental data. However, there is significant work to be done to achieve quantitative agreement. First, comprehensive 3-D thermal modeling is required for better representation of laser-heating and melting to be included in the acoustic finite element simulations. The computation fluid dynamic software *Flow-3D* is recommended for the 3-D laser-heating and melting models. Having accurate 3-D thermal models can ultimately allow us to solve the inverse problem to determine depth-dependent temperature profiles and melt pool depths. Also, implementing thermal imaging could allow for quantitative agreement between surface wave delay and induced surface temperatures.

This work includes a lot of real-time cooling experimental data for the slow and rapid laser-heating and melting cases. Further data analysis and cooling simulations are needed to extract valuable information, such as knowing when the metal has been completely re-solidified as this is also a very important process in advanced manufacturing processes.

Using *Flow-3D* simulations could also play a huge role in achieving laser-ultrasonic diagnostics in real laser-based advanced manufacturing systems. This software includes the capability to model scanning heating lasers, metal powder beds, and melt track overlap. Such high-fidelity models could allow us to very accurately study surface acoustic wave interaction in these complex heating and melting processes.

After quantitative measurements of depth-varying temperatures and melt pool depths are achieved experimentally, next steps in experimentation could include implementing an Argon gas environment. Most advanced manufacturing techniques use these environments to remove oxidization and discoloration due to the heating, so it would be beneficial to work in a similar environment. Also, studying surface acoustic wave interaction in laser-melted metal powder beds is a significant next step. Simple metal powder lines could be melted by translating a high-power CW heating laser, as was done in this work in Chapter 6, and an excitation line source and detection point could be placed on opposite sides to observe the metal powder being heated, melted, and solidified in real-time. *Flow3D* simulations can be used to guide these experiment measurements and data analysis.

BIBLIOGRAPHY

Achenbach, J. D. The Thermoelasticity of Laser-Based Ultrasonics. *Journal of Thermal Stresses* **28**, 713–727 (2005).

Alleyne, D. & Cawley, P. A two-dimensional Fourier transform method for the measurement of propagating multimode signals. *The Journal of the Acoustical Society of America* **89**, 1159–1168 (1991).

Arias, I. & Achenbach, J. D. Thermoelastic generation of ultrasound by line-focused laser irradiation. *International Journal of Solids and Structures* **40**, 6917–6935 (2003).

Bertoni, H. L. & Tamir, T. Unified theory of Rayleigh-angle phenomena for acoustic beams at liquid-solid interfaces. *Appl. Phys.* **2**, 157–172 (1973).

Biot, M. A. The interaction of Rayleigh and Stoneley waves in the ocean bottom*. *Bulletin of the Seismological Society of America* **42**, 81–93 (1952).

Blouin, A. & Monchalin, J. Detection of ultrasonic motion of a scattering surface by two-wave mixing in a photorefractive GaAs crystal. *Appl. Phys. Lett.* **65**, 932–934 (1994).

Bucaro, J. A. & Flax, L. Application of acoustic surface waves to the study of surface properties of ion-exchanged glass. *Journal of Applied Physics* **45**, 765–774 (1974).

Casas, J., Kéita, N. M. & Steinemann, S. G. Sound Velocity in Liquid Titanium, Vanadium and Chromium. *Physics and Chemistry of Liquids* **14**, 155–158 (1984).

Cheng, A., Murray, T. W. & Achenbach, J. D. Simulation of laser-generated ultrasonic waves in layered plates. *The Journal of the Acoustical Society of America* **110**, 848–855 (2001).

Cheng, J., Wu, L. & Zhang, S. Thermoelastic response of pulsed photothermal deformation of thin plates. *Journal of Applied Physics* **76**, 716–722 (1994).

Dai, T. *et al.* Laser ultrasonic testing for near-surface defects inspection of 316L stainless steel fabricated by laser powder bed fusion. *China Foundry* **18**, 360–368 (2021).

Dalong Liu & Ebbini, E. S. Real-Time 2-D Temperature Imaging Using Ultrasound. *IEEE Trans. Biomed. Eng.* **57**, 12–16 (2010).

Davies, S. J., Edwards, C., Taylor, G. S. & Palmer, S. B. Laser-generated ultrasound: its properties, mechanisms and multifarious applications. *J. Phys. D: Appl. Phys.* **26**, 329–348 (1993).

Davis, G. *et al.* Laser ultrasonic inspection of additive manufactured components. *Int J Adv Manuf Technol* **102**, 2571–2579 (2019).

Delaye, P. *et al.* Detection of ultrasonic motion of a scattering surface by photorefractive InP:Fe under an applied dc field. *J. Opt. Soc. Am. B* **14**, 1723 (1997).

Doyle, P. A. & Scala, C. M. Near-field ultrasonic Rayleigh waves from a laser line source. *Ultrasonics* **34**, 1–8 (1996).

du Plessis, A. & le Roux, S. G. Standardized X-ray tomography testing of additively manufactured parts: A round robin test. *Additive Manufacturing* **24**, 125–136 (2018).

Everton, S., Dickens, P., Tuck, C. & Dutton, B. Using Laser Ultrasound to Detect Subsurface Defects in Metal Laser Powder Bed Fusion Components. *JOM* **70**, 378–383 (2018).

Everton, S. K., Hirsch, M., Stravroulakis, P., Leach, R. K. & Clare, A. T. Review of in-situ process monitoring and in-situ metrology for metal additive manufacturing. *Materials & Design* **95**, 431–445 (2016).

Forien, J.-B. *et al.* Detecting keyhole pore defects and monitoring process signatures during laser powder bed fusion: A correlation between in situ pyrometry and ex situ X-ray radiography. *Additive Manufacturing* **35**, 101336 (2020).

Gillespie, J. *et al. In situ* characterization of laser-generated melt pools using synchronized ultrasound and high-speed X-ray imaging. *The Journal of the Acoustical Society of America* **150**, 2409–2420 (2021).

Glorieux, C. *et al.* Surface acoustic wave depth profiling of elastically inhomogeneous materials. *J. Appl. Phys.* **88**, 4394 (2000).

Goossens, J. *et al.* Surface acoustic wave depth profiling of a functionally graded material. *Journal of Applied Physics* **102**, 053508 (2007).

Grasso, M. & Colosimo, B. M. Process defects and *in situ* monitoring methods in metal powder bed fusion: a review. *Meas. Sci. Technol.* **28**, 044005 (2017).

Gunter, P. & Huignard, J. P. *Photorefractive Materials and Their Applications I*. vol. 61 (Springer Berlin Heidelberg, 1988).

Guo, Z., Achenbach, J. D., Madan, A., Martin, K. & Graham, M. E. Integration of modeling and acoustic microscopy measurements for thin films. *The Journal of the Acoustical Society of America* **107**, 2462–2471 (2000).

Harke, K. J., Calta, N., Tringe, J. & Stobbe, D. Laser-based ultrasound interrogation of surface and sub-surface features in advanced manufacturing materials. *Sci Rep* **12**, 3309 (2022).

Hinterlechner, I. *et al.* In-situ monitoring of phase transformation in Ti-6Al-6V-2Sn using laser ultrasonics. *Nondestructive Testing and Evaluation* **33**, 130–138 (2018).

Ing, R. K. & Monchalin, J. -P. Broadband optical detection of ultrasound by two-wave mixing in a photorefractive crystal. *Appl. Phys. Lett.* **59**, 3233–3235 (1991).

Jian, X., Dixon, S., Guo, N. & Edwards, R. Rayleigh wave interaction with surface-breaking cracks. *Journal of Applied Physics* **101**, 064906 (2007).

Khairallah, S. A., Anderson, A. T., Rubenchik, A. & King, W. E. Laser powder-bed fusion additive manufacturing: Physics of complex melt flow and formation mechanisms of pores, spatter, and denudation zones. *Acta Materialia* **108**, 36–45 (2016).

Khairallah, S. A. *et al.* Controlling interdependent meso-nanosecond dynamics and defect generation in metal 3D printing. *Science* **368**, 660–665 (2020).

Kil-Mo Koo, Dong-Gyu Jeong, Jong-Ho Choi, & Duck-Young Ko. A new measurement system of very high temperature in atomic pile using ultrasonic delay time. in *Proceedings of IEEE Region 10 International Conference on Electrical and Electronic Technology. TENCON 2001 (Cat. No.01CH37239)* vol. 2 860–863 (IEEE, 2001).

King, W. E. *et al.* Laser powder bed fusion additive manufacturing of metals; physics, computational, and materials challenges. *Applied Physics Reviews* **2**, 041304 (2015).

Kiss, A. M. *et al.* Laser-Induced Keyhole Defect Dynamics during Metal Additive Manufacturing. *Adv. Eng. Mater.* **21**, 1900455 (2019).

Klein, M. & Sears, J. Laser ultrasonic inspection of laser cladded 316LSS and TI-6-4. in *International Congress on Applications of Lasers & Electro-Optics* 1006 (Laser Institute of America, 2004).

Kouprianoff, D., Yadroitsava, I., du Plessis, A., Luwes, N. & Yadroitsev, I. Monitoring of Laser Powder Bed Fusion by Acoustic Emission: Investigation of Single Tracks and Layers. *Front. Mech. Eng.* **7**, 678076 (2021).

Kruger, S. E. & Damm, E. B. Monitoring austenite decomposition by ultrasonic velocity. *Materials Science and Engineering: A* **425**, 238–243 (2006).

Lai, P. *et al.* Real-Time Monitoring of High-Intensity Focused Ultrasound Lesion Formation Using Acousto-Optic Sensing. *Ultrasound in Medicine & Biology* **37**, 239–252 (2011).

Manzo, A. J. & Helvajian, H. Pulsed laser ultrasonic excitation and heterodyne detection for *in situ* process control in laser 3D manufacturing. *Journal of Laser Applications* **29**, 012012 (2017).

Manzo, A. J. & Helvajian, H. Utility of optical heterodyne displacement sensing and laser ultrasonics as in situ process control diagnostic for additive manufacturing. *Opt. Eng.* **57**, 1 (2018).

Matthews, M. J. *et al.* Denudation of metal powder layers in laser powder bed fusion processes. *Acta Materialia* **114**, 33–42 (2016).

McDonald, F. A. On the precursor in laser-generated ultrasound waveforms in metals. *Appl. Phys. Lett.* **56**, 230–232 (1990).

Meegan, G. D., Hamilton, M. F., Il'inskii, Yu. A. & Zabolotskaya, E. A. Nonlinear Stoneley and Scholte waves. *The Journal of the Acoustical Society of America* **106**, 1712–1723 (1999).

Mercelis, P. & Kruth, J. Residual stresses in selective laser sintering and selective laser melting. *Rapid Prototyping Journal* **12**, 254–265 (2006).

Mills, K. C. *Recommended values of thermophysical properties for selected commercial alloys*. (2002).

Mitchell, J. A., Ivanoff, T. A., Dagel, D., Madison, J. D. & Jared, B. Linking pyrometry to porosity in additively manufactured metals. *Additive Manufacturing* **31**, 100946 (2020).

Morales, R. E., Harke, K. J., Tringe, J. W., Stobbe, D. M. & Murray, T. W. Real-time laser ultrasonic monitoring of laser-induced thermal processes. *Sci Rep* **12**, 9865 (2022).

Moreau, A. *et al.* On-line measurement of texture, thickness and plastic strain ratio using laser-ultrasound resonance spectroscopy. *Ultrasonics* **40**, 1047–1056 (2002).

Murray, T. W., Krishnaswamy, S. & Achenbach, J. D. Laser generation of ultrasound in films and coatings. *Appl. Phys. Lett.* **74**, 3561–3563 (1999).

Murray, T. W., Balogun, O., Steen, T. L., Basu, S. N. & Sarin, V. K. Inspection of compositionally graded mullite coatings using laser based ultrasonics. *International Journal of Refractory Metals and Hard Materials* **23**, 322–329 (2005).

Murray, T. W. *et al.* A New In-Line Laser-Based Acoustic Technique for Pillar Bump Metrology. *Journal of Microelectronics and Electronic Packaging* **13**, 58–63 (2016).

Murray, T. W. & Wagner, J. W. Laser generation of acoustic waves in the ablative regime. *Journal of Applied Physics* **85**, 2031–2040 (1999).

Obbard, R. W. *et al.* Micro computed tomography for in situ analysis of subsurface structure. in *2021 IEEE Aerospace Conference (50100)* 1–10 (IEEE, 2021).

Ogi, H. *et al.* Titanium's high-temperature elastic constants through the hcp–bcc phase transformation. *Acta Materialia* **52**, 2075–2080 (2004).

Ozisik, M. N., Orlande, H. R. B., Colaco, M. J. & Cotta, R. M. *Finite difference methods in heat transfer*. (2017).

Queheillalt, D. T. & Wadley, H. N. G. Laser ultrasonic sensing of the melting and solidification of cadmium telluride. *Journal of Crystal Growth* **225**, 34–44 (2001).

Ready, J. F. *Effects of high-power laser radiation*. (Academic Press, 1971).

Rieder, H., Dillhöfer, A., Spies, M., Bamberg, J. & Hess, T. Ultrasonic online monitoring of additive manufacturing processes based on selective laser melting. in 184–191 (2015).

Rose, J. L. *Ultrasonic waves in solid media*. (Cambridge University Press, 1999).

Rose, L. R. F. Point-source representation for laser-generated ultrasound. *The Journal of the Acoustical Society of America* **75**, 723–732 (1984).

Saleh, B. E. A. & Teich, M. C. *Fundamentals of photonics*. (Wiley, 2019).

Sanderson, T., Ume, C. & Jarzynski, J. Laser generated ultrasound: a thermoelastic analysis of the source. *Ultrasonics* **35**, 115–124 (1997).

Saunders, N., Guo, U. K. Z., Li, X., Miodownik, A. P. & Schillé, J.-Ph. Using JMatPro to model materials properties and behavior. *JOM* **55**, 60–65 (2003).

Scruby, C. B. & Drain, L. E. *Laser Ultrasonics: Techniques and Applications*. (Routledge, 2019).

Shevchik, S. A., Masinelli, G., Kenel, C., Leinenbach, C. & Wasmer, K. Deep Learning for *In Situ* and Real-Time Quality Monitoring in Additive Manufacturing Using Acoustic Emission. *IEEE Trans. Ind. Inf.* **15**, 5194–5203 (2019).

Shi, Y.-A. *et al.* A Method for Reconstructing Internal Temperature Distribution in Solid Structure. *J Nondestruct Eval* **39**, 48 (2020).

Shinbine, A., Garcin, T. & Sinclair, C. In-situ laser ultrasonic measurement of the hcp to bcc transformation in commercially pure titanium. *Materials Characterization* **117**, 57–64 (2016).

Singh, R. K. & Narayan, J. A novel method for simulating laser-solid interactions in semiconductors and layered structures. *Materials Science and Engineering: B* **3**, 217–230 (1989).

Smith, R. J. *et al.* Spatially resolved acoustic spectroscopy for selective laser melting. *Journal of Materials Processing Technology* **236**, 93–102 (2016).

Smithells, C. J., Gale, W. F. & Totemeier, T. C. *Smithells metals reference book*. (Elsevier Butterworth-Heinemann, 2004).

Snow, Z., Diehl, B., Reutzel, E. W. & Nassar, A. Toward in-situ flaw detection in laser powder bed fusion additive manufacturing through layerwise imagery and machine learning. *Journal of Manufacturing Systems* **59**, 12–26 (2021).

Solymar, L., Webb, D. J. & Grunnet-Jepsen, A. *The physics and applications of photorefractive materials*. (Clarendon Press ; Oxford University Press, 1996).

Spicer, J. B., McKie, A. D. W. & Wagner, J. W. Quantitative theory for laser ultrasonic waves in a thin plate. *Appl. Phys. Lett.* **57**, 1882–1884 (1990).

Steg, R. G. & Klemens, P. G. Scattering of Rayleigh Waves by Surface Irregularities. *Phys. Rev. Lett.* **24**, 381–383 (1970).

Szabo, T. L. Obtaining subsurface profiles from surface−acoustic−wave velocity dispersion. *Journal of Applied Physics* **46**, 1448–1454 (1975).

Tanaka, T. & Izawa, Y. Nondestructive Detection of Small Internal Defects in Carbon Steel by Laser Ultrasonics. *Jpn. J. Appl. Phys.* **40**, 1477–1481 (2001).

Thijs, L., Verhaeghe, F., Craeghs, T., Humbeeck, J. V. & Kruth, J.-P. A study of the microstructural evolution during selective laser melting of Ti–6Al–4V. *Acta Materialia* **58**, 3303–3312 (2010).

Thomson, W. T. Transmission of Elastic Waves through a Stratified Solid Medium. *Journal of Applied Physics* **21**, 89–93 (1950).

Von Allmen, M. & Blatter, A. *Laser-beam interactions with materials: physical principles and applications*. (Springer, 1995).

Welsch, G., Boyer, R. & Collings, E. W. *Materials properties handbook: titanium alloys*. (ASM International, 1994).

Wildenschild, D. & Sheppard, A. P. X-ray imaging and analysis techniques for quantifying pore-scale structure and processes in subsurface porous medium systems. *Advances in Water Resources* **51**, 217–246 (2013).

Wood, R. F. & Giles, G. E. Macroscopic theory of pulsed-laser annealing. I. Thermal transport and melting. *Phys. Rev. B* **23**, 2923–2942 (1981).

Yamada, H., Kosugi, A. & Ihara, I. Noncontact Monitoring of Surface Temperature Distribution by Laser Ultrasound Scanning. *Jpn. J. Appl. Phys.* **50**, 07HC06 (2011).

Yang, T. *et al.* In-situ monitoring and ex-situ elasticity mapping of laser induced metal melting pool using ultrasound: Numerical and experimental approaches. *Journal of Manufacturing Processes* **71**, 178–186 (2021).

Ye, J. *et al.* Energy Coupling Mechanisms and Scaling Behavior Associated with Laser Powder Bed Fusion Additive Manufacturing. *Adv. Eng. Mater.* **21**, 1900185 (2019).

Zhang, F., Krishnaswamy, S., Fei, D., Rebinsky, D. A. & Feng, B. Ultrasonic characterization of mechanical properties of Cr- and W-doped diamond-like carbon hard coatings. *Thin Solid Films* **503**, 250–258 (2006).

APPENDIX I

C++ Code for Coupled 1-D Laser-Heated Thermal Model and Acoustic Wave Generation

All constants set for Titanium alloy Ti-6Al-4V

```
# include <stdio.h>

# include <stddef.h>

# include <stdlib.h>

# include <math.h>

# include <conio.h>

# include <fstream>

# include <iostream>

# include <sstream>

# include <string>

#include  <complex>

using namespace std;

#define _USE_MATH_DEFINES

#define PI      3.14159265358979323846264338327950288/* pi to machine precision, defined in math.h */

#define TWOPI       (2.0*PI)


/* C program for the inversion of the Laplace transform and the Hankel

transform associated with the thermoelastic response of an infinite plate

to the action of a laser heating pulse at the plate boundary- translated

by T. Murray from fortran program written by J.B. Spicer and adapted by R.

Morales in 2021 to couple laser heating and acoustic generation in a multi-

layered model*/


void main(){

        double *allocate_real_vector(int, int);

        void free_real_vector(double *, int, int);

        double **allocate_real_matrix(int, int, int, int);
```

```cpp
void free_real_matrix(double **, int, int, int);
double *allocate_double_vector(int l, int y);
void free_double_vector(double *v, int l);
int  i, j, m, q, cnt, n, tot, melting, num1, starter, ji, nm, cnt2, ct1;
double c, p, I, a, dt, dz, I1, I2, cp, rho, L, K2, st1, st2, ds, gs, power1;
double beta, po, A, R0, Ts, Hv, Tlv, density, flux, flux1, totflux, vsurface, R1;
double cvsurface, dsurface, totsurface, enout, marker, pressure;
double l1, Tm, Rf, I11, I12, I21, I22, I23, kip;
char string[80]; char string2[80];
double expulsion, expdist, totexpul, power, IA, CT;
double *TP, *s, *u, *z, *R, *b, *Q, *STP, *k, *ka, *kb;
double Temp, alphaT, rhoT, v, E, G, sumofT, avgT, cT, cL;
double **param;
double solid(double g, complex<double> omega, int l, int n,
        double** param, double* prm, double s2rd, int);
double qadrat(double*, double, double, complex<double>, int, int, double**,
        double (*)(double, complex<double>, int, int, double**, double*, double, int),
        double[], double*, double, int);
void lapinv(double*, int, double, double, double, double, int);

int l = 1;//l=1 for the half space.
char configuration = 'b';// a for no substrate,b for plate(s) on a substrate,c for halfspace;
double *prm, x, error[4], *tmp1;
complex<double> omega;
double totks, smod, sposs, sden, pi = 3.14159265358979;
double tsmin, tsmax, per, w, rfreq, s2rd, rhankinv, chankinv;
double gbeg, gend, h, st, sl;
double voferror, errorlp, alp1, alp2, gopi, scop;
int kmax, ior, pts;
int index;
```

```c
double Emod, lam3, poss;

int timeStep, cts, tottime, totAc, spcStep;


FILE *lp, *mp, *np, *fp;

FILE *ap, *tp;

FILE *kp;

ap = fopen("acousticData.dat", "w");

tp = fopen("timeAcoustic.dat", "w");


lp = fopen("heating25.dat", "w");

mp = fopen("averageTempsandProps.dat", "w");

fp = fopen("TempField.dat", "w");

np = fopen("avgTempField.dat", "w");

kp = fopen("param.dat", "w");


STP = allocate_double_vector(1, 50000);

TP = allocate_double_vector(1, 50000);

s = allocate_double_vector(1, 50000);

u = allocate_double_vector(1, 50000);

z = allocate_double_vector(1, 50000);

R = allocate_double_vector(1, 50000);

Q = allocate_double_vector(1, 50000);

b = allocate_double_vector(1, 50000);

k = allocate_double_vector(1, 50000);

ka = allocate_double_vector(1, 50000);

kb = allocate_double_vector(1, 50000);


tot = 4000; /* TOTAL NUMBER OF SPACE STEPS */

totAc = 4000; /* TOTAL NUMBER OF SPACE STEPS FOR ACOUSTIC CALCS*/

spcStep = 10;  /* SPACE STEPS TO AVERAGE OVER FOR ACOUSTIC CALCS*/
```

```
tottime = 80001; // 51200;

timeStep = 3200;


l1 = 8e-5; /* THICKNESS (CM)- DIMENSIONLESS LENGTH CONSTANT
                              DZ (ACTUAL)= (DZ)(L1) */

dz = 0.075; /* DIMENSIONLESS SPACE STEP */

dt = 0.075;  /* DIMENSIONLESS TIME STEPS */


int nn = totAc; // number of plate layers

totks = 0.0;

l = l + nn;

prm = allocate_real_vector(0, 5);


/* INITIALIZE VARIOUS VALUES TO ZERO */


totexpul = 0.0; expulsion = 0.0; starter = 1; nm = 0; totsurface = 0.0;

enout = 0.0; marker = 0.0; kip = 0.0; pressure = 0.0;


/* INPUT POWER DENSITY AND OUTPUT FILE NAMES */


printf("Enter the power density in MW/cm2: ");

scanf("%lf", &power);

printf("\n");

printf("The power density is %lf\n", power);

printf("\n");


/* PHYSICAL CONSTANTS */


a = 1.0e7; /* was 1e6 1/CM  ABSORPTION DEPTH */
```

power = (power*1e6); /* CONVERT POWER DENSITY W/CM2 */

ds = 0.0; /* INITIAL MOVEMENT OF MELT FRONT */

Tm = 1943.0; /* MELTING TEMPERATURE */

rho = 4.42; /* DENSITY G/CM3 */

L = (390)*rho; /*   LATENT HEAT J/CM3   */

K2 = 0.07; /* DIMENSIONLESS CONSTANT W/CMK .. Thermal Conductivity..*/

melting = 0; /* MELTING=1.0 WHEN MELT FRONT STARTS TO PROPAGATE */

st1 = 0.0; st2 = 0.0; /* TWO VARIABLES FOR DEFINING POSITION OF MELT
FRONT */

m = tot; /* NUMBER OF SPACE STEPS BEFORE MELT FRONT */

n = tot - m; /* NUMBER OF SPACE STEPS AFTER MELT FRONT */

cnt = 0; /* COUNTER FOR WRITE TO FILE */

cnt2 = 0; /* COUNTER FOR TEMPERATURE MATRIX */

/* CONSTANTS FOR VAPORIZATION CALCULATION */

A = 47.867; /* ATOMIC WEIGHT g/mol */

```
po = .001*1.013e8; /* AMBIENT PRESSURE g/(sec2 m) */

R1 = 8.314e3; /* GAS CONSTANT (UNITS) g m2/(sec2 mol K) */

Tlv = 3560.0; /* VAPORIZATION TEMPERATURE K */

beta = 1.0;  /* COUPLING CONSTANT */

density = rho * 100 * 100 * 100; /* g/m3 */

Hv = 421000.0; /* LATENT HEAT J/mol */

R0 = 8.314; /* GAS CONSTANT (UNITS) J/ mol K  */

/* INITIAL TEMPERATURE DISTRIBUTION (corresponds to 300K)*/

for (i = 1; i <= tot + 100; i++) { TP[i] = (-0.8456); } /*  -0.6848*/

/* J GIVES TOTAL NUMBER OF TIME STEPS */

for (j = 1; j <= tottime; j++) {

        n = tot - (m + 1);                      /* n= number of space steps behind front */

        /* TERMS FOR HEAT EQUATION */

        for (i = 1; i <= tot + 5; i++) {
                if (TP[i] > 0.0) /* melt properties */
                {
                        CT = TP[i] * Tm + Tm;
```

```
                    k[i] = 34.6 / 100; /*  J/cmKs */

                    cp = 0.83 * rho; /* J/cm3K */

          }


          else /* solid properties */

          {

                    CT = TP[i] * Tm + Tm;

                    cp = 0.4115 + 2e-4*CT + 5e-10*CT*CT; /* J/gK */

                    cp =  (cp)*rho;/*         Specific Heat J/cm3K */

                    k[i] = (-0.797 + 18.2e-3*CT - 2e-6*CT*CT)/100;    /*
Thermal Conductivity W/cmK*/

          }

          Q[i] = (k[i] * L) / (cp*Tm*K2);

          R[i] = Q[i] * dt / (dz*dz);

     }

     if (j == 1) {

          for (i = 1; i <= tot + 4; i++) {

                    ka[i] = 1.0;

                    kb[i] = 1.0;

          }

     }

     /* weighting fnc, not used- very small variation of

     K spatially at every time step. approx=1*/


     /* REFLECTIVITY */


     if (TP[1] > 0.0) { Rf = .6154; }

     else { Rf = .6154; } /* */


     /* BOUNDRY CONDITION- FRONT SURFACE */
```

```c
        s[1] = (1.0 / 6.0 - R[1] + 5.0 / 3.0 + 2.0*R[1]) / Q[1];

        u[1] = ((1.0 / 6.0 - R[2]) / Q[2]) / s[1];

        /* INTERNAL NODES */

        for (q = 2; q <= m - 1; q++) {

                b[q] = (1.0 / 6.0 - R[q - 1]) / Q[q - 1];

                s[q] = (5.0 / 3.0 + 2.0*R[q]) / Q[q] - b[q] * u[q - 1];

                u[q] = ((1.0 / 6.0 - R[q + 1]) / Q[q + 1]) / s[q];
        }

        /* MELT FRONT -LEFT SIDE- BOUNDARY CONDITION */

        if (melting == 1) {

                b[m] = 1.0 / (3.0*Q[m - 1] * (2.0 + st1)) - 2.0*dt / (dz*dz*(2.0 + st2));

                s[m] = 2.0 / Q[m] - 1.0 / (3.0*Q[m] * (1.0 + st1)) + (2.0*dt) / (dz*dz*(1.0
+ st2)) - b[m] * u[m - 1];
        }

        /* BACK SURFACE BOUNDARY CONDITION */

        else {
```

```
            b[m] = (1.0 / 6.0 - R[m - 1]) / Q[m - 1];


            s[m] = ((1.0 / 6.0 - R[m] + 5.0 / 3.0 + 2.0*R[m]) / Q[m]) - b[m] * u[m - 1];

        }


        // cnt = cnt + 1; if (cnt == timeStep) { cnt = 0; }   /* Counter-write to file when
counter = 0 */


    /* LASER SOURCE FIRST LAYER */


        /* gs = ((j*dt*L*l1*l1) / (Tm*K2) - 25e-9) / 6.0e-9*

                ((j*dt*L*l1*l1) / (Tm*K2) - 25e-9) / 6.0e-9; */ /*9.6 for 16ns pulse
(FWHM) */

        I = power; /* * exp(-1.0*gs); */
        I1 = (1.0 - Rf)*I*exp(-1.0*(0.0)*(a*dz*l1));
        I2 = (I1*(1.0 - exp(-a * dz*l1))*2.0*dt*l1*l1) / (k[1] * dz*Tm*l1);


        /* SOURCE TERM FOR FRONT SURFACE*/


        if (melting == 1) {
                z[1] = (((1.0 / 6.0 + ka[1] * R[1] + 5.0 / 3.0 - 2.0*R[1]) / Q[1])*TP[1]
                        + ((1.0 / 6.0 + kb[1] * R[2]) / Q[2])*TP[2] + I2 - enout) / s[1];
        }


        else {
                z[1] = (((1.0 / 6.0 + ka[1] * R[1] + 5.0 / 3.0 - 2.0*R[1]) / Q[1])*TP[1]
                        + ((1.0 / 6.0 + kb[1] * R[2]) / Q[2])*TP[2] + I2) / s[1];
        }


        /* CALCULATE TEMPERATURE FOR INTERNAL NODES */
```

94

```
for (i = 2; i <= m; i++) {

        /* gs = ((j*dt*L*l1*l1) / (Tm*K2) - 25e-9) / 6.0e-9*
                ((j*dt*L*l1*l1) / (Tm*K2) - 25e-9) / 6.0e-9; */
        I = power; /* * exp(-1.0*gs); */
        I1 = (1.0 - Rf)*I*exp(-1.0*(i - 1)*(a*dz*l1));
        I2 = (I1*(1.0 - exp(-a * dz*l1))*2.0*dt*l1*l1) / (k[i] * dz*Tm*l1);

        /* BOUNDRY CONDITION - FIRST MELT BOUNDARY */

        if (i == m) {
                if (melting == 1) {
                        z[i] = (TP[i - 1] * (1.0 / (3 * Q[i - 1] * (2 + st1)) +
                                (2 * dt) / (dz*dz*(2.0 + st1))) + TP[i] *
                                (2.0 / Q[i] - 1 / (3 * Q[i] * (1 + st1)) - 2.0*dt /
                                (dz*dz*(1.0 + st1))) + I2 - b[i] * z[i - 1]) / s[i];
                }

                else {

                        z[i] = (((1.0 / 6.0 + R[i]) / Q[i])*TP[i] + ((5.0 / 3.0 -
2.0*R[i]) / Q[i])*TP[i]

                                + ((1.0 / 6.0 + R[i - 1]) / Q[i - 1])*TP[i - 1] - b[i] *
z[i - 1] + I2) / s[i];
                }

        }

        else {
```

```
                          z[i] = (((1.0 / 6.0 + ka[i] * R[i + 1]) / Q[i + 1])*TP[i + 1] +

                                  ((5.0 / 3.0 - 2.0*R[i]) / Q[i])*TP[i] + ((1.0 / 6.0 + kb[i] *
R[i - 1]) / Q[i - 1])

                                  *TP[i - 1] - b[i] * z[i - 1] + I2) / s[i];


                  }
          }


          /* COMPLETE ALGORITHM -SOLVE FOR TEMPERATURE AT ALL
NODES*/


          TP[m] = z[m];


          for (i = m - 1; i >= 1; i--) { TP[i] = z[i] - u[i] * TP[i + 1]; }


          /*.........CALCULATION BEHIND THE MELT FRONT...............*/


          if (melting == 1) {


                  /* BOUNDARY CONDITION- BEHIND MELT FRONT  */


                  s[1] = 2.0 / Q[1 + (m + 1)] - 1.0 / (3.0*Q[1 + (m + 1)] * (1.0 - st1)) +
2.0*dt / (dz*dz*(1.0 - st2));


                  u[1] = (1.0 / (3.0*Q[2 + (m + 1)] * (2.0 - st1)) - 2.0*dt / (dz*dz*(2.0 -
st2))) / s[1];


                  /* INTERNAL NODES */


                  for (q = 2; q <= n - 1; q++) {
```

96

b[q] = (1.0 / 6.0 - R[q - 1 + (m + 1)]) / Q[q - 1 + (m + 1)];

s[q] = (5.0 / 3.0 + 2.0*R[q + (m + 1)]) / Q[q + (m + 1)] - b[q] * u[q - 1];

u[q] = ((1.0 / 6.0 - R[q + 1 + (m + 1)]) / Q[q + 1 + (m + 1)]) / s[q];
}

/* BACK SURFACE BOUNDARY CONDITION */

b[n] = (1.0 / 6.0 - R[n - 1 + (m + 1)]) / Q[n - 1 + (m + 1)];

s[n] = ((1.0 / 6.0 - R[n + (m + 1)] + 5.0 / 3.0 + 2.0*R[n + (m + 1)]) / Q[n + (m + 1)]) - b[n] * u[n - 1];

/* LASER SOURCE- BACK OF MELT FRONT */

/* gs = ((j*dt*L*l1*l1) / (Tm*K2) - 25e-9) / 6.0e-9*

      ((j*dt*L*l1*l1) / (Tm*K2) - 25e-9) / 6.0e-9; */

I = power; /* * exp(-1.0*gs); */

I1 = (1.0 - Rf)*I*exp(-(m + 1)*a*dz);

I2 = (I1*(1.0 - exp(-a * dz*l1))*dt*2.0*l1*l1) / (Tm*k[1 + m + 1] * dz*l1);

/* SOURCE TERM AT BACK MELT BOUNDARY*/

z[1] = (TP[2 + (m + 1)] * (1.0 / (3 * Q[2 + (m + 1)] * (2 - st1)) + 2 * dt / (dz*dz*(2.0 - st1))) +

      TP[1 + (m + 1)] * (2.0 / Q[1 + (m + 1)] - 1 / (3 * Q[1 + (m + 1)] * (1 - st1)) -

```
                2.0*dt / (dz*dz*(1.0 - st1))) + I2) / s[1];


        /* CALCULATE TEMPERATURE FOR INTERNAL NODES */


        for (i = 2; i <= n; i++) {


                /* gs = ((j*dt*L*l1*l1) / (Tm*K2) - 25e-9) / 6.0e-9*
                        ((j*dt*L*l1*l1) / (Tm*K2) - 25e-9) / 6.0e-9; */
                I = power; /* * exp(-1.0*gs); */
                I1 = (1.0 - Rf)*I*exp(-1.0*(i - 1 + (m + 1))*(a*dz*l1));
                I2 = (I1*(1.0 - exp(-a * dz*l1))*2.0*dt*l1*l1) / (k[i + m + 1] *
dz*Tm*l1);


                if (i == n) {
                        z[i] = (((1.0 / 6.0 + R[i + (m + 1)]) / Q[i + (m + 1)])*TP[i +
(m + 1)] +
                                ((5.0 / 3.0 - 2.0*R[i + (m + 1)]) / Q[i + (m +
1)])*TP[i + (m + 1)]
                                + ((1.0 / 6.0 + R[i - 1 + (m + 1)]) / Q[i - 1 + (m +
1)])
                                *TP[i - 1 + (m + 1)] - b[i] * z[i - 1] + I2) / s[i];
                }


                else {
                        z[i] = (((1.0 / 6.0 + ka[i + m + 1] * R[i + 1 + (m + 1)]) / Q[i
+ 1 + (m + 1)])*TP[i + 1 + (m + 1)] +
                                ((5.0 / 3.0 - 2.0*R[i + (m + 1)]) / Q[i + (m +
1)])*TP[i + (m + 1)] + ((1.0 / 6.0 +
                                kb[i + m + 1] * R[i - 1 + (m + 1)]) / Q[i - 1 +
(m + 1)])*TP[i - 1 + (m + 1)] - b[i] * z[i - 1] + I2) / s[i];
                }
        }
```

/* COMPLETE ALGORITHM- CALCULATE TEMPERATURE AT ALL NODES BEHIND MELT*/

TP[n + (m + 1)] = z[n];

for (i = n - 1; i >= 1; i--) { TP[i + (m + 1)] = z[i] - u[i] * TP[i + 1 + (m + 1)]; }

/* CALCULATE NEW TEMPERATURE AT NODE CLOSEST TO MELT FRONT */

/* gs = ((j*dt*L*l1*l1) / (Tm*K2) - 25e-9) / 6.0e-9*
        ((j*dt*L*l1*l1) / (Tm*K2) - 25e-9) / 6.0e-9; */
I = power; /* * exp(-1.0*gs); */
I1 = (1.0 - Rf)*I*exp(-1.0*(m + 1 - 1)*(a*dz*l1));
I2 = (I1*(1.0 - exp(-a * dz*l1))*2.0*dt*l1*l1) / (k[m + 1] * dz*Tm*l1);

TP[m + 1] = (((1.0 / 6.0 + ka[m + 1] * R[m + 2]) / Q[m + 2])*STP[m + 2]
+
        ((5.0 / 3.0 - 2.0*R[m + 1]) / Q[m + 1])*STP[m + 1]
        + ((1.0 / 6.0 + kb[m + 1] * R[m]) / Q[m])*STP[m]
        + I2 - ((1.0 / 6.0 - ka[m + 1] * R[m + 2]) / Q[m + 2])*TP[m + 2] -
        ((1.0 / 6.0 - kb[m + 1] * R[m]) / Q[m])*TP[m])*Q[m + 1] / (5.0 /
3.0 + 2.0*R[m + 1]);

/* CALCULATE HOW FAR MELT FRONT MOVES */

ds = (dt*k[m + 2]) / (2.0*dz*K2)*(TP[m + 2] * ((2.0 - st2) / (1.0 - st2)) -
        TP[m + 3] * ((1.0 - st2) / (2.0 - st2)) + STP[m + 2] * ((2.0 - st1) /
(1.0 - st1)) -

STP[m + 3] * ((1.0 - st1) / (2.0 - st1))) + (dt*k[m]) /
(2.0*dz*K2)*(TP[m] * ((2.0 + st2) / (1.0 + st2)) -

TP[m - 1] * ((1.0 + st2) / (2.0 + st2)) + STP[m] * ((2.0 +
st1) / (1.0 + st1)) - STP[m - 1] * ((1.0 + st1) / (2.0 + st1)));

/* CALCULATE WHERE THE NEW MELT FRONT POSITION LIES
*/


```
if (fabs(st1*dz + ds) <= (dz / 2.0)) {
        st1 = (st1*dz + ds) / dz;
        st2 = (st1*dz + 2.0*ds) / dz;

}


else {
        if (st1*dz + ds > dz / 2) {


                num1 = (int)(((st1*dz + ds) - dz / 2) / dz);
                m = m + (num1 + 1);
                if (m == 4) { starter = 2; }
                st1 = (-(num1 + 1)*dz + (st1*dz + ds)) / dz;
                st2 = (-(num1 + 1)*dz + (st1*dz + 2.0*ds)) / dz;

        }


        else {
                num1 = (int)((fabs(st1*dz + ds) - dz / 2) / dz);
                m = m - (num1 + 1);
                st1 = ((num1 + 1)*dz + (st1*dz + ds)) / dz;
                st2 = ((num1 + 1)*dz + (st1*dz + 2.0*ds)) / dz;
                if (starter == 1) { m = 2; st1 = st2 = 0.0; }
                else if (m == 1) { melting = 2; m = tot; }

        }
```

```c
        }

        Ts = TP[1] * Tm + Tm; /* REAL SURFACE TEMPERATURE */

        flux = beta * po / (pow(2.0*3.1415*A*R1*Ts, .5));

        flux1 = exp((Hv*(Ts - Tlv)) / (R0*Ts*Tlv));

        pressure = (po / 1000.0)*flux1; /* SATURATED VAPOR PRESSURE */


        /* CALCULATE VAPORIZATION BOUNDARY MOVEMENT DUE TO
EXPULSION */

        expulsion = ((m*6e-9)*2.0 / 260e-6)*pow((po*flux1) / density, .5)*100.0
                *((L*l1) / (Tm*K2));
        expdist = expulsion * dt;
        totexpul = totexpul + expdist;


        /* CALCULATE VAPORIZATION FRONT MOVEMENT FROM
SURFACE VAPORIZATION */

        totflux = flux * flux1;
        vsurface = ((totflux*A) / density)*100.0; /* velocity in cm/sec */
        cvsurface = (vsurface)*((L*l1) / (Tm*K2)); /* convert to dimless velocity
*/

        dsurface = cvsurface * dt;


        /* Total distance vaporation interface has moved-dimless */
        totsurface = totsurface + dsurface + expdist;
```

marker = marker + dsurface; /* tracks surface vaporization only */

/* CALCULATE ENERGY REMOVED FROM FIRST NODE- USED IN VAPORIZATION PROCESS */

```
if (((TP[1] * Tm + Tm) - Tlv) >= 0.0) {


            enout = vsurface * ((293430.0 + 10790.0) / 26.98)*2.69 +

                    vsurface * ((5.82*4.184 / 26.98)*2.69)*((TP[1] * Tm +
Tm) - 300.0);

            }
            else { enout = 0.0; }
```

/* TRACK ENERGY LOST AND CONVERT TO FORM TO BE INPUT BACK INTO PROGRAM */

```
            power1 = enout;
            enout = (enout*((2.0*dt*l1*l1) / (k[1] * dz*Tm*l1))); /* adjust units */


            /* ERROR CHECK*/


            if (totsurface >= dz) {
                    totsurface = (totsurface - dz);
                    for (i = 1; i <= tot; i++) { TP[i] = TP[i + 1]; }
                    if (totsurface >= dz) { printf("error in evaporation routine"); }
                    m = m - 1;
                    nm = nm + 1;
            }


            if (TP[1] * Tm + Tm >= Tlv) { kip = TP[1] * Tm + Tm - Tlv; }
            else { kip = 0.0; }
```

```
                } /* END OF PROCESSES OCCURRING IN THE MELT */


                /* SAVE PREVIOUS TEMPERATURE VALUES IN ARRAY */


                for (i = 1; i <= tot; i++) { STP[i] = TP[i];}


                /* CHECK FOR MELT FRONT PROPAGATION - MELT FRONT STARTED
NODE NEXT TO BOUNDARY TO AVOID CALCULATION OF THERMAL GRADIENTS
AT BOUNDARY */


                if (TP[2] >= 0.0&&melting == 0) { melting = 1; m = 3; }


                /* PRINT RESULTS TO FILE WHEN COUNTER INDICATES */


                if (cnt == 0) {


                        fprintf(lp, "%1.4e       %1.4e  %1.4e  %1.4e  %1.4e\n", (j* dt* L* l1* l1) /
                                (Tm * K2), TP[1] * Tm + Tm, (m* dz* l1 * 1e4), I, totAc* dz* l1
* 1e4);            /*1e4 converts to um*/


                        cnt2 = cnt2 + 1;


                        cts = 0; /*Counter for reduced spatial steps*/


                        ct1 = 0;


                        sumofT = 0;


                        for (i = 1; i <= tot; i++) {
                                Temp = TP[i] * Tm + Tm;
                                fprintf(fp, "%1.4e       ", Temp);
```

```
                            }
                            fprintf(fp, "\n");

                            if (m == tot) {
                                    param = allocate_real_matrix(0, nn, 0, 3);

                                    for (i = 1; i <= totAc; i++) {
                                            Temp = TP[i] * Tm + Tm;
                                            sumofT = sumofT + Temp;
                                            ct1 = ct1 + 1;
                                            // avgT = Temp;
                                            // fprintf(np, "%1.6e   ", avgT);

                                            if (ct1 == spcStep) {
                                                    avgT = sumofT / double(spcStep);
                                                    fprintf(np, "%1.6e    ", avgT);
                                                    ct1 = 0;
                                                    sumofT = 0;

                                                    if (avgT <= 1100) {
                                                            rhoT = 4466.5 - 0.14346 * avgT;
                                                            E = 1.3211e11 - 5.3476e7 * avgT;
                                                            v = 0.30444 + 4.3136e-5 * avgT;
                                                            G = E / (2 * (1 + v));
                                                            cT = sqrt(G / rhoT);
                                                            cL = sqrt((E * (1 - v)) / (rhoT * (1 - 2 * v) *
(1 + v)));

                                                    }

                                                    else if (avgT > 1100 && avgT <= 1275) {
```

```
                                        rhoT = -1.06197e5 + 377.102 * avgT -
0.48139 * avgT * avgT + 2.72431e-4 * avgT * avgT * avgT - 5.76672e-8 * avgT * avgT * avgT
* avgT;

                                        E = -2.86129e13 + 9.80836e10 * avgT -
1.25480e8 * avgT * avgT + 71192 * avgT * avgT * avgT - 15.1157 * avgT * avgT * avgT *
avgT;

                                        v = 0.71057 - 7.3107e-4 * avgT + 3.6983e-7
* avgT * avgT;

                                        G = E / (2 * (1 + v));

                                        cT = sqrt(G / rhoT);

                                        cL = sqrt((E * (1 - v)) / (rhoT * (1 - 2 * v) *
(1 + v)));

                                }


                                else if (avgT > 1275 && avgT <= (Tm + 1)) {

                                        rhoT = 4576.8 - 0.20406 * avgT;

                                        E = 1.2157e11 - 3.8674e7 * avgT;

                                        v = 0.31529 + 4.9955e-5 * avgT;

                                        G = E / (2 * (1 + v));

                                        cT = sqrt(G / rhoT);

                                        cL = sqrt((E * (1 - v)) / (rhoT * (1 - 2 * v) *
(1 + v)));

                                }


                                param[cts][0] = 1.0 / (1e-3 *
cT);//1.0/1.809;//3.13;//st

                                param[cts][1] = 1.0 / (1e-3 * cL);//6.32;//sl

                                param[cts][2] = spcStep * l1 * dz * 10;  //h
Substrate Thickness - 10 converts cm to mm

                                param[cts][3] = (1e-3 * rhoT) / (param[cts][0] *
param[cts][0]); //mu


                                fprintf(mp, "%1.6e     %1.6e  %1.6e  %1.6e
%1.6e\n", avgT, cT, cL, rhoT, param[cts][2]);
```

```
                        cts = cts + 1;
                    }


                }
            }


        else {
                param = allocate_real_matrix(0, (totAc - m) + 1, 0, 3);


                param[0][0] = 1.0 / (1e-3 * 16);//1.0/1.809;//3.13;//st
                param[0][1] = 1.0 / (1e-3 * 4407);//6.32;//sl
                param[0][2] = m * l1 * dz * 10;  //h Substrate Thickness - 10
converts cm to mm
                param[0][3] = (1e-3 * 3920) / (param[0][0] * param[0][0]); //mu


                fprintf(mp, "%i         %i      %i     %i      %1.6e\n", m, 16,
4407, 3920, param[0][2]);


                cts = 1;
                for (i = m + 1; i <= (totAc); i++) {
                        Temp = TP[i] * Tm + Tm;
                        sumofT = sumofT + Temp;
                        ct1 = ct1 + 1;


                        if (ct1 == spcStep) {
                                avgT = sumofT / double(spcStep);
                                fprintf(np, "%1.6e     ", avgT);
                                sumofT = 0;
                                ct1 = 0;

                                106
```

```
if (avgT <= 1100) {

        rhoT = 4466.5 - 0.14346 * avgT;

        E = 1.3211e11 - 5.3476e7 * avgT;

        v = 0.30444 + 4.3136e-5 * avgT;

        G = E / (2 * (1 + v));

        cT = sqrt(G / rhoT);

        cL = sqrt((E * (1 - v)) / (rhoT * (1 - 2 * v) *
(1 + v)));

    }


    else if (avgT > 1100 && avgT <= 1275) {

            rhoT = -1.06197e5 + 377.102 * avgT -
0.48139 * avgT * avgT + 2.72431e-4 * avgT * avgT * avgT - 5.76672e-8 * avgT * avgT * avgT
* avgT;

            E = -2.86129e13 + 9.80836e10 * avgT -
1.25480e8 * avgT * avgT + 71192 * avgT * avgT * avgT - 15.1157 * avgT * avgT * avgT *
avgT;

            v = 0.71057 - 7.3107e-4 * avgT + 3.6983e-7
* avgT * avgT;

            G = E / (2 * (1 + v));

            cT = sqrt(G / rhoT);

            cL = sqrt((E * (1 - v)) / (rhoT * (1 - 2 * v) *
(1 + v)));

    }


    else if (avgT > 1275 && avgT <= (Tm + 1)) {

        rhoT = 4576.8 - 0.20406 * avgT;

        E = 1.2157e11 - 3.8674e7 * avgT;

        v = 0.31529 + 4.9955e-5 * avgT;

        G = E / (2 * (1 + v));

        cT = sqrt(G / rhoT);
```

107

```
                                            cL = sqrt((E * (1 - v)) / (rhoT * (1 - 2 * v) *
(1 + v)));
                                        }


                                        param[cts][0] = 1.0 / (1e-3 *
cT);//1.0/1.809;//3.13;//st

                                        param[cts][1] = 1.0 / (1e-3 * cL);//6.32;//sl
                                        param[cts][2] = spcStep * ll * dz * 10;  //h
Substrate Thickness - 10 converts cm to mm
                                        param[cts][3] = (1e-3 * rhoT) / (param[cts][0] *
param[cts][0]); //mu


                                        fprintf(mp, "%1.6e    %1.6e  %1.6e  %1.6e
    %1.6e\n", avgT, cT, cL, rhoT, param[cts][2]);


                                        cts = cts + 1;
                                    }
                                }
                            }


            fprintf(np, "\n");


        printf("Run Number %d out of %d\n", cnt2, int(1 + (tottime-1)/timeStep));


        param[cts][0] = 1.0 / (1e-3 * cT);//1.0/1.809;//3.13;//st
        param[cts][1] = 1.0 / (1e-3 * cL);//6.32;//sl
        param[cts][2] = 0.0;//1.5; //h Substrate Thickness
        param[cts][3] = (1e-3 * rhoT) / (param[cts][0] * param[cts][0]);//mu


        for (i = 0; i < (cts+1); i++) {
```

```
                printf("layer[%d],%f %f %f %f\n", i, 1 / param[i][0], 1 / param[i][1],
param[i][2], param[i][3]);

                fprintf(kp, "%i %1.6e  %1.6e  %1.6e  %1.6e\n", i, 1 / param[i][0], 1 /
param[i][1], param[i][2], param[i][3]);

        }


        printf("Run Number %d out of %d\n", cnt2, int(1 + (tottime - 1) / timeStep));


        //exit(1);
        /* Spatial frequency begins at gbeg and ends at gend  */


                // Inputs into Transfer Matrix
                //Laser Source parameters
        kmax = 201;//1300;//1700;//4901; 301
        gbeg = 0.0;
        gend = 160;
        tsmin = 0.0;
        tsmax = 1.0;// time in microseconds
        per = 0.75 * tsmax;
        pts = kmax;


        prm[0] = 0.05;//radius at the FWHM in mm
        prm[0] = sqrt(prm[0] * prm[0] * 2.0);//radius at the 1/e^2 point
        prm[1] = 6.58410e-5;  // thermal diffusivity
        prm[2] = 10.0e-3;// laser pulse width in microseconds
        prm[3] = tsmin;  // tmin in microseconds
        prm[4] = tsmax; //tmax in microseconds


        tmp1 = allocate_real_vector(0, 3 * pts);
        //source to receiver distance in mm
```

```
voferror = 0.1e-9; //0.1e-13
error[1] = voferror;
error[2] = voferror;
errorlp = 1.0e-9;
error[3] = 2.4e-7;



alp1 = 0.01;//0.1
alp2 = 1.00001 * alp1 - (log(errorlp)) / (2.0 * per);
rfreq = alp2;//real part of the frequency in the laplace domain.
/*****************************************/


s2rd = 1.0;
for (i = 1; i <= kmax; i++) {


        w = ((double)(i)-1.0) * pi / per;


        index = 2 * i - 1;


        omega.real(rfreq);
        omega.imag(w); //Temporal frequency


        ior = 1;
        //real part of hankel transform
        rhankinv = qadrat(&x, gbeg, gend, omega, cts+1, cts, param, solid, error,
prm, s2rd, ior);
        //imaginary part of hankel transform
        ior = 2;
```

```c
                    chankinv = qadrat(&x, gbeg, gend, omega, cts+1, cts, param, solid, error,
prm, s2rd, ior);


                    tmp1[index] = rhankinv;
                    tmp1[index + 1] = chankinv;
                    printf("%i\n", i);


          }
          printf("%f\n", s2rd);
          printf("Begin Laplace Inversion\n");


          //Inverse Laplace transform
          lapinv(tmp1, kmax, alp1, errorlp, tsmin, tsmax, pts);
          for (i = 1; i <= pts; i++) {
                    //j = 2 * i - 1;
                    scop = (tsmin + (tsmax - tsmin) * ((double)(i)-1.0) / pts);


                    fprintf(tp, "%f\n", scop);
                    fprintf(ap, "%e          ", tmp1[2*i]);
                    //fprintf(fp,"%f          ",tmp1[j+1]);


          }
          // fprintf(fp,"\n");


          free_real_vector(tmp1, 0, 2 * pts);


          //cnt = cnt + 1;
          fprintf(ap, "\n");
          }
```

```
                cnt = cnt + 1; if (cnt == timeStep) { cnt = 0; }   /*    Counter-write to file when
counter = 0 */

        }


        free_double_vector(s, 1);

        free_double_vector(z, 1);

        free_double_vector(u, 1);

        free_double_vector(Q, 1);

        free_double_vector(R, 1);

        free_double_vector(b, 1);

        free_double_vector(k, 1);

}

void free_double_vector(double *v, int l)

{

        /*  Frees   a real vector of range [l..u].  */

        free((char*)(v + l));

}


double *allocate_double_vector(int l, int u)

{

        /*  Allocates a real vector of range [l..u].  */


        //void system_error(char *);

        double *p;


        p = (double *)calloc((unsigned)(u - l + 1), sizeof(double));

//        if (!p) system_error("Failure in allocate_real_vector().");

        return p - l;

}
```

APPENDIX II

Onscale Code for 3-D Finite Element Model with a Temperature Field Imported

All constants set for Titanium alloy Ti-6Al-4V

```
c 3D Surface Acoustic Model with Thermoelastic Laser Line Source
mem MB 100000 250


titl SP SP
c symbx holem = 0.0                              /* RADIUS of melt


symb #get { labl } jobname       /* get the name of the job, i.e., <jobname>.flxinp and call it labl
rest no                  /* no restart file saved


mp omp /* 4 dyn                              /* Parallelise computation across <2> cores
(dynamically)


symb simtime = 0.3500e-6            /* Simulation Time
symb spotsize = 10.0e-6                  /* Excitation spot size radius in FWHM
symb freqmax = 2958 / $spotsize     /* Frequency content        (calc'd from v_R/spot size)
symb velmin = 3182              /* Min wave velocity (shear speed)
symb wavemin = $velmin / $freqmax       /* Min wave length (lamba = c/f)
c symb box = $wavemin / 10            /* Element size (box = wavelength/10)
symb box = 1.0e-6
symb spotloc = 0.2e-3            /* Location of excitation line source


symb boxx = $box
symb boxy = $box
symb boxz = $box
```

```
c
********************************************************************************
*****
c                                   Model
c
********************************************************************************
*****
symb dx1 = 1.00e-3
symb dy1 = 0.85e-3
symb dz1 = 1.00e-3
symb name = i


c Geometry End Points x
symb x1 = 0.0
symb x2 = $x1 + $dx1                      /*


c Geometry End Points y
symb y1 = 0.0
symb y2 = $y1 + $dy1                      /*


c Geometry End Points y
symb z1 = 0.0
symb z2 = $z1 + $dz1            /*


c
********************************************************************************
*****
c                                   MESHING
c
********************************************************************************
*****
symb i1 = 1
symb i2 = $i1 + nint ( ( $x2 - $x1 ) / $boxx )                 /*End abs Zone 1 and start source
```

```
symb indgrd = $i2


symb j1 = 1
symb j2 = $j1 + nint ( ( $y2 - $y1 ) / $boxy )              /*End Symm Step 1
symb jndgrd = $j2


symb k1 = 1
symb k2 = $k1 + nint ( ( $z2 - $z1 ) / $boxz )              /*End Symm Step 1
symb kndgrd = $k2


grid $indgrd $jndgrd $kndgrd


geom
        xcrd $x1 $x2 $i1 $indgrd
        ycrd $y1 $y2 $j1 $jndgrd
        zcrd $z1 $z2 $k1 $kndgrd
        end
```

c
****
*****
c   MATERIAL PROPERTIES
c
****
*****


```
symb wavevel_s = 3.182e3    /* shear wave speed in m/s
symb wavevel_l = 6.130e3    /* long wave speed in m/s
symb rho = 4420.                    /* density in kg/m3
```

```
symb wavevel_ll = 4.407e3   /* LIQUID long wave speed in m/s
symb rhol = 3920.            /* LIQUID density in kg/m3


matr
    wvsp on                                /* Use wavespeeds to specify mat. props
    prop myTi $rho $wavevel_l $wavevel_s            /*name of material and then
properties
        end


matr
    wvsp on                                /* Use wavespeeds to specify mat. props
    prop myTiL $rhol $wavevel_ll 0.0
        end
c
*******************************************************************************
*****
c                          IMPORTING TEMPERATURE FIELD
c
*******************************************************************************
*****
symb #read 'tempDist_fcnt_3D_June2022_8W.txt'
symb t = $T10101 * $T20202
symb #msg 1
Calculated Temp is $t
term


symb nZZ = 1
symb mT = 0
symb nV = 14              /* Size of temperature field grid
```

```
do loopTempF3 ZZ 1 $nV 1

        symb nYY = 1

        do loopTempF2 YY 1 $nV 1

                symb nXX = 1

                do loopTempF1 XX 1 $nV 1

                        symb TT_diff = $T$(nXX)$(mT)$(nYY)$(mT)$(nZZ)

                        symb TT_K = $TT_diff + 293


                        if ( $TT_K lt 1100.0 ) then

                                symb rho_ = 4466.5 - 0.14346 * ( $TT_K )

                                symb E_ = 1.3211e11 - 5.3476e7 * ( $TT_K )

                                symb v_ = 0.30444 + 4.3136e-5 * ( $TT_K )

                                symb G_ = $E_ / ( 2 * ( 1 + $v_ ) )

                                symb cT_ = ( $G_ / $rho_ ) ** ( 1. / 2. )

                                symb cL_ = ( ( $E_ * ( 1 - $v_ ) ) / ( $rho_ * ( 1 - 2 * $v_ ) * ( 1 +
$v_ ) ) ) ** ( 1. / 2. )


                        elseif ( $TT_K gt 1100.0 and $TT_K le 1275.0 ) then

                                symb rho_ = -1.06197e5 + 377.102 * $TT_K - 0.48139 * $TT_K *
$TT_K + 2.72431e-4 * $TT_K * $TT_K * $TT_K - 5.76672e-8 * $TT_K * $TT_K * $TT_K *
$TT_K

                                symb E_ = -2.86129e13 + 9.80836e10 * $TT_K - 1.25480e8 *
$TT_K * $TT_K + 71192 * $TT_K * $TT_K * $TT_K - 15.1157 * $TT_K * $TT_K * $TT_K *
$TT_K

                                symb v_ = 0.71057 - 7.3107e-4 * $TT_K + 3.6983e-7 * $TT_K *
$TT_K

                                symb G_ = $E_ / ( 2 * ( 1 + $v_ ) )

                                symb cT_ = ( $G_ / $rho_ ) ** ( 1. / 2. )

                                symb cL_ = ( ( $E_ * ( 1 - $v_ ) ) / ( $rho_ * ( 1 - 2 * $v_ ) * ( 1 +
$v_ ) ) ) ** ( 1. / 2. )
```

```
                    elseif ( $TT_K gt 1275.0 ) then

                            symb rho_ = 4576.8 - 0.20406 * ( $TT_K )

                            symb E_ = 1.2157e11 - 3.8674e7 * ( $TT_K )

                            symb v_ = 0.31529 + 4.9955e-5 * ( $TT_K )

                            symb G_ = $E_ / ( 2 * ( 1 + $v_ ) )

                            symb cT_ = ( $G_ / $rho_ ) ** ( 1. / 2. )

                            symb cL_ = ( ( $E_ * ( 1 - $v_ ) ) / ( $rho_ * ( 1 - 2 * $v_ ) * ( 1 +
$v_ ) ) ) ** ( 1. / 2. )

                    endif


                    symb m_name = T$(name)$(nXX)$(mT)$(nYY)$(mT)$(nZZ)

matr

      wvsp on                                /* Use wavespeeds to specify mat. props

      prop $m_name $rho_ $cL_ $cT_

      end

                    symb nXX = $nXX + 1

                    end$ loopTempF1

            symb nYY = $nYY + 1

            end$ loopTempF2

            symb nZZ = $nZZ + 1

      end$ loopTempF3


symb nXX = 1

symb nYY = 1

symb nZZ = 1


symb nV = $nV - 1                           /* because linspace was used to create vectors in
Matlab


symb yb = 0
```

```
symb spc = 0.25e-3 / $nV                        /* Size of temperature field calculcated

symb ctr = 0.5e-3                               /* Center of heated region


site

        regn myTi $i1 $indgrd $j1 $jndgrd $k1 $kndgrd

c       regn void $i1 $indgrd $j1 $jndgrd $k1 $kndgrd

        do p_l_loopL YY 1 $nV 1

                symb xb = $ctr

                symb xbn = $ctr

                symb nXX = 1

                do p_l_loopM XX 1 $nV 1

                        symb zb = 0

                        symb nZZ = 1

                        do p_l_loopN ZZ 1 $nV 1

                                text m_name = T$(name)$(nXX)$(mT)$(nYY)$(mT)$(nZZ)

                                symb y_current = $YY * $spc

                                symb x_current = $XX * $spc

                                symb z_current = $ZZ * $spc

                                symb xx = $ctr + $x_current

                                symb xxn = $ctr - $x_current

                                blok $m_name part stnd $xb $xx $yb $y_current $zb $z_current
$i1 $indgrd $j1 $jndgrd $k1 $kndgrd

                                blok $m_name part stnd $xxn $xbn $yb $y_current $zb $z_current
$i1 $indgrd $j1 $jndgrd $k1 $kndgrd

                                symb nZZ = $nZZ + 1

                                symb zb = $z_current

                                end$ p_l_loopN

                        symb xb = $xx

                        symb xbn = $xxn

                        symb nXX = $nXX + 1
```

```
                    end$ p_l_loopM

                    symb yb = $y_current

                    symb nYY = $nYY + 1

             end$ p_l_loopL

c       sphr myTiL $ctr 0.0 0.0 $holem 0.0 0.0 360.0 0.0 360.0 $i1 $indgrd $j1 $jndgrd $k1
$kndgrd

        end


grph

        set imag tiff

        nvew 2 2

        eye 0.05 -0.4 -1.0

    plot matr

        eye -1 -1 1

        vert 1 1 1

    plot matr

        imag

    end



c
********************************************************************************
*****
c                         BOUNDARY CONDITIONS & LOADING
c
********************************************************************************
*****
term


boun

    side xmin absr

    side xmax absr
```

```
    side ymin symm

    side ymax absr

        side zmin free

    side zmax absr

        end



data hist drv1 * thermoelastpulse1p5ns.dat    /*Import thermoelastic pulse as a .dat file

func hist drv1



c Laser Line Source

symb p_scale = 1.e6              /*Magnitude scaling

symb FWHM = nint ( ( 1 * $spotsize ) / $boxx )           /*Beam diamter FWHM for
Gaussian

symb sig_e2 = $FWHM * 0.8493218                          /*Convert from FWHM to
1/e^2



symb imean = $i1 + nint ( ( $spotloc ) / $boxx )           /* Location of excitation on xaxis

symb iss = $imean - nint ( ( 10.0e-6 ) / $boxx )           /*Beam diamter extent FWHM for
Gaussian

symb ise = $imean + nint ( ( 10.0e-6 ) / $boxx )           /*Beam diamter extent FWHM for
Gaussian

symb II = 1



symb KK = 1



plod


        do p_l_loopI I $iss $ise 1


                symb r_current = sqrt ( ( ( $I - $imean ) * ( $I - $imean ) ) )
```

```
        symb p_scale = $r_current * exp ( ( -2.0 * ( $r_current * $r_current ) / ( $sig_e2 *
$sig_e2 ) ) )

        symb iend = nint ( $I + 1 )

        symb KK = $KK + 1

        symb II = $I + 1


        text v_name = TV$(name)$(KK)

        text c_name = T$(name)$(KK)


        symb icond = ( $I - $imean )


        if ( $icond lt 0.0 ) then

                vctr $v_name -1. 0. 0.

        else

                vctr $v_name 1. 0. 0.

        endif


        pdef $c_name func $p_scale

        sdef $c_name $v_name $I $II $j1 $jndgrd $k1 $k1



        end$ p_l_loopI

    end


c
*******************************************************************************
*****

c                                    OUTPUTS

c
*******************************************************************************
*****
```

```
calc

    disp z

        end


symb idos = $i1 + nint ( ( 0.8e-3 ) / $boxx )          /*Beam diamter FWHM for Gaussian

c symb idoe = $i1 + nint ( ( 2.25e-3 ) / $boxx )           /*Beam diamter FWHM for
Gaussian


c pout

c        form matlab

c        hist zdsp $idos $idos 1 $j1 $j1 1 $k1 $k1 1

c        end


pout

        hist zdsp $idos $idos 1 $j1 $j1 1 $k1 $k1 1

        end


prcs


symb tr = 10                                              /* Save only every "tr"th time step

symb name = ime

symb decim = 1


symb ids = $i1

symb ide = $indgrd

symb jds = $j1

c symb jde = $j1

symb jde = $jndgrd
```

c

****

*****

c

c   RUN THE MODEL

c

c

****

*****

symb #get { step } timestep   * Timestep size

symb nsteps = nint ($simtime / ($tr * $step))   /* Number of steps needed to reach time simtime

data

       symb i_min = $ids   /* min "i" nodal coordinate (x)

       symb i_max = $ide   /* max "i" nodal coordinate (x)

       symb j_min = $jds   /* min "j" nodal coordinate (y)

       symb j_max = $jde   /* max "j" nodal coordinate (y)

       symb k_min = $k1   /* min "k" nodal coordinate (z)

       symb k_max = $k1   /* max "k" nodal coordinate (z)

       symb xy_plane = $z1   /* Position of the xy-plane (z)

       symb xz_plane = $y1   /* Position of the xz-plane (y)

       symb yz_plane = $x1   /* Position of the yz-plane (x)

       symb #read save_coordinates.temp

       end

```
do loopi I 1 $nsteps
symb #msg 1
Loop $I of $nsteps
exec $tr
data

        open dummy1 3 $i_length $j_length 1 f

        cpyg zdsp $i_min $decim $j_min $decim $k_max 1 dummy1 1 $i_length 1 $j_length 1 1
        cddo dummy1 z_tep_$I.txt 1 $i_length 1 $j_length 1 1

        end
end$ loopi

stop
```